

An empirical model of ionospheric scintillation at high latitudes

by

Hichem Mezaoui

MSc, University of Provence, 2009

**A DISSERTATION SUBMITTED IN PARTIAL FULFILLMENT
OF THE REQUIREMENTS FOR THE DEGREE OF**

Doctor of Philosophy

In the Graduate Academic Unit of Physics

Supervisors: Abdelhaq M. Hamza, PhD, Dept. of Physics
 P. Thayyil Jayachandran, PhD, Dept. of Physics
Examining Board: B. Newling, PhD, Dept. of Physics
 D. Tokaryk, PhD, Dept. of Physics
External Examiner: R. B. Langley, PhD, Dept. of Geodesy and Geomatics Engineering
 A. V. Koustov, PhD, Dept. of Physics, University of Saskatchewan

This dissertation is accepted

Dean of Graduate Studies

THE UNIVERSITY OF NEW BRUNSWICK

May, 2017

©Hichem Mezaoui, 2017

Abstract

Trans-ionospheric radio signals experience both amplitude and phase variations as they propagate through a turbulent ionosphere, this phenomenon is known as scintillation. As a result of these fluctuations, GPS receivers lose track of signals and consequently induce positioning and navigational errors. Therefore, there is a need to study scintillation and their causes in order to not only resolve the navigational problem but in addition develop analytical and numerical radio propagation models.

This thesis presents the work that has been done to develop an empirical model of ionospheric scintillation at high latitudes. In this study, GPS L1 signals were recorded and characterized using the Canadian High Arctic Ionospheric Network (CHAIN). We developed new indices to quantify scintillation and the chaoticity of the turbulent ionosphere. More particularly, we used the multi-fractal aspect of the scintillating GPS signal to compute the corresponding wavelet-based entropy and fractal dimension. These indices were used to construct scintillation maps in the geomagnetic domain. It has been found that the chaoticity of the scintillating signal exhibits a dependence on

geomagnetic conditions and a seasonal cycle, suggesting the possibility to quantify the ionospheric turbulence using the proposed indices.

In the second part of the thesis, a simulator of the trans-ionospheric channel was developed. The model takes into account the case of strong scintillation, where the amplitude fluctuations start to build up inside the ionospheric slab. The features of the power spectra of the observed scintillation events were reproduced: it has been found that the amplitude fluctuations are characterized by a power spectral density that obeys a power law with a breakdown at the Fresnel scale. The phase, on the other hand, does not exhibit a breakdown of the power law, which is in agreement with the observations.

Dedication

To my family

Table of Contents

| | |
|--------------------------------------------------------|-----|
| Abstract | ii |
| Dedication | iv |
| Table of Contents | xi |
| List of Tables | xii |
| List of Figures | xix |
| Abbreviations | xx |
| 1 Introduction and Thesis Outline | 1 |
| 1.1 Introduction | 1 |
| 1.2 Dissertation Outline | 5 |
| 2 The Earth's ionosphere | 7 |
| 2.1 Solar atmosphere | 7 |
| 2.1.1 The internal and atmospheric structure | 7 |
| 2.1.2 Solar cycle | 10 |

| | | |
|---------|-------------------------------------------------------------|----|
| 2.2 | Solar Activity | 11 |
| 2.2.1 | Co-rotating Interaction Region | 11 |
| 2.2.2 | Coronal Mass Ejections (CMEs) | 12 |
| 2.2.3 | Flares | 13 |
| 2.3 | Magnetosphere | 13 |
| 2.4 | Morphology of the ionosphere | 18 |
| 2.4.1 | D layer | 20 |
| 2.4.2 | E Layer | 20 |
| 2.4.3 | F Layer | 20 |
| 2.4.4 | Transport | 21 |
| 2.4.5 | Ambipolar Diffusion | 24 |
| 2.5 | Radio Waves in the Ionospheric Plasma | 25 |
| 2.6 | The High Latitude Ionosphere | 29 |
| 2.6.1 | The characteristics of the ionospheric conductivity . . . | 32 |
| 2.6.2 | Sources of the ionospheric irregularities at high latitudes | 35 |
| 2.6.2.1 | Particle Precipitation | 36 |
| 2.6.2.2 | Gradient drift instability | 36 |
| 2.6.2.3 | Kelvin-Helmholtz Instability | 37 |
| 2.6.2.4 | Farley Buneman instability | 38 |
| 2.7 | Monitoring the ionosphere | 39 |
| 2.7.1 | Sporadic E-layers | 43 |
| 2.7.2 | Spread-F | 44 |

| | |
|----------------------------------------------------------------|-----------|
| 3 Global Positioning System | 45 |
| 3.1 Overview | 46 |
| 3.1.1 GPS signal characteristics | 46 |
| 3.1.2 Positioning techniques | 47 |
| 3.2 Derived observables for ionospheric studies | 53 |
| 3.2.1 Total electron content | 53 |
| 3.2.2 Vertical projection | 56 |
| 3.3 Canadian High Arctic Ionospheric Network (CHAIN) | 59 |
| 3.3.1 GPS receivers | 59 |
| 3.3.2 Canadian Advanced Digital Ionosonde (CADI) | 60 |
| 4 Overview of ionospheric scintillation | 65 |
| 4.1 Describing the dielectric function | 66 |
| 4.1.1 Multi-scale aspect of the dielectric function | 66 |
| 4.1.2 Stationarity | 67 |
| 4.1.3 Probability density function | 68 |
| 4.1.4 Spatial covariance | 70 |
| 4.1.5 Power spectra | 72 |
| 4.2 Geometric optics | 77 |
| 4.2.1 Optical path | 77 |
| 4.2.2 Taylor hypothesis: frozen fields | 79 |
| 4.2.3 Case of non-frozen fields | 81 |
| 4.3 Maxwell's equations in a random medium | 83 |

| | | |
|----------|----------------------------------------------------------------------------------------------------------------|------------|
| 4.4 | General solutions | 92 |
| 4.5 | Rytov's approximation | 93 |
| 4.5.1 | The Rytov transformation | 93 |
| 4.5.2 | The Basic Rytov Solution | 97 |
| 5 | Application of the maximum entropy principle in the de- termination of the scintillation components | 100 |
| 5.1 | Wavelet transform | 101 |
| 5.1.1 | Introduction | 101 |
| 5.1.2 | Definition | 102 |
| 5.1.3 | Wavelet transform of a discrete signal | 104 |
| 5.1.4 | Basis wavelet | 106 |
| 5.1.5 | Morlet wavelet | 107 |
| 5.1.6 | Signal reconstruction | 109 |
| 5.1.7 | Multifractal nature of the ionospheric scintillation . . | 110 |
| 5.2 | Entropy | 112 |
| 5.2.1 | Wavelet-based general Tsallis entropy | 114 |
| 5.2.2 | Optimization of the detrending scale | 115 |
| 5.2.3 | Gaussian statistics | 120 |
| 5.3 | Summary and conclusion | 124 |
| 6 | Intermittent scintillation | 126 |
| 6.1 | A simple intermittency model | 127 |
| 6.1.1 | Higher order moments | 127 |

| | | |
|----------|----------------------------------------------------------------------------------|------------|
| 6.1.2 | Castaing distribution | 130 |
| 6.2 | Discussion and conclusion | 133 |
| 7 | Statistical characteristics of ionospheric scintillations | 138 |
| 7.1 | Phase space reconstruction | 139 |
| 7.1.1 | Information Dimension | 139 |
| 7.1.2 | Attractor dimension reconstruction | 141 |
| 7.1.3 | Wavelet-based fractal dimension | 143 |
| 7.2 | Climatology | 144 |
| 7.2.1 | Optimum scale | 148 |
| 7.2.1.1 | Analysis of the optimum scale using the entropy maximization technique | 149 |
| 7.2.1.2 | Variation of the optimum scale with the elevation angle | 154 |
| 7.2.2 | Variation of the fractal dimension | 156 |
| 7.2.3 | Variation of the entropy | 162 |
| 7.3 | Conclusion | 167 |
| 8 | Simulator of the trans-ionospheric channel | 168 |
| 8.1 | Spectral model | 169 |
| 8.2 | Numerical results | 174 |
| 8.2.1 | Time series generation | 174 |
| 8.2.2 | Effect of the spectral index on the field | 176 |
| 8.3 | Conclusion | 182 |

List of Tables

| | |
|----------------------------------------------------------------|-----|
| 3.1 GPS observables and the corresponding wavelengths and pre- | |
| cisions. | 48 |
| 7.1 The CHAIN stations and the corresponding geographic and | |
| corrected geo-magnetic coordinates. | 147 |

List of Figures

| | | |
|-----|-----------------------------------------------------------------------------------------------------------------------------------------------------------------------------------------------------------------------------------------------------------------------------------------------|----|
| 2.1 | Temperature profile at the surface of the sun. Courtesy: National Center for Atmospheric Research (NCAR). | 9 |
| 2.2 | Structure of the Sun [http://solarsystem.nasa.gov]. | 9 |
| 2.3 | Illustration of the Co-rotating Interaction Regions (CIRs). Courtesy: National Center for Atmospheric Research (NCAR). . . | 12 |
| 2.4 | Diagram showing the basic structure and electric current systems of the magnetosphere for an observer situated a) at dusk in the Sun-Earth plane [Hunsucker and Hargreaves, 2003] and b) in the afternoon sector above the Sun-Earth plane [De Keyser, 2005]. | 15 |
| 2.5 | Typical ionospheric profile and its neutral elements composition, where dashed and solid lines represent the profile during day and night, respectively [Kelley, 2009]. | 19 |
| 2.6 | Illustrations of thermospheric heating and the ionization processes for different elements of the ionosphere. Photon flux enters the atmosphere and ionization processes convert photon energy to chemical potential energy. | 22 |

| | | |
|------|--------------------------------------------------------------------------------------------------------------------------------------------------------------------------------------------------------------------------------------------------------------------------------------------------------------------------|----|
| 2.7 | Orthogonal coordinate system for a propagating radio-wave. The geomagnetic field lies in the x-y plane [Mushini, 2013]. . . | 26 |
| 2.8 | Statistical locations of auroral activity during periods of quiet, moderate and high geomagnetic activity. Data are from all-sky camera images [Kivelson and Russell, 1995] | 31 |
| 2.9 | Example of the ionospheric conductivity profile: illustration of the variation of the different components of conductivity with height in mid-latitude ionosphere during day time. Courtesy: National Center for Atmospheric Research (NCAR) | 34 |
| 2.10 | Gradient drift instability mechanism in the E and F regions of the ionosphere [Tsunoda, 1988]. | 38 |
| 2.11 | Illustration of an ionogram obtained using an ionsonde. The X-axis represents the frequency and the Y-axis represents the virtual height. Critical frequencies of ionospheric layers and corresponding heights are also seen, for both ordinary and extraordinary modes. | 41 |
| 3.1 | Sketch of hypothesized diffraction of multipath ray around the ground plane for a high elevation satellite and an elevated GPS antenna [Mushini, 2013]. | 54 |

| | |
|--------------------------------------------------------------------------------------------------------------------------------------------------------------------------------------------------------------------------------------------|----|
| 3.2 Color coded examples of phase and code derived TEC, phase leveled TEC, vertical TEC, and satellite elevation. A satellite elevation cutoff of 20° is indicated by vertical dotted lines [Watson, 2011]. | 57 |
| 3.3 Diagram representing the thin shell assumption and also the ionospheric pierce point (IPP), slant-TEC (STEC), vertical-TEC (VTEC) are shown. Courtesy: Royal Observatory of Belgium. | 58 |
| 3.4 The distribution of the GPS receivers and Canadian Advanced Digital Ionosondes (CADIs) in the Canadian High Arctic Ionospheric Network. | 60 |
| 3.5 CHAIN GPS antenna (a) and NovAtel Receiver (b) located in Cambridge Bay, NU (http://chain.physics.unb.ca/chain/). . . | 61 |
| 3.6 CHAIN CADI transmitting and receiving antennas (a) and box containing CADI receivers (b) located in Hall Beach, NU. | 62 |
| 3.7 Ionogram from the Eureka CADI from signal broadcast at 03:00 UT on 1 November 2011. Received signal power as a function of reflected virtual height and broadcast frequency is indicated for ordinary and extraordinary modes. | 63 |

| | |
|---------------------------------------------------------------------------------------------------------------------------------------------------------------------------------------------------------------------------------------------------------------------------------------------------------------------------------------------------------------------------------------------------------------|-----|
| 3.8 Measurements of the Eureka CADI for 24 hours on 1 November 2011. 4.2 MHz group range (top panel), azimuthal ionospheric drift direction (2^{nd} panel), horizontal ionospheric drift speed (3^{rd} panel), and vertical ionospheric drift speed (bottom panel). Drift velocity was calculated from the 4.2 MHz broadcast, while the color bar is the power of the reflected 4.2 MHz signal. | 64 |
| 4.1 A conceptual description of the process of turbulence decay as it proceeds through an energy cascade in which eddies subdivide into progressively smaller eddies until they finally dissipate | 75 |
| 5.1 An illustration of shifting and scaling of a mother wavelet in order to calculate the wavelet transform [Mushini, 2013]. | 104 |
| 5.2 Illustration of four different mother wavelets: (a) Morlet, (b) Paul, (c) Mexican hat, and (d) DOG. The parameter m represents the number of vanishing moments and the solid line shows the real part, while dashed line shows the imaginary part of the signal [Mushini, 2013]. | 107 |
| 5.3 Construction of the Morlet wavelet is illustrated. (a) representation of a Morlet wavelet and (b) construction of a Morlet wavelet by convolving a Gaussian curve with a sine wave [Mushini, 2013]. | 108 |

| | |
|---------------------------------------------------------------------------------------------------------------------------------------------------------------------------------------------------------------------|-----|
| 5.4 Example of a scalogram of the power (left pannel) and the phase (right panel) components of the GPS L1 signal, during the scintillation event at Cambridge Bay, 7 th of March, 2008, PRN 31. | 112 |
| 5.5 The fit of the probability density function during the event at Qikiqtarjuaq, 2011/02/14, PRN 15, dotted points and solid line represent the data and the fit, respectively. | 119 |
| 5.6 The fit of $p(s_i)$ for the phase, solid line, $\beta = \frac{1}{\sigma^2} = 0.37$. The distribution presents quasi-Gaussian statistics, with a kurtosis, $k=3.03$, and a skewness, $s=0.08$ | 122 |
| 6.1 Differential power signal recorded at Qikiqtarjuaq during scintillation on the 14th of February 2011 for a time lag of 0.15 second, PRN 15. | 133 |
| 6.2 Differential power signal recorded at Resolute Bay during scintillation (21 October 2010) for a time lag of 0.2 second, PRN 19 | 134 |
| 6.3 Differential power signal recorded at Iqaluit during scintillation on the 22nd of February 2011 for a time lag of 0.02 second, PRN 31 | 135 |

| | |
|-------------------------------------------------------------------------------------------------------------------------------------------------------------------------------------------------------------------------------------------------------------------------------------------------------------------------------------------------------------------|-----|
| 6.4 Example of Kurtosis vs temporal lag for the event at Qikiqtarjuaq during scintillation on the 14th of February 2011. Starting from a lag value of 0.02s a fast decrease in the kurtosis is observed for larger time lags. The fit is performed using the relation. $K = 4 \sinh^2 \left[\frac{1}{2} \frac{\tau_i}{\tau} \right] + 4$, with $\tau_i = 1.75s$ | 136 |
| 7.1 Illustration of mutual information against time delay obtained from the detrended power (a) and phase (b) components during the event at Qikiqtarjuaq, 2011/02/14, PRN 15. | 142 |
| 7.2 Example of a scintillation event at Qikiqtarjuaq, 2011/02/14, PRN 15. The phase space reconstruction is presented for two temporal delays ($\tau = 0.02$ s, 0.03 s), for the phase and the power components of the GPS L1 signal. | 143 |
| 7.3 Illustration of the variation of the fractal dimension with the occurrence of the power scintillation (left panel) and phase scintillation (right panel) on 01 March 2009 on PRN 20 between 03:00 and 04:00 UTC at Cambridge Bay (69.10° N 254.88° E). | 145 |
| 7.4 Probability density function of the optimum scale associated with the phase component of the signal. | 150 |
| 7.5 Probability density function of the optimum scale associated with the power component of the signal. | 152 |

| | | |
|------|---------------------------------------------------------------------------------------------------------------------------------------------------------------------------------|-----|
| 7.6 | Joint probability density function constructed for the power and phase components for the winter, summer and solstices. . . | 153 |
| 7.7 | Variation of the optimum scale with the elevation angle of the GPS satellite for the power and the phase components of the signal. | 155 |
| 7.8 | Variation of the value of the PDF at the most probable optimum scale for the power (left) and the phase (right) components. | 156 |
| 7.9 | PDF associated with the variation of the wavelet-based fractal dimension for the phase and the power components. | 158 |
| 7.10 | Normalized joint probability density function of power scintillation events characterized by $D > 0.4$ for fall (a), winter (b), spring (c), and summer (d). | 160 |
| 7.11 | Normalized joint probability density function of phase scintillation events characterized by $D > 0.2$ for fall (a), winter (b), spring (c), and summer (d). | 161 |
| 7.12 | PDF associated with the entropy variation of the phase (top panel) and the power (bottom panel) components. | 163 |
| 7.13 | Normalized joint probability density function of power scintillation events characterized by an entropy $S > 5.3$ for fall (a), winter (b), spring (c), and summer (d). | 165 |
| 7.14 | Normalized joint probability density function of phase scintillation events characterized by an entropy $S > 4.3$ for fall (a), winter (b), spring (c), and summer (d). | 166 |

| | | |
|-----|---------------------------------------------------------------------------------------------------------------------------------------------------------------------------------------------------------------------------------------------------------|-----|
| 8.1 | Illustration of different parameters of the model [Deshpande et al., 2014]. | 171 |
| 8.2 | The geometry of the GPS signal propagation from the satellite to the ground , for the north hemisphere (a) and the south hemisphere (b) [Deshpande et al., 2014]. | 172 |
| 8.3 | Example of the power and phase time series on the ground (top and bottom panels, respectively). | 176 |
| 8.4 | Illustration of the phase contour on the ground for different values of the spectral index p_H | 178 |
| 8.5 | Corresponding phase (black) and amplitude (blue) scintillation spectra observed a scintillation event. Fresnel filtering is clearly observed in the amplitude spectra while there is no Fresnel filtering in the phase spectra [Mushini, 2013]. | 180 |
| 8.6 | Illustration for the power spectra for the phase (top panel) and the power (bottom panel) components of the signal for $P_H = 4$ | 181 |

List of Symbols, Nomenclature or Abbreviations

GPS Global Positioning System

CADI Canadian Advanced Digital Ionosonde

IPP Ionospheric Pierce Point

TEC Total Electron Content

CHAIN Canadian High Arctic Ionospheric Network

PDF Probability density function

Chapter 1

Introduction and Thesis Outline

This chapter is a general introduction to ionospheric scintillation. Objectives and motivations behind the present work and a brief outline of the thesis are also provided.

1.1 Introduction

The Global Positioning System (GPS) was originally engineered by the American Department of Defence (DoD). The first satellites were launched in 1978 and declared operational for civil use in 1995. It consists of 31 satellites orbiting on a medium-Earth orbit (an altitude of 20000 km). GPS allows the user to obtain information about the time and the geographic location with

a high level of accuracy. From civilian use in navigation during commercial flights to military applications, the GPS has become one of the most important technologies in the modern era and is worth billions of dollars.

A GPS satellite emits a radio wave from an altitude of 20000 km. Hence, the signal propagates through the ionized part of the upper atmosphere (the ionosphere), which extends from approximately 90 to 1000 km. This medium presents a non-homogeneous distribution of charge and a highly dynamic aspect. Therefore, due to diffractive and refractive effects, the interaction between the trans-ionospheric radio wave and the ionospheric plasma may result in perturbations in the power and the phase components of the GPS signal and a degradation of the ranging accuracy. These disturbances can be severe enough to cause the loss of lock of the ground-based GPS receivers on the satellite signal. This phenomenon is commonly known as the ionospheric scintillation.

As the ionosphere is influenced by the radiations and the plasma outflow originating from the sun, the ionospheric scintillation can present a highly variable aspect. The fact that the state of the ionosphere depends on the solar activity detracts from the reliability of the GPS capabilities. Therefore, understanding the ionospheric scintillation is essential in mitigating the effect of the ionosphere on the GPS performances. Further, an optimum characterization of the ionospheric scintillation serves a twofold purpose, not only does it facilitate the attenuation of the scintillation effects, but also it permits an understanding of the dynamics and the morphology of the iono-

spheric plasma.

At high latitudes the ionosphere is strongly coupled to the interplanetary magnetic field via the open magnetic field lines, a fact that makes the high latitude ionosphere very sensitive to the solar activity. It is important to stress that the sun's magnetic activity presents a cycle characterized by an 11-year period. This can be reflected in the long term variation of the ionospheric plasma turbulence level. In addition, seasonal variations have also been observed [Prikryl et al., 2011].

In early studies, VHF and UHF communication systems were extensively used in the investigation of the ionospheric scintillation at mid and low latitudes. The multi-scale aspect of the ionospheric scintillation become evident. More particularly, it has been shown that the ionospheric electron irregularities producing scintillation presented a power law structure [Jones, 1960; Rufenach, 1971].

With the dawn of GPS it has been possible to have an important enhancement in terms of the spatial and the temporal coverage. Ionospheric scintillation has been extensively investigated using the GPS signal. However, for a period of time, there has been a lack of monitoring stations, equipped with ground based receivers, at high latitude regions. Given the importance of understanding the high latitude ionospheric plasma dynamics, due to the fact of its direct coupling with the IMF via the magnetic field lines, infrastructures for monitoring the ionospheric plasma have been built. Among these structures is the Canadian High Arctic Ionospheric Network (CHAIN).

In order to optimally characterize the ionospheric scintillation, the process of filtering out the non-scintillation components from the trans-ionospheric GPS signal is of primary necessity. Such unwanted components are the contributions from the diurnal variation of the electron density background and the Doppler shift induced by the relative motion of the ionospheric plasma bulk. Traditionally, the default setting of a 0.1 Hz cut-off frequency is adopted in the ionospheric scintillation studies [Forte and Radicella, 2002, 2005]. However, given the multi-fractal and the stochastic aspects of the ionospheric plasma dynamic, the adoption of a universal cut-off frequency is not a reasonable approach. There is a need to investigate the criteria for defining the optimum scale/frequency delimiting the small scale contribution, responsible for the scintillation occurrences, from the diurnal variations and the Doppler effects. This constitutes one of the objectives of the present dissertation.

The wavelet transform is revealed to be a very fruitful mathematical tool in the context of investigating the statistical properties of the ionospheric scintillation. In the present work, a wavelet based entropy is proposed and used in the statistical characterization of the ionospheric scintillation. In addition, based on the statistical behaviour of the GPS signal components during ionospheric scintillation, criteria for the delimitation of the optimum cut off frequency are defined.

The dimensionality of the ionospheric scintillation is quantified using a newly introduced wavelet based fractal dimension.

The constructed scintillation observables are used in a climatology study

of the ionospheric scintillation. Data of two years' worth of scintillation events are investigated. The corresponding scintillation maps are constructed and characterized. Conclusions are drawn about the stochasticity and the chaoticity of the ionospheric scintillation and the behaviour of the optimum cut-off scale.

Finally, a simulator of the trans-ionospheric channel is constructed. The spectral features of the observed ionospheric scintillation are reproduced.

1.2 Dissertation Outline

Chapter 2 is a general introduction to the characteristics of the sun's environment, the magnetosphere and the ionosphere. More emphasis is given to the high latitude ionospheric plasma, where different properties of its dynamics and morphology are introduced. The propagation of the radio waves in the ionosphere is also discussed.

Chapter 3 presents an introduction to the GPS and corresponding measurements. The Canadian High Arctic Ionospheric Network is also introduced.

Chapter 4 gives a general overview of the ionospheric scintillation. Different scintillation theories are discussed.

Chapter 5 introduces a new technique for the determination of the optimum cut-off scale, delimiting the ionospheric scintillation components.

Chapter 6 introduces a new model describing the intermittency of the ionospheric scintillation.

Chapter 7 presents a climatology study of the ionospheric scintillation. The stochasticity and chaoticity of the system are described. Also, the statistical behavior of the cut-off frequency is discussed.

Chapter 8 introduces a simulator of the ionospheric scintillation. Spectral properties of the observed ionospheric scintillation events are reproduced.

Chapter 9 stresses the important results of the present dissertation and provides ideas for future work.

Chapter 2

The Earth's ionosphere

The terrestrial ionosphere is sustained by the sun's activity. Indeed, the creation of free electrons in the atmosphere is mainly due to the interaction of the neutral molecules with the photons (X-rays, Extreme Ultra Violet) radiated by the sun. Superposed upon the background electron density are irregularities, ranging from different scales, created by different physical mechanisms (introduced in the following text).

2.1 Solar atmosphere

2.1.1 The internal and atmospheric structure

The sun's structure comprises of two major parts: the internal structure and the atmosphere. The first part is divided into three layers: the core, the radiative and the convective zones.

All thermonuclear reactions take place in the core, producing gamma rays and raising the temperature up to $15 \cdot 10^6$ K. This part extends to approximately the third of the solar radius, where begins the transition zone called the radiative zone. At the top of the internal structure is the convective zone which extends from about 70% of solar radius to the surface of the sun.

The solar atmosphere is divided into three layers: the photosphere, the chromosphere and the corona, presenting a particular temperature profile, figure 2.1. The photosphere constitutes the coldest region of the sun (about 6000 K) and is situated at the lowest height. It is the source of the light in the visible spectrum. This region comprises convection cells of ionized matter called granules, where intense magnetic fields are confined. Also, the photosphere comprises cold regions, characterized by intense unipolar magnetic fields, called sunspots. These are the coldest regions in the sun (4000 K).

The chromosphere is the region situated just above the photosphere and presents a temperature profile directly proportional to the altitude. It is characterized by monochromatic emissions of the electromagnetic radiation corresponding to specific emission lines, such as the red line of hydrogen (H), ultraviolet line of calcium (CAIIH) and the Lyman- ultraviolet line, among others. One of the interesting features of this layer are the prominences, which are basically bright regions surrounding sunspots, corresponding to dense and cooler regions which follow the magnetic loops emerging from the photosphere.

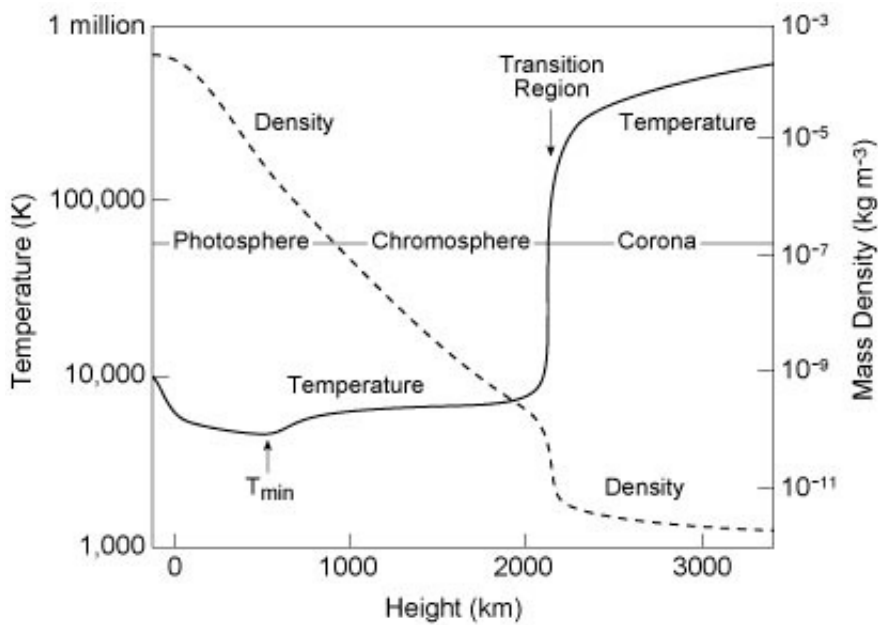


Figure 2.1: Temperature profile at the surface of the sun. Courtesy: National Center for Atmospheric Research (NCAR).

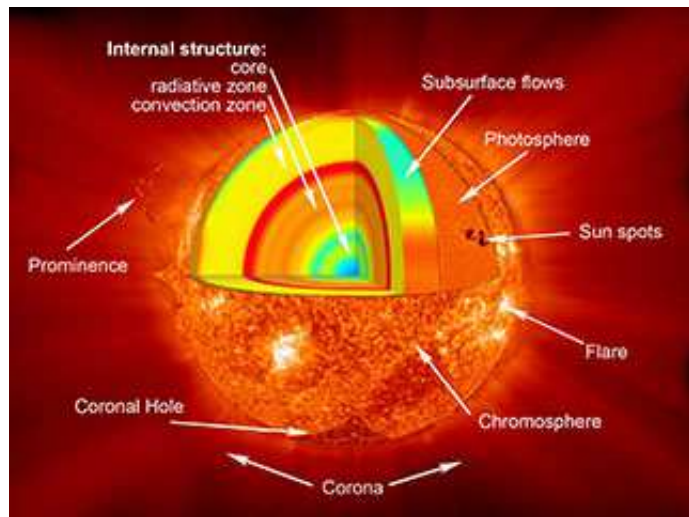


Figure 2.2: Structure of the Sun [<http://solarsystem.nasa.gov>].

The corona is the outermost layer of the solar atmosphere and the least dense. It presents a temperature profile similar to the chromosphere's, with temperature reaching several millions of degrees. As a result, the electrons and the protons escape from the gravitational field of the sun to constitute a continuous stream of plasma, the solar wind.

2.1.2 Solar cycle

The solar dynamo (the turbulent plasma located in the core of the sun) induces an activity cycle called the solar cycle, which on average presents a period of 11 years. Different indices have been constructed in order to monitor the solar activity; for example, we cite the International Sunspot Number, which gives an estimate of sunspots and groups of sunspots observed on the photosphere. Another index is $F_{10.7}$, the radio flux at wavelength 10.7 cm, observed daily at the radio station of Penticton, Ottawa (Canada) since 1950. Other indices have been defined to quantify the activity of the sun, such as the Total Solar Irradiance [de Toma et al., 2001] and MgII [de Toma et al., 1997].

The period of rotation of the Sun on its axis is approximately 25 days at the equator and about 35 at the poles. This results from a differential aspect of the solar rotation. The synodic rotation period, which is the rotation period of the sun from the earth's point of view, lasts 27.3 days.

The solar wind is an outflow of plasma originating from the expansion of the solar corona up to the limits of the interstellar space. This medium is characterized by a very large conductivity. Therefore, the Interplanetary Magnetic Field (IMF), which corresponds to the extension of the solar magnetic field in the interplanetary medium, is highly coupled to the plasma. This property can be visualized in the “frozen” in aspect, where we can describe the system as magnetic field lines frozen in the plasma flow. The solar wind has a typical density of the order of few electrons per cubic centimeter, and a flow velocity, v , of approximately $400 \text{ km} \cdot \text{s}^{-1}$.

2.2 Solar Activity

2.2.1 Co-rotating Interaction Region

Typically, during solar minimum, the coronal holes are located at the high latitude regions of the sun. The equatorial region, on the other hand, presents a “quiet” state, where low speed solar wind is blown outward from the sun. When the solar activity is high, coronal holes migrate towards the equator and, subjected to the rotation of the sun, produce solar wind emissions that present an intermittent aspect in terms of slow and fast wind emissions. Thus, it is possible to have an interaction between a fast and a slow wind producing a shock region called the Co-rotating Interaction Region (CIR), Figure 2.3. The latter is bounded by a forward shock and a reverse shock. As the occurrence of CIRs is dependent on the solar activity, it can be foreseen

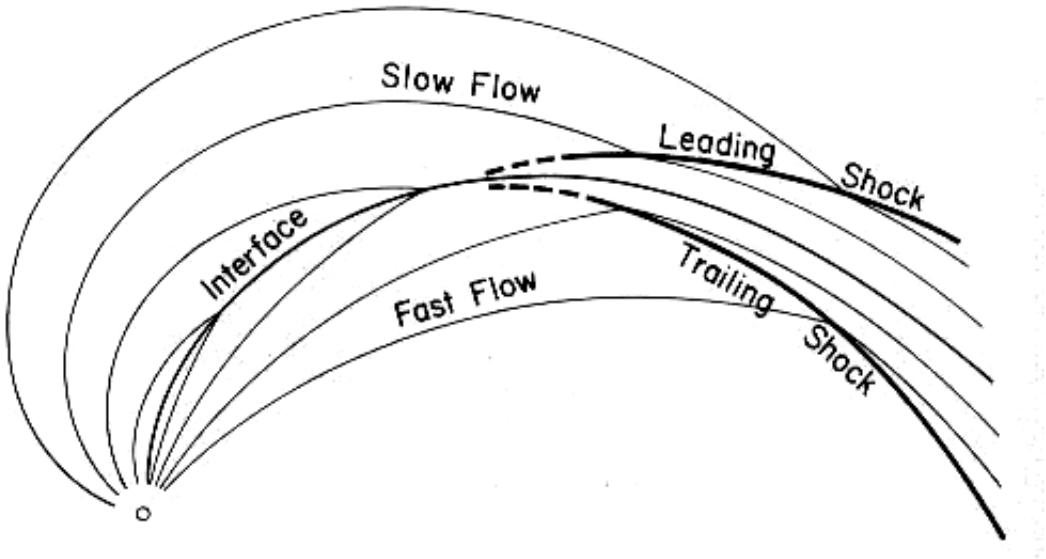


Figure 2.3: Illustration of the Co-rotating Interaction Regions (CIRs). Courtesy: National Center for Atmospheric Research (NCAR).

by monitoring IMF and solar wind parameters.

2.2.2 Coronal Mass Ejections (CMEs)

These are caused by a mechanism called magnetic reconnection, where magnetic energy is released and transformed into kinetic energy. Indeed, closed magnetic loops on the surface of the sun, confining a plasma, are stressed via motion of their photospheric footprints; this induces a tear of the field lines connecting to the sun. The plasma is then released, and magnetic buoyancy forces the plasma blob to accelerate quickly away from the Sun. The propagation speed of CMEs lies anywhere from near zero to 2000 km/s . Fast CMEs plow into the solar wind and can form shock waves, while slow CMEs

flow with the solar wind.

2.2.3 Flares

A solar flare consists of a burst of electromagnetic radiation from the chromosphere near a sunspot, lasting for a period ranging from minutes to hours. The emission can be in different ranges of the spectrum, including hard X-rays and γ -rays (bremsstrahlung), soft (thermal) X-rays and EUV (multi-million degree K gas) and radio bursts (energetic electrons in magnetic fields). During a solar flare, a large quantity of energy is released from a small volume in a short period of time. This requires either a large amount of energy stored in that small volume that can be quickly transformed and released as energetic electrons and photons or very efficient transport of energy into that volume where it is then converted into the observed forms. In the solar environment, an important amount of energy is available in the form of magnetic energy. In order to convert the stored energy into particle energy and heat, a rapid mechanism of conversion is needed. This is where the magnetic reconnection comes into play.

2.3 Magnetosphere

The earth's magnetic field can be, to a first approximation, considered as a dipole with the pole tilted, with respect to the axis of rotation of the earth,

with an angle of 11° . Put in a more illustrative way, the magnetic pole is tilted toward North America in the northern hemisphere. The field at the surface of the earth varies between 0.25 Gauss at the magnetic equator to 0.6 Gauss near the magnetic poles.

This picture of the earth's magnetic field represented by a magnetic dipole is rather a simplistic illustration. Indeed, the earth is immersed in a hot bath constituted of a collisionless plasma outflowing from the sun (the solar wind). Additionally, the solar wind is supersonic, as it is subject to heating by the sun, and, due to the sun's gravitational field, compression and subsequent expansion. This results in a complex interaction region in the interface between the magnetic field of the earth (magnetosphere) and the solar wind, as illustrated in Figure 2.4.

A considerable amount of the energy carried by the IMF finds its way into the ionosphere, especially, via the magnetic field lines, where it triggers aurora displays; also, it energizes the plasma on the magnetic field lines, creating a vast circulating current of hot plasma in the upper atmosphere.

In order to have a picture of how the inflowing stream of plasma interacts with the shielding magnetic field of the earth, let us suppose that the solar wind is sub-sonic and write the equation describing the motion of a charged particle in the presence of a magnetic field. A particle of charge q (element of the solar wind) immersed in a magnetic field (earth's magnetic field) is

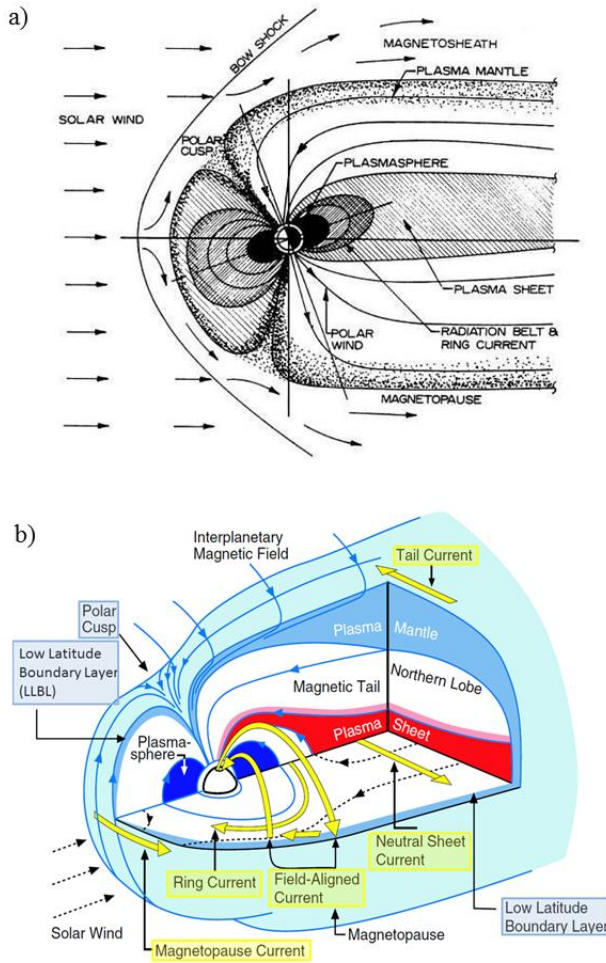


Figure 2.4: Diagram showing the basic structure and electric current systems of the magnetosphere for an observer situated a) at dusk in the Sun-Earth plane [Hunsucker and Hargreaves, 2003] and b) in the afternoon sector above the Sun-Earth plane [De Keyser, 2005].

subject to the Lorentz force:

$$\vec{F} = q\vec{v} \times \vec{B} \quad (2.1)$$

Due to the polarity of the earth's magnetic field, the ions are deflected towards dusk and the electrons towards dawn. This creates a net dawn to dusk current, inducing a magnetic field parallel to the earth's field in the region between the current sheet and the earth and an anti-parallel field in the region of the solar wind. Therefore, the magnetic field is strengthened in between the current sheet and the earth and cancels out in the region of the solar wind. Let us now consider a more realistic configuration. As the solar wind is supersonic, a bow shock forms upstream of earth, and the solar wind plasma and magnetic field are slowed and compressed between the current sheet (magnetopause) and the solar wind, the so-called magnetosheet region; the ion and electron temperature rises to ≈ 50 eV and ≈ 200 eV, respectively. Therefore, the plasma in the magnetosheet region flows around the Earth's magnetic field, compressing the dayside and extending the magnetosphere on the nightside.

When the interplanetary magnetic field has a southward component, the process known as magnetic reconnection takes place: the southward component of the interplanetary magnetic field cancels out with the northward component of the Earth's magnetic field, opening the dayside of the magnetopause. The solar wind plasma flows around the magnetosphere and drives convec-

tion patterns.

A magnetized plasma is characterized by the parameter β , which is defined as the ratio of the plasma pressure, $p = nK_B T$, to the magnetic pressure, defined as $\frac{B^2}{2\mu_0}$, i.e., $\beta = \frac{2\mu_0 p}{B^2}$.

Based on the value of β and the magnetic field topology, one can define different plasma regions in the Earth's magnetosphere; the tail lobes are characterized by a low β value (< 0.01). This region is threaded by magnetic field lines extending from the polar cap to hundreds of R_E (R_E being the Earth radius, $1R_E = 6370$ km) tailward. Having an opposite magnetic field direction, the tail lobes contains a high density ($0.1 - 1 \text{ cm}^{-3}$), high temperature ($T_i \approx 2\text{-}20 \text{ keV}$, $T_e \approx 0.4 - 4 \text{ keV}$) plasma, originating from the solar wind and the ionosphere. The plasma carries a current sheet, termed the neutral sheet, because the magnetic field reverses and the magnitude becomes very small ($< 5 \text{ nT}$). A thin layer of plasma, termed the plasma sheet boundary layer, is observed between the lobes and the plasma sheet. This region comprises field aligned ion and electron populations. The mapping of these plasma regions constitute the main part of the nightside auroral oval (introduced in the following sections of the text).

2.4 Morphology of the ionosphere

The ionosphere is the ionized component of the atmosphere, extending from the altitude of 60 km to approximately 1000 km. Due to the effect of gravity, the ionosphere is horizontally stratified and can be characterized by an electron density profile. A typical density profile of the high-latitude ionosphere is given in Figure 2.5. The ionosphere is considered to be a weakly ionized plasma because the electron and ion densities are estimated to be a thousand times smaller than the neutral fluid density. The electron density for a certain volume of the ionosphere is a result of different processes: production, loss and transport, as illustrated by the continuity equation,

$$\frac{\partial N_e}{\partial t} = q - L - \vec{\nabla} \cdot (N_e \vec{v}) \quad (2.2)$$

where N_e is the electron concentration while q and L represent the production and the loss rates, respectively. The term \vec{v} is the mean plasma velocity. The production is the result of ionization of different neutral components of the atmosphere by solar radiation. The loss is the result of the recombination of electrons with positive ions. The vertical structure of the ionosphere can be characterized by three different layers. In each of these layers, specific chemical reactions, describing the process of loss and production, take place. This results in a local peak in the plasma density. In the following we describe the three main layers of the ionosphere.

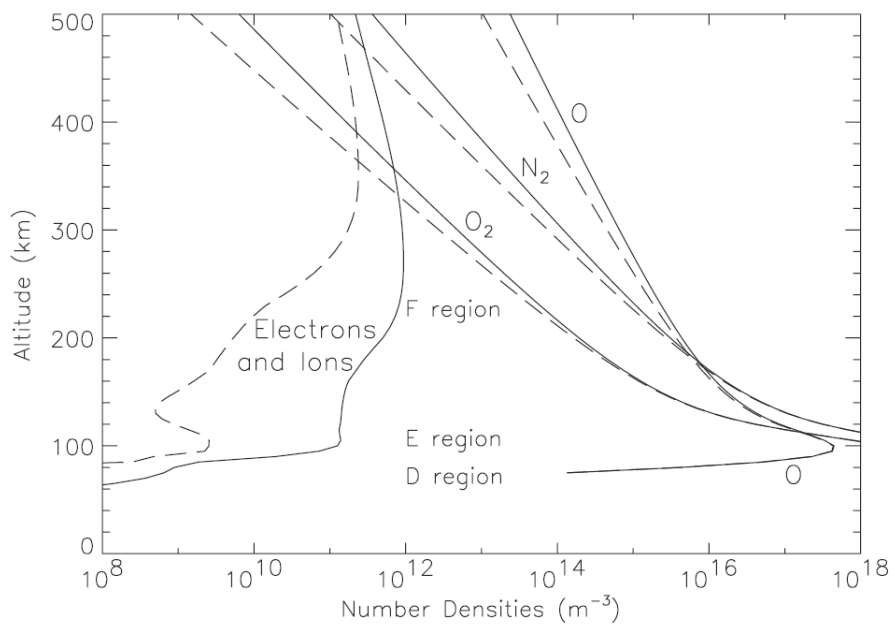


Figure 2.5: Typical ionospheric profile and its neutral elements composition, where dashed and solid lines represent the profile during day and night, respectively [Kelley, 2009].

2.4.1 D layer

The D layer is the lowest layer of the ionosphere (60-90 km) composed mainly of molecular ions, such as O_2^+ and N_2^+ . These ions are the product of direct ionization of neutral molecules, such as O_2 and N_2 , by cosmic rays or solar X-rays (between 1 and 10 Å). Above 70 km, NO^+ is produced by Lyman- α radiation at 1216 Å which leads to the D peak. The electron concentration in the D-layer ranges between 10^7 and $10^{10} e^-/m^3$. Due to a high recombination rate of O_2^+ and N_2^+ ions, this layer exists only during day time.

2.4.2 E Layer

The E layer is produced at heights ranging from 90 km to 130 km. Due to its reflective properties at low radio frequencies, this layer was the first to be discovered ¹. The majority of the neutrals at these altitudes are the N_2 and O_2 molecules. Direct ionization of these molecules, in addition to charge exchange, produces NO^+ and O^+ . The electron concentration in the E layer lies between 10^{10} and $10^{11} e^-/m^3$.

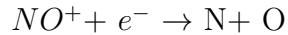
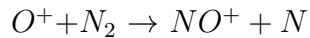
2.4.3 F Layer

This layer is the only one that is permanent. It extends from 130 km to 1000 km. The neutral constituents at these altitudes are N_2 and the atomic oxy-

¹The reflective properties of the ionosphere will be introduced in section 2.5

gen O. Ion production in this region is due to ionization of the atomic oxygen by the Far Ultraviolet (FUV) and Extreme Ultraviolet (EUV) radiations. The F layer can be characterized by two sub-layers, F1 and F2, that exhibit specific photochemical reactions.

- The F_1 layer is defined in the range 130 km-200 km. It usually merges with the F_2 layer during night periods when production is not sustained by the solar radiation.
- The F_2 region is characterized by the highest electron density in the ionosphere. It extends from the F_1 layer to the approximate height of 1000 km. The main neutral constituent at these heights is the atomic oxygen, O, which is transformed to atomic ions by photo-ionization. The rate of recombination being still proportional to N_2 and O_2 ,



the loss of O^+ by recombination is lower than that found at the F_1 layer heights. Different ionization processes are summarized in Figure 2.6.

2.4.4 Transport

In the D, E, and F_1 layers, the concentration of neutral molecules is high and so are the collision cross sections between the neutral elements and the ions

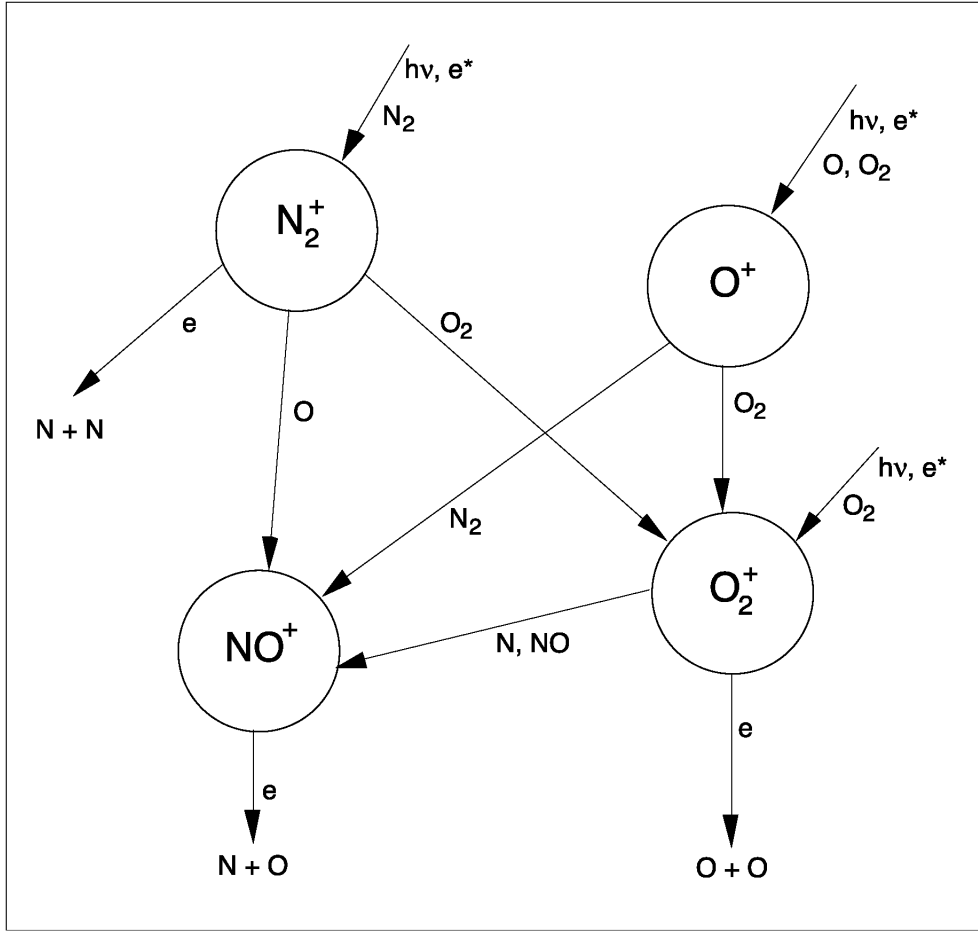


Figure 2.6: Illustrations of thermospheric heating and the ionization processes for different elements of the ionosphere. Photon flux enters the atmosphere and ionization processes convert photon energy to chemical potential energy.

as well as the recombination rates. Therefore, the motion of the electrons and ions is primarily driven by the background neutral wind. In this case the last term in equation 2.2 can be neglected, and the continuity equation can be expressed solely by the production and the loss terms. The layers are

said to be in the so-called state of photochemical equilibrium.

On the other hand, at the F_2 layer, the concentration is low, constraining the electron and the ions to the geomagnetic topology, except for the $\vec{E} \times \vec{B}$ drift, where the electrons are free to move across the magnetic field lines. In this case, the transport term, in equation 2.2, cannot be neglected. Let us give a simple illustration of the influence of electric and magnetic fields on the motion of charged particles.

In the presence of magnetic and electric fields, \vec{E} and \vec{B} , a particle with charge q is subject to the Lorentz force, given by:

$$\vec{F} = q(\vec{E} + \vec{v} \times \vec{B}) \quad (2.3)$$

where \vec{v} is the velocity of the particle. In the absence of an electric field, the motion of the particle is helicoidal, as a result of two motions: the parallel translation along \vec{B} due to the particle's velocity \vec{v} and, even if the particle does not have an initial velocity component along the magnetic field, the rotation of the particle about the magnetic field \vec{B} .

The Larmor radius, describing the circular motion in the plane perpendicular to the magnetic field \vec{B} , can be easily computed, considering a circular motion:

$$F_L = ma = m \frac{v_\perp^2}{r_L} = |q|v_\perp B \implies r_L = \frac{mv_\perp}{qB} \quad (2.4)$$

where m is the mass of the particle and v_\perp its velocity, perpendicular to the magnetic field. The acceleration of the particle is represented by a.

The corresponding angular velocity is given by $\omega_L = \frac{q}{m}B$. The so-called gyrofrequency is defined as:

$$f_L = \frac{\omega_L}{2\pi} = \frac{|q|B}{2\pi m} \quad (2.5)$$

From equation 2.5 it is clear that the gyrofrequency depends on the mass of the charged particle. In the presence of an electric field the guiding center of the helix drifts at a velocity:

$$\vec{v} = \frac{\vec{E} \times \vec{B}}{B^2} \quad (2.6)$$

From equation 2.6, it is clear that the drift velocity is independent of both the sign and magnitude of the particle's charge. Therefore, the electrons and the positive ions drift at the same speed in the presence of an electric field, in the case where the collisions can be neglected ².

2.4.5 Ambipolar Diffusion

Another mechanism, contributing to the dynamics of the polar ionospheric plasma, is worth mentioning here. As a result of the equilibrium between the pressure gradients and the gravitational forces, the ions and electrons

²This condition is met when the electron-ion, electron-neutral and ion-neutral collision cross sections are small. This is typically the case in the ionosphere at heights above 130 km.

are subject to diffusion. However, in order to maintain the total charge-neutrality of the ionospheric plasma, they need to diffuse at the same rate. This mechanism is called ambipolar diffusion. At the F_2 layer, where the concentration is weak, the charged particles follow the magnetic field lines. The fact that these lines are quasi perpendicular to the horizontal in the polar and high latitude regions, makes the ambipolar diffusion a maximum at these regions, playing an important role in the dynamics of the ionospheric plasma.

2.5 Radio Waves in the Ionospheric Plasma

In the context of the propagation of radio waves in the ionosphere, it is of fundamental importance to understand the characteristics of the ionospheric plasma. The latter, being magnetized, presents peculiar optical properties. In fact, the electrons and ions, primarily constrained by Earth's magnetic field due to the Lorentz force, move along the magnetic field lines. This asymmetric geometry induces a spatial asymmetry in the dielectric function, $\epsilon(x, y, z)$, which in turn leads to birefringence. Figure 2.7 illustrates the propagation of the radio-wave in the geomagnetic field.

Sir Edward Appleton was one of the first pioneers to work on the derivation of the refractive index formula for a medium with a complex charge density distribution, such as the ionosphere.

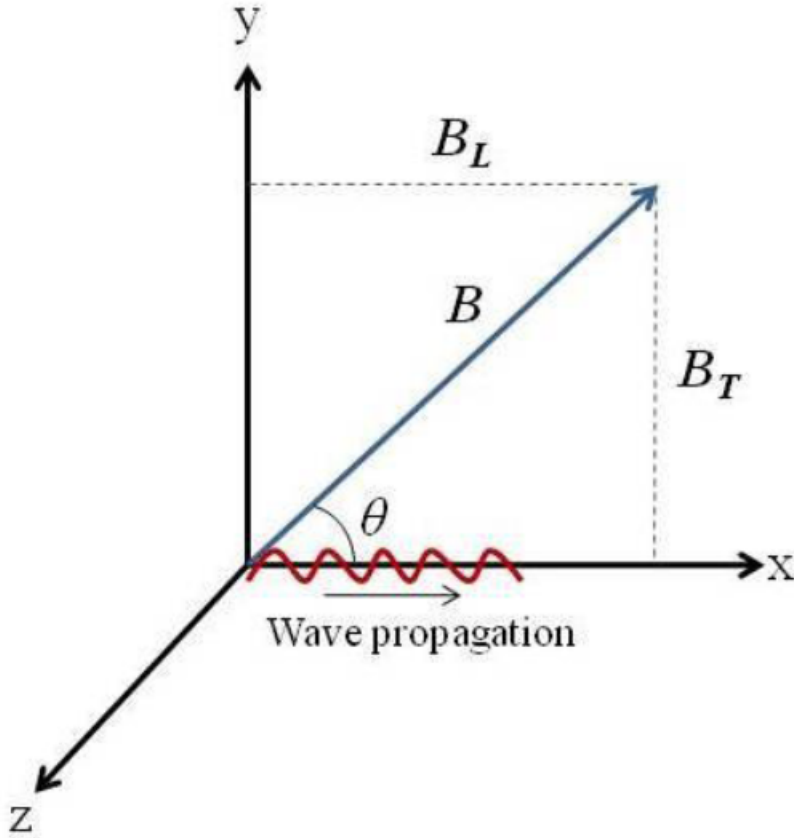


Figure 2.7: Orthogonal coordinate system for a propagating radio-wave. The geomagnetic field lies in the x-y plane [Mushini, 2013].

Let us cite Appleton formula, giving the refractive index [Davies, 1990]:

$$n^2 = 1 - \frac{X}{1 - iZ - \frac{Y_T^2}{2(1-X)} \pm \sqrt{\frac{Y_T^4}{4(1-X-iZ)^2} + Y_L^2}} \quad (2.7)$$

where the following changes of variables have been performed: $X = \frac{Ne^2}{\epsilon_0 m \omega^2}$, $Y_T = \frac{eB_T}{m\omega}$, $Y_L = \frac{eB_L}{m\omega}$, $Z = \frac{\nu}{\omega}$.

The parameter ν is the electron-neutral frequency and N_e is the electron number density. The parameters ω and m represent the wave frequency and the mass of the electron, respectively. The two projections of the magnetic field \vec{B} along the x and y axis are given respectively by B_T and B_L .

In the case where we ignore the magnetic field and the collisions, the refractive index, also referred to as the phase refractive index, can be given as:

$$n_{ph}^2 \approx 1 - \frac{1}{2}X \quad (2.8)$$

Substituting the value of X:

$$n_{ph}^2 \approx 1 - \frac{40.3N}{f^2} \quad (2.9)$$

From 2.9, we can write the phase velocity as follow:

$$V_{ph} = \frac{c}{n} = c \left[1 - \frac{Ne^2}{m\epsilon_0\omega^2} \right]^{-\frac{1}{2}} \quad (2.10)$$

From inspection of 2.10, it is clear that the phase velocity is dependent on the frequency of the propagating wave. Therefore, the ionospheric medium is said to be dispersive. This means that if two waves, presenting slightly different frequencies, propagate in the ionospheric plasma, they will have different propagation velocities. The interference pattern of these two waves will determine the characteristics of propagation of the composite wave, i.e., the velocity of propagation of the energy (group velocity) and its direction of

propagation. Practically, we can obtain such characteristics by modulating the wave. We talk then about the propagation of the modulation envelope. In order to give a classical illustrative example, let us consider the superposition of two different traveling harmonic waves, ψ_1 and ψ_2 , presenting a slight difference in frequency and wavenumber, denoted by $\delta\omega$ and δk , respectively.

$$\psi_1 = \cos(kx_1 - \omega t) \quad (2.11)$$

$$\psi_2 = \cos((k + \delta k)x_1 - (\omega + \delta\omega)t) \quad (2.12)$$

$$\psi = \psi_1 + \psi_2 = 2 \cos\left(\frac{1}{2}(x_1\delta k - t\delta\omega)\right) \cos\left[\left(k + \frac{\delta k}{2}\right)x_1 + \left(\omega + \frac{\delta\omega}{2}\right)t\right] \quad (2.13)$$

The result is referred to as the “beat” signal, and its envelope is given by:

$$E = 2 \cos\frac{1}{2}(x_1\delta k - t\delta\omega) \quad (2.14)$$

The velocity of propagation of the envelope is given by the group velocity as follows:

$$V_g = \frac{\delta\omega}{\delta k} \quad (2.15)$$

In our context, it is convenient to define a group refractive index:

$$n_g = \frac{c}{V_g} = c \frac{\delta k}{\delta\omega} = c \frac{d}{d\omega} \left(\frac{2\pi}{\lambda} \right) = \frac{d}{d\omega} (n_{ph}\omega) = n_{ph} + \omega \frac{\delta n_{ph}}{\delta\omega} \quad (2.16)$$

Substituting in 2.9, one gets the expression for the group refractive index:

$$n_g \approx 1 + \frac{40.3N}{f^2} \quad (2.17)$$

This discrepancy between the phase and the group refractive indices, is the building block of the techniques used in the present thesis.

2.6 The High Latitude Ionosphere

The high latitude ionosphere is characterized by its coupling with the magnetosphere and the interplanetary magnetic field (IMF) via the “open” magnetic field lines. These lines are connected to the magnetosheet and the solar wind, which means that they are connected to the Earth’s surface on one end and to the IMF on the other, as opposed to the closed magnetic field lines, that have both footpoints on the earth. This property, in addition to the topology of the magnetic field lines at these latitudes, which are quasi perpendicular to the surface, makes the polar ionosphere very peculiar and different from its low latitude counterpart. In particular, for example, the precipitation of the energetic particles from the solar wind along the magnetic field lines plays a crucial role in the dynamics and the morphology of the polar ionospheric plasma. On the other hand, due to the fact that the magnetic field lines are parallel to the gravitational field, the role played by the gravitational forces is not the same as for the case of the low latitude

regions, where the gravitational field is perpendicular to the magnetic field. Indeed, the effect of the gravitational field can be ignored for the charged particles, as the electromagnetic forces dominate; only gravitational forces acting on the neutrals are taken into consideration.

The high latitude ionosphere is characterized by two main regions, namely, the polar cap and the auroral oval regions. The auroral oval is defined as the transition region between the so-called closed and open magnetic field lines. In this region, energetic particle precipitation, originating from the magnetospheric field lines, is predominant. These particles are thought to be originating from the reconnection of the IMF at the magnetotail. Different observable phenomena result from these energy injections, such as, the luminous auroral Borealis/Australis, geomagnetic field disturbances and X-ray radiation. Boundaries of the auroral oval vary with the geomagnetic activity as illustrated in Figure 2.8, where the most intense auroral emissions are represented by the dotted regions. In general, the auroral zone is defined as being centered approximately 23° from the geomagnetic poles with a width of approximately 10° . The auroral oval consists of a continuous band centered at approximately 67° magnetic latitude at magnetic midnight and about 77° at magnetic noon during quiet and moderate geomagnetic activity.

The polar cap, enclosed by the auroral oval, is characterized by open magnetic field lines that are directly connected to the IMF; the polar cap is therefore directly coupled to the solar wind and the solar activity. In the case of a

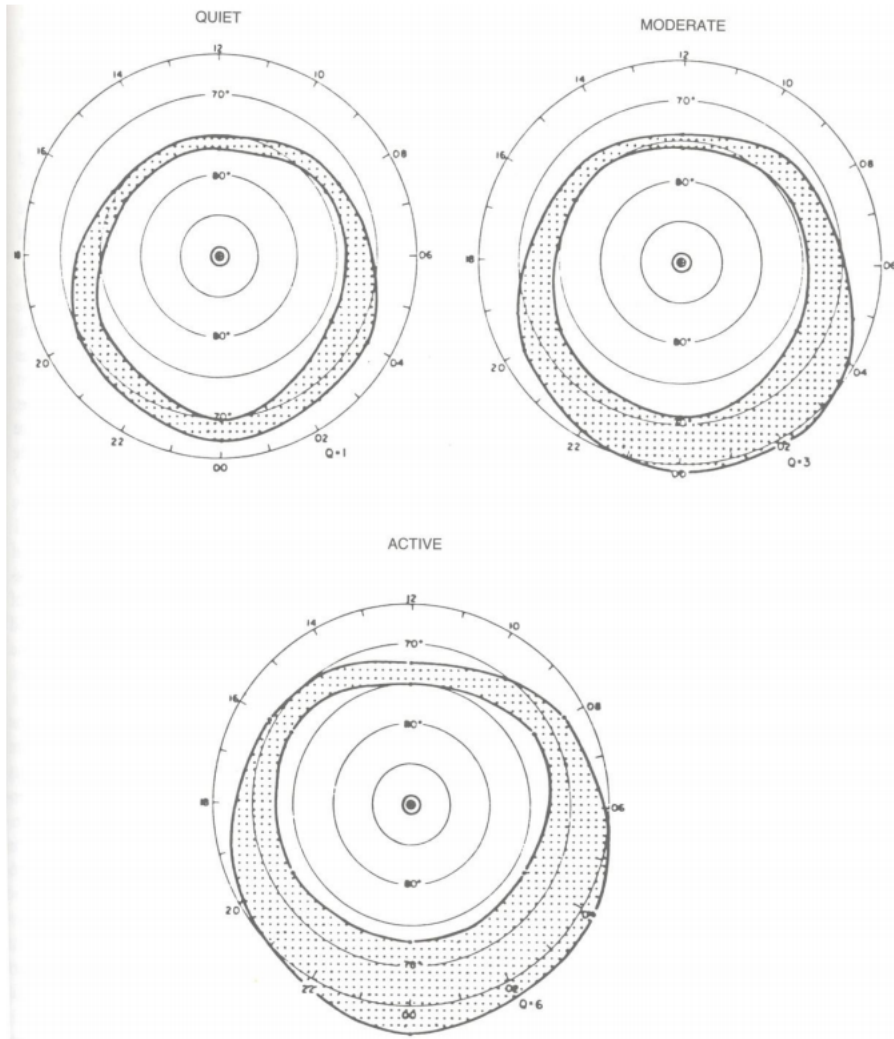


Figure 2.8: Statistical locations of auroral activity during periods of quiet, moderate and high geomagnetic activity. Data are from all-sky camera images [Kivelson and Russell, 1995]

southward IMF, the solar wind will induce an electric field $\vec{E}_{sw} = -\vec{V}_{sw} \times \vec{B}_{sw}$ where the plasma is collisionless, characterized by a high conductivity. The electric field is then mapped down the equipotential magnetic field lines to the ionosphere and generates an $\vec{E} \times \vec{B}$ drift of the plasma at a velocity $\vec{V} = \vec{E} \times \vec{B}/B^2$, with values ranging from 200 m/s to 300 m/s during quiet geomagnetic activity and reaching as much as 1500 m/s on a day of high geomagnetic activity.

2.6.1 The characteristics of the ionospheric conductivity

Two mechanisms come into play in the control of the ions' motion, namely, the collision and the magnetic force. In the E layer and below, the medium is resistive and the collisions between the ions and the neutrals predominate; while above, in the F layer, the plasma is non-resistive and the motion of the ions is dictated by the magnetic field. As a result of all these physical mechanisms, the conductivity has different components in the different layers of the ionospheric plasma. In general, the ionospheric current density \vec{J} is written as [Kelley, 2009]:

$$\vec{J} = \begin{bmatrix} \sigma_1 & \sigma_2 & 0 \\ -\sigma_2 & \sigma_1 & 0 \\ 0 & 0 & \sigma_0 \end{bmatrix} \begin{bmatrix} E_x \\ E_y \\ E_z \end{bmatrix}$$

where the different components of the conductivity are given by:

$$\sigma_1 = \left[\frac{1}{m_e \nu_{en}} \left(\frac{\nu_{en}^2}{\nu_{en}^2 + \Omega_e^2} \right) + \frac{1}{m_i \nu_{in}} \left(\frac{\nu_{in}^2}{\nu_{in}^2 + \Omega_i^2} \right) \right] N_e e^2 \quad (2.18)$$

$$\sigma_2 = \left[\frac{1}{m_e \nu_{en}} \left(\frac{\nu_{en} \Omega_e}{\nu_{en}^2 + \Omega_e^2} \right) + \frac{1}{m_i \nu_{in}} \left(\frac{\nu_{in} \Omega_i}{\nu_{in}^2 + \Omega_i^2} \right) \right] N_e e^2 \quad (2.19)$$

$$\sigma_0 = \left[\frac{1}{m_e \nu_{en}} + \frac{1}{m_i \nu_{in}} \right] N_e e^2 \quad (2.20)$$

with

m_e and m_i representing the electron and ion masses, respectively;

ν_{en} and ν_{in} the electron-neutral and ion-neutral collision frequencies, respectively; Ω_e and Ω_i the gyrofrequencies of the electron and the ion, respectively.

The quantity σ_1 is called the Peterson conductivity, and is defined as the conductivity along the applied electric field. The component σ_2 is the conductivity perpendicular to the direction of the applied electric field, and is called the Hall conductivity. Finally, the quantity σ_0 is the longitudinal conductivity and is defined in the case of an applied electric field parallel to the magnetic field. In this case, the conductivity depends only on the collision frequencies. In Figure 2.9, the variation of the ionospheric conductivity with height is illustrated.

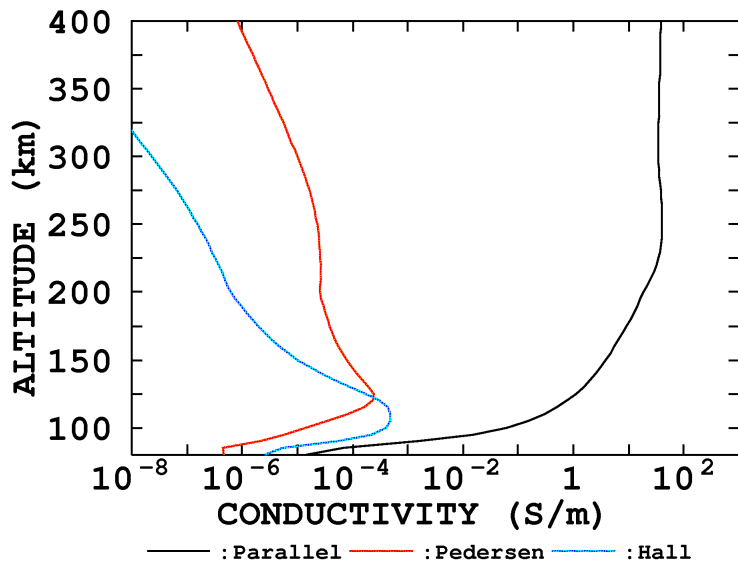


Figure 2.9: Example of the ionospheric conductivity profile: illustration of the variation of the different components of conductivity with height in mid-latitude ionosphere during day time. Courtesy: National Center for Atmospheric Research (NCAR)

2.6.2 Sources of the ionospheric irregularities at high latitudes

Different mechanisms contribute to the configuration and morphology of the electron density distribution in the high latitude region of the ionosphere. The electron density irregularities can be formed via plasma processes, plasma instabilities, particle precipitation and neutral fluid turbulence.

Particle precipitation is very important in the high latitude region, due to the open magnetic field lines characterizing it, and the possibility for charged particles from the solar wind to map down the magnetic field lines and penetrate the ionosphere.

Plasma instabilities can be a source of irregularities in the E and F regions of the ionosphere. Indeed, various sources of free energy are available at these altitudes; for example, the difference in the ion-neutral and electron-neutral collision cross sections leads to non-zero currents, which are a source of free energy. Also, velocity shears and density gradients can constitute sources of free energy. We talk about a micro-instability when the wavelength, characterizing the fluctuations of the electron density, is of a size $\lambda < r_L$, where r_L is the Larmor radius, defined by 2.4. Else, the mechanism is considered as macro-instability. In the following, we discuss various instability mechanisms occurring in different layers of the ionosphere.

2.6.2.1 Particle Precipitation

This mechanism plays a major role in the formation of the electron density irregularities in the polar region. Electrons of energies ranging from 10^2 to 10^3 eV deposit all their energy at the F layer. This results in the formation of spatial and temporal variations in the electron fluxes in the ionospheric plasma. Dyson [1974] showed a good correlation between the low energy electrons fluxes and the electron densities in the cusp region [Dyson and Winningham, 1974]. Kelley [1982] correlated low energy electron precipitation and the formation of large scale ($\lambda > 10$ km) irregularities at the high latitude F layer and found that the power spectra of the electron density fluctuation could be described by a power law of the form $k^{-1.89}$ [Kelley et al., 1982].

Large scale magnetic field aligned convecting structures have been observed in the auroral F region and have been associated with diffuse aurora particle precipitation and the corresponding field aligned currents [Vickrey et al., 1980]. Also, it has been found that the scale of the plasma enhancements, observed along the north south axis, are comparable to the outer scale of the electron irregularities structures associated with the auroral F region particle precipitation [Kelley et al., 1982].

2.6.2.2 Gradient drift instability

This instability, also known as cross field instability, occurs whenever there is an enhancement of the plasma density due to a driving mechanism, such as

electric fields or neutral winds; a disturbance can take place via separation of charges. The induced polarization electric field, $\delta\vec{E}$, and the presence of the ambient magnetic field lead to a $\delta\vec{E} \times \vec{B}_0$ drift, which disturbs the plasma density, creating an unstable configuration. The mechanism of the gradient drift instability, in the F and E regions, is illustrated in Figure 2.10.

In the F region, the ions drift parallel to the electric field, due to the Pederson conductivity, and the electrons in the opposite direction. This will create a separation of charge, and the resulting alternating polarization electric field will induce drifts of the plasma, creating an unstable configuration when the density gradient is perpendicular to the electric field \vec{E} .

In the E region, when the electric field \vec{E} is parallel to the plasma density gradient, $\vec{\nabla}n$, the condition for the gradient drift instability is met. The electrons will drift perpendicularly to the electric field (due to the Hall conductivity), while the ions will move along the direction of the electric field (due to the Pederson conductivity). This will create a space charge and a polarization electric field, which will induce $\delta\vec{E} \times \vec{B}$ drifts increasing the amplitude of the disturbance into an instability.

2.6.2.3 Kelvin-Helmholtz Instability

This instability occurs at the interface of two adjacent flows characterized by different velocity profiles. To give an example of such a mechanism, let us consider the case where a jet of fluid is injected into a stationary fluid; the instability will induce a conversion of the kinetic energy of its directed

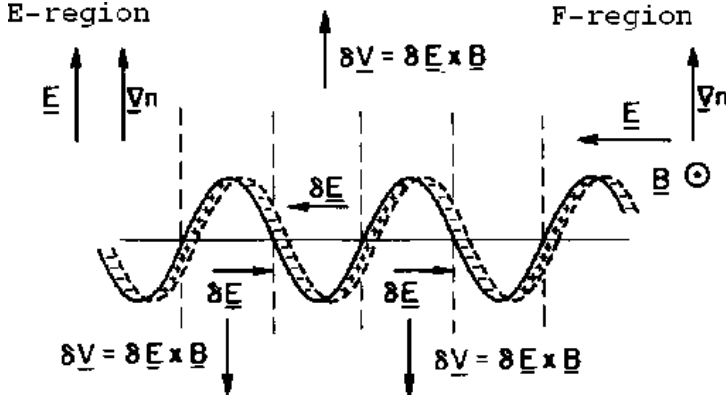


Figure 2.10: Gradient drift instability mechanism in the E and F regions of the ionosphere [Tsunoda, 1988].

motion into a turbulent state characterized by vortex formation.

2.6.2.4 Farley Buneman instability

This instability occurs in the case where the differential current due to the relative velocity between ions and electrons exceeds a threshold determined by the ion acoustic speed, given by:

$$C_s = \sqrt{\frac{k_B(T_i + T_e)}{m_i}} \quad (2.21)$$

where T_i , T_e are the ion and electron temperatures, respectively. the parameter m_i is the ion mass. This instability is also called the two stream instability. This latter produces waves that propagate nearly perpendicular to the magnetic field. The cone of angle within which the propagation occurs

is given by

$$\cos\theta = \frac{C_s}{V_d}(1 + \Psi) \quad (2.22)$$

where

$$\Psi = \frac{\nu_e \nu_i}{\omega_e \omega_i} (\sin^2 \alpha + \frac{\omega_e^2}{\nu_e^2} \cos^2 \alpha) \quad (2.23)$$

V_d represents the relative drift speed between electrons and ions, α is the angle between the propagation direction of the wave and the magnetic field. The parameters ν_e , ν_i and ω_e , ω_i represent the collision and gyro-frequencies for the electrons and the ions, respectively.

In the E region, due to the fact that the cross section of ion-neutral collision is large, the ions are unmagnetized and experience a Pedersen drift parallel to \vec{E} . On the other hand, the electrons are magnetized and experience a Hall drift perpendicular to the electric field \vec{E} . It results in a finite relative speed between the ions and the electrons and a high probability for the instability to be triggered. However, in the F region, both electrons and ions are magnetized with no relative velocity, and consequently the conditions for the instability are not met.

2.7 Monitoring the ionosphere

High Frequency (HF) and Ultra High Frequency (UHF) electromagnetic waves are usually used in sounding the ionosphere (except for in-situ measurements made by orbiting satellites). The main key to this process is the

interaction of the radio wave with the plasma. Before going any further into the discussion, it is necessary to recall some basic concepts of plasma physics.

The plasma frequency describes the response of the charged particle α , of charge q and mass m , to an imposed electric field and is described as follow:

$$f_{p\alpha} = \sqrt{\frac{N_e q^2}{4\pi^2 \epsilon_0 m}} \quad (2.24)$$

with ϵ_0 being the permitivity of free space and N_e the electron density. In the case of a propagating electromagnetic wave in a plasma, the wave is transmitted through the plasma if the frequency of the wave satisfies $f > f_{p\alpha}$. The wave is reflected if $f \leq f_{p\alpha}$.

Probing the ionosphere from the ground is possible by sending electromagnetic waves at different frequencies. For example, if the desired layer to probe has a density N , then the adequate frequency to use for the probe is the corresponding plasma frequency given by equation 2.24. Usually, a radar, referred to as ionosonde, is used to send vertically an electromagnetic wave at a frequency in the range of 1-30 MHz, corresponding to plasma frequency values associated to different local electron density maxima at different heights. The reflected signal is then recorded by the same antenna. Based on this procedure, the travel time is computed and associated with a corresponding height. The values of the heights are presented in a graph, depicting the ionospheric structure, called the ionogram, as illustrated in Figure 2.11. Let

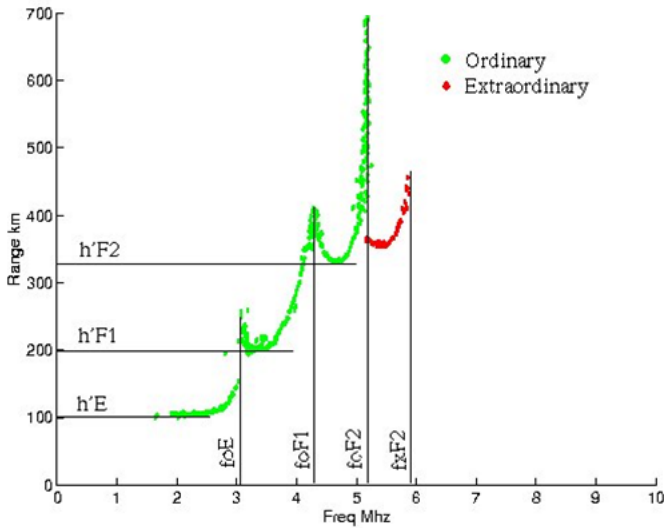


Figure 2.11: Illustration of an ionogram obtained using an ionosonde. The X-axis represents the frequency and the Y-axis represents the virtual height. Critical frequencies of ionospheric layers and corresponding heights are also seen, for both ordinary and extraordinary modes.

us situate two important critical frequencies corresponding to the E and F_2 region: f_0E and f_0F_2 . It is important to note that above the f_0F_2 frequency it is not possible to get reflections, since it is the highest frequency in the ionospheric profile. Therefore, the profile obtained using an ionosonde is called 'bottom-side' profile.

An ionogram gives the density profile in the form of a graphical representation of the variation of the electron density with the so-called virtual height, defined as:

$$h_v = \frac{1}{2}ct = c \int_0^{h_v} \frac{dh}{V_g} = \int_0^{h_v} n_g dh \quad (2.25)$$

where c is the speed of light, V_g and n_g represents the group velocity and the group index of refraction, respectively. The time taken to receive the reflected signal is given by t .

Another powerful technique of ground monitoring the ionosphere is the incoherent scatter; a radar is used to send an electromagnetic wave at a frequency higher than the f_0F_2 in a small region of the ionosphere. Most of the wave will be transmitted through the ionosphere into the outer space. However, a small portion of the wave gets reflected and different observables can be derived from the power spectrum of the reflected wave, such as the drift velocity, the temperature of the electrons and the ions and the density, as well as the neutral wind speed and temperature. However, the cost of this technique is extremely high and the facilities providing such measurements are limited in number. To cite a few, the first station is Jicamarca (Peru), Arecibo (Puerto Rico), Millstone Hill (Massachusetts, USA), the European project EISCAT (Norway/Finland/Sweden).

The advent of the Global Navigation Satellite Systems has provided the opportunity to probe the ionosphere from very high altitude (20000 km) via trans-ionospheric radio wave at ($f >> f_0F_2$). More specifically, using the Global Positioning System (GPS) satellites, transmitting at frequencies $f \approx 1.5$ GHz, it is possible to make trans-ionospheric observations and deduce different observables. Among others, the Total Electron Content (TEC) is defined as the total number of electron integrated along a propagation path and is generally given in TEC units (TECU), with $1TECU = 10^{16}e^-/m^2$.

Also, the power and the phase of the GPS signal can be recorded and, given a proper characterization of these components, interesting features of the ionospheric plasma can be deduced, which is the basic idea of the present thesis.

2.7.1 Sporadic E-layers

Sporadic E-Layers, also referred to as Es-layers, are short time scale ionospheric plasma enhancement due to shear flows in the E region. At these altitudes the ions are dominated by collisions. The ions are then subject to the zonal neutral winds, which accumulate the available ions at the node between the eastward wind above and the westward wind below. The ions that are trapped in between the two shearing layers are metallic ions, such as Fe^+ , with a significant life time against recombination. Moreover, there is some evidence that these layers can be ionized by meteors. The density of a sporadic E-layer can be much greater than the density of a normal E layer. Hence, it possesses a higher plasma frequency (the characteristic frequency at which waves with lower frequency will get reflected). When it is the case, the E-layer will blanket the upper layers. However, there are cases where the upper layers can be seen through the E-layers, and this would be an indication of the patch aspect of the sporadic E-layer.

2.7.2 Spread-F

Spread-F is the term used to describe ionospheric irregularities, observed in ionogram traces, that present a spreading aspect in height at high latitude. These irregularities are mapped along the magnetic field lines, they are also known as Field-Aligned Irregularities (FAI). They can present a patchy aspect with a width of hundreds of kilometers along the magnetic field lines and down to several meters perpendicularly.

In the polar region, the signature of spread-F is a frequency spreading and broadening of the ionogram trace around the critical frequency. Some mechanisms have been proposed to explain the generation of spread-F in the mid and high latitudes. Among them, Haldoupis [2003], after observations of simultaneous Es-layers and spread-F occurrences, suggested that the unstable E layers play a role in the generation of spread-F via upward mapping of the polarization electric field in the E region, formed by the neutral wind that creates a differential current between the electrons and the ions due to the discrepancy in the neutral-ion and neutral-electron collision cross section in the E layer [Haldoupis et al., 2003].

Chapter 3

Global Positioning System

Prior to 1970s, the U.S. Navy and the Air Force had been intensively studying the possibility to improve navigation from space. These studies have led to the design of the Global Positioning System (GPS). Nowadays, the system is composed of about 30 satellites, orbiting at an altitude of 20200 km in six orbital planes of approximately 55° inclination (relative to the equator). The satellites move in nearly circular medium Earth orbits (MEOs) with a revolution period of about 12 hours. With this orbital configuration, the system provides a global coverage with four to eight simultaneously observable satellites above 15° elevation at any time of the day. GPS satellites are equipped with on-board atomic clocks to allow the user to accurately measure the speed, time and position.

3.1 Overview

3.1.1 GPS signal characteristics

The main carrier frequencies¹ transmitted by the GPS are the L1 (at 1.5 GHz) and L2 (at 1.2 GHz) signals. The GPS carriers are modulated using a sequence of code called the Coarse/Acquisition (C/A) pseudo random noise code (PRN), enabling precise ranging and simultaneous acquisition of the GPS signal from different satellites at the same frequency. This code has a length of 1.023 chips a transmission rate of $1.023M\text{chips/sec}$. All satellites are identifiable by their own PRN codes that are uncorrelated with each other. This permits the simultaneous acquisition of the GPS signal from different satellites with a minimum interference [Simon et al., 1994]. The second modulation applied to the carrier signal is the precision P-code, which presents a transmission rate of 10.23 Mbits/sec and a length of 6.1871×10^{12} chips, which makes it more precise than the C/A PRN code. The C/A code is only modulated on the L1 signal, while the P-code is modulated on both carriers, L1 and L2. These two codes are also referred to as the ranging codes, for reasons that will be given in the following text.

¹Other frequencies are used in the transmission of the GPS signal such as the L5 (at 1.176 GHz). However, in the context of this thesis, we are only interested in the L1 and L2 signals.

3.1.2 Positioning techniques

PRN codes are used to measure the range (distance between the satellite and the receiver) via the estimation of the travel time of the GPS signal from the satellite to the receiver. This distance can be computed as follows:

$$P_i = c(t_r - t_s) \quad (3.1)$$

where t_r is the reading of the receiver clock at signal reception time and t_s the reading of the satellite clock at emission time, and c is the speed of light.

The phase measurement is performed using the carrier signal. The phase is considered as the phase difference of the incoming signal and a replica generated by the receiver. However, this estimation is ambiguous, since only a fraction of the phase can be initially measured. One has to estimate an unknown number of cycles, called ambiguity, to compute the distance between the receiver and the satellite. This is performed by multiplying the wavelength by the phase difference:

$$\phi = \lambda(\phi(t_r) - \phi(t_s) + N_r^s) \quad (3.2)$$

where λ is the wavelength of the carrier, $\phi(t_r)$ is the phase of the replica at t_r ; $\phi(t_s)$ is the phase of the transmitted signal at the satellite and N_r^s is the ambiguity.

The convention is to consider the precision of GPS observables as being the inversely proportional to its wavelength. The general consensus is to assume that the precision is the hundredth of the wavelength, see Table 3.1. The

| | C/A-code | P-code | L_1/L_2 phase |
|------------|----------|--------|-----------------|
| Wavelength | 300 m | 30 m | 0.19-0.24 m |
| Precision | 3 m | 0.3 m | 2-2.5 mm |

Table 3.1: GPS observables and the corresponding wavelengths and precisions.

GPS system is operational in three main positioning modes:

1. **Absolute positioning:** This is based on stand-alone measurements with a minimum of four satellites. Phase and code-based observables could be used in this technique.
2. **Differential positioning:** In this technique, the receiver makes the absolute stand-alone measurement. In addition, a correction is brought via comparison with a receiver or a network of receivers or reference station(s). This is called differential correction. This technique is more accurate than the absolute positioning technique.
3. **Relative positioning:** This is the most precise positioning technique. It uses another receiver, for which the position is known accurately, as a reference. The measurements (code and/or phase measurements) obtained by the first receiver are compared with those obtained by the

reference. Thus, this technique consists in computing the vector linking the two stations, which is also called the baseline.

In practice, four satellite observations are needed; three by which the position (latitude, longitude and height) is determined via trilateration. The rest of the observables are used to find the offset receiver clock with respect to the GPS time. As seen before, the ranging codes and the carrier phase can be used in order to estimate the distance from the satellite to the receiver. In the following, we give the models, including the sources of errors.

The pseudo-range estimated from the code signals and the phase measurement obtained from L1 and L2 signals can be expressed respectively as follows:

$$P_i = \rho + c(dt^s - dt_r) + \Delta\rho + I_i + T + M_i + c(D_i^s + D_{r,i}) + e_i \quad (3.3)$$

$$\phi_i = \rho + \Delta\rho - I_i + T + m_i + c(dt^s - dt_r) + c(d_i^s + d_{r,i}) + PCV_i^s + PCV_{r,i} + \lambda_i N_i + \epsilon_i \quad (3.4)$$

with:

P_i the code measurement, in meters, on frequency f_i ;

ϕ_i the phase measurement, in meters, on frequency f_i

f_i the GPS frequency, with $f_1 = 1575.42$ MHz and $f_2 = 1227.60$ MHz;

ρ the geometric distance between the satellite and the antenna;

$\Delta\rho$ the error on rho due to the orbit error;
 I_i the ionospheric delay on frequency f_i ;
 T the tropospheric delay;
 M_i the code multipath error on frequency f_i ;
 m_i the phase multipath error on frequency f_i ;
 c the speed of light in vacuum;
 Δt^s and Δt_r the clock errors related to satellite s and receiver r respectively;
 D_i^s and $D_{r,i}$ the code hardware delays on the ith frequency, respectively for the satellite s and the receiver r;
 d_i^s and $d_{r,i}$ the phase hardware delays on the ith frequency, respectively for the satellite s and the receiver r;
 PCV_i^s and $PCV_{r,i}$ the phase center variations and offsets on the ith frequency, for the satellite s and the receiver r respectively;
 λ_i the wavelength related to f_i ;
 N_i the initial ambiguity on frequency f_i ;
 e_i the code measurement noise on f_i ;
 ϵ_i the carrier phase measurement noise on f_i ;

The main errors in range measurements are described as follows:

1. **Orbit error.** This error is the difference between the real distance satellite-receiver and the computed one. The term $\Delta\rho$ represents the projection of this error on the satellite-to-receiver path.

2. **Ionospheric delay.** As seen in the previous chapter, the ionospheric medium is a dispersive medium due to its plasma characteristics. The signal experiences group delay and phase advance, inducing an error in the range estimation.

3. **Tropospheric delay.** This delay is due to the refractive nature of the troposphere. This latter extends from the surface of the Earth to the tropopause, located between the altitude of 10 to 15 km. The delay induced by the troposphere is defined as:

$$T = \int n ds - \int_{sat}^{rec} ds = \int (n - 1) ds \quad (3.5)$$

where n is the refractive index ($n > 1$, corresponding to the lengthening of the optical path) and ds the infinitesimal element of the path. The troposphere is nondispersive for frequencies up to 15 GHz, and the contribution to the delay is the same for all available frequencies in the GPS system. The refractive index depends on the temperature, pressure and the relative humidity. The range equivalent of this delay is about 2.4 m for a satellite at the zenith and 25 m for a satellite at an elevation of approximately 5° .

4. **Multipath.** This consists of reflection and diffraction of the GPS signal from the surrounding environment, Figure 3.1. It contributes to the delay of the signal. When the reflecting objects are not close, the

delay is large and it is easier to single out the corresponding component. However, in the case of diffraction from nearby objects, the task of filtering out the unwanted components is more difficult. Indeed, due to the shortness of the delay, which can be of the order of tens of nanoseconds, the correlation function between the received signal and the replica (generated by the receiver) is distorted, inducing an error in the range estimation.

The effect of multipath depends on the type of measurement. The amplitude of the induced error on the range estimation can reach a maximum of 15 m for P-code measurements, 150 m for C/A measurements, and about 5 cm for phase measurements.

5. **Clock errors.** As discussed previously, each satellite of the GPS constellation is equipped with an active atomic clock on board, which is synchronized with the GPS time. However, this synchronization is not optimum all the time due to the drift experienced by the atomic reference. As a result, an error is induced in the range measurements. The clock error, Δt^s , can be fit to a polynomial as follows:

$$\Delta t^s = a_0 + a_1(t^s - t_{0c}) + a_2(t^s - t_{0c})^2 \quad (3.6)$$

with a_0 , a_1 , a_2 being some numerical coefficients, t^s and t_{0c} are the current and the reference time for the clock model, respectively.

This model, however, is not well suited for precise positioning.

6. **Hardware-induced Delay.** Electric circuits in the satellite and receiver induce this delay. The latter can vary from one frequency to another, and depend on whether it is a code or a phase measurement; however, it is assumed to be stationary (stable with time). This characteristic dependence on the frequency can be used to calibrate the receiver in order to compute the total electron content (TEC), whose accuracy is dependent on the code hardware delays. In the case where their absolute value is difficult to estimate, the inter-frequency delays, inter-frequency biases (IFB), can be computed by constructing observable differences. The IFB have a value of about 3 ns (1 m) for satellites and 10 ns (3 m) for receivers [Spits, 2012].

3.2 Derived observables for ionospheric studies

3.2.1 Total electron content

As discussed in Chapter 2, the refractive index in the ionosphere, given by Equation 2.7, depends on the frequency of the incoming wave: the ionosphere is said to be dispersive. For the sake of clarity, let us rewrite both equations

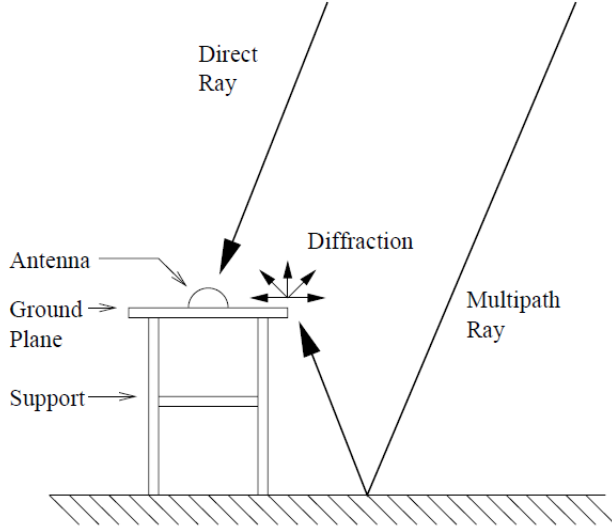


Figure 3.1: Sketch of hypothesized diffraction of multipath ray around the ground plane for a high elevation satellite and an elevated GPS antenna [Mushini, 2013].

2.17 and 2.9 giving the group and phase refractive index, respectively:

$$n_{i,gr} \approx 1 + \frac{40.3N_e}{f_i^2} \quad (3.7)$$

$$n_{i,ph} \approx 1 - \frac{40.3N_e}{f_i^2} \quad (3.8)$$

where $n_{i,gr}$ represents the refractive group index and $n_{i,ph}$ the refractive phase index for the i th frequency (L_1 or L_2), N_e is the electron density and f_i the carrier frequency.

From equations 3.7 and 3.8 we can calculate the frequency-dependent group velocity $v_{i,gr} = \frac{c}{n_{i,gr}}$, depending on the frequency at play of the C/A and P GPS codes. The L_i carrier will have a phase velocity $v_{i,ph} = \frac{c}{n_{i,ph}}$; the

ionosphere will induce a group delay for codes and a phase advance for carrier. Let us write the delay induced by the ionosphere in the form of a length, translating the difference between a real optical path (considering ionospheric refraction) and a free propagation:

$$I = \int n ds - \int ds = \int (n - 1) ds \quad (3.9)$$

where n can represent either the group index n_{gr} or the phase index n_{ph} . It is important to emphasize that we have neglected the bending of the ray². Using 3.7 and 3.8, we can rewrite the delay as³:

$$I_{i,gr} = \int (40.3 \frac{N_e}{f_i^2}) ds \quad (3.10)$$

$$I_{i,ph} = - \int (40.3 \frac{N_e}{f_i^2}) ds \quad (3.11)$$

Rewriting expression 3.11 for two different frequencies leads to:

$$I_{L_1} = \frac{f_2^2}{f_1^2} I_{L_2} \quad (3.12)$$

Using 3.3 and 3.4, one can deduce the total electron content integrated along

²Generally, the bending effect on the ray path is negligible for UHF, since the plasma frequency of the ionosphere is much smaller, of the order of 12 MHz

³The influence of terms of order higher than f_i^{-2} can be neglected for frequencies larger than 1 GHz [Seeber, 2003]. However, we have to stress that higher order terms have to be taken into account for precise geodetic measurements.

the ray path, using the P code and carrier phase, respectively as:

$$TEC_P = 9.52(P_2 - P_1) \quad (3.13)$$

$$TEC_\Phi = 9.52(\Phi_1 - \Phi_2) \quad (3.14)$$

The two quantities differ in nature: TEC_P is computed using the P-code and, therefore, presents a higher error compared to the phase-derived total electron content, TEC_Φ ; this latter is more precise but, at the same time, presents an ambiguity.

In order to enhance the precision, the above two observables can be combined as follows:

$$TEC_{lev} = TEC_\Phi + |TEC_P - TEC_\Phi| \quad (3.15)$$

This operation is referred to as phase leveling: the phase-derived TEC is brought to the level of the code-derived TEC, Figure 3.2.

3.2.2 Vertical projection

The projection of the measured TEC (also termed the slant TEC) to the vertical is usually made assuming a homogeneous ionosphere with no horizontal gradient (which is a rather simplistic assumption). The ionosphere is modeled as a spherical shell with an infinitesimal thickness, containing all the free electrons. The intersection of the ray path with the shell, at a certain assumed height, is called the ionospheric pierce point (IPP), as illustrated in

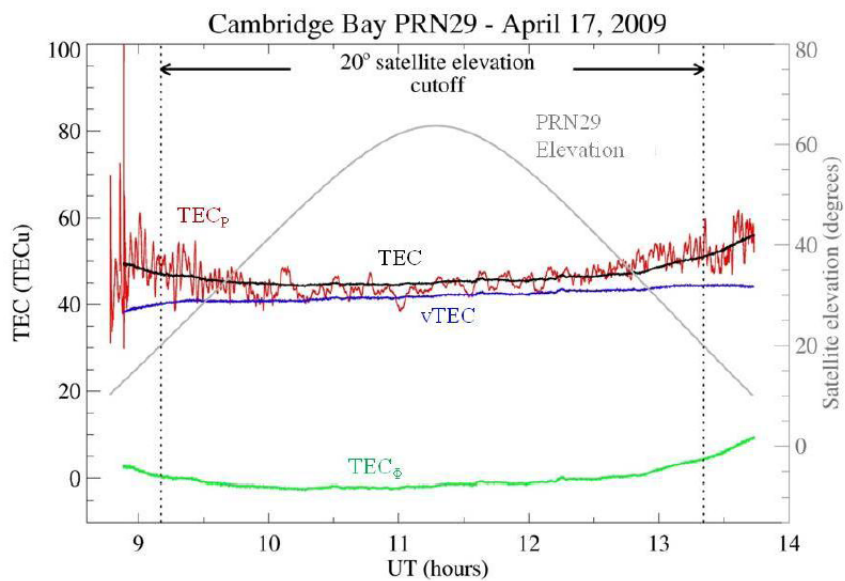


Figure 3.2: Color coded examples of phase and code derived TEC, phase leveled TEC, vertical TEC, and satellite elevation. A satellite elevation cutoff of 20° is indicated by vertical dotted lines [Watson, 2011].

Figure 3.3. The vertical TEC is obtained from the slant TEC via a mapping function:

$$M(e) = \frac{1}{\cos[\arcsin(\cos(e)\frac{R_e}{(R_e+h)})]} \quad (3.16)$$

where e is the elevation angle, R_e the radius of the earth and H the shell height.

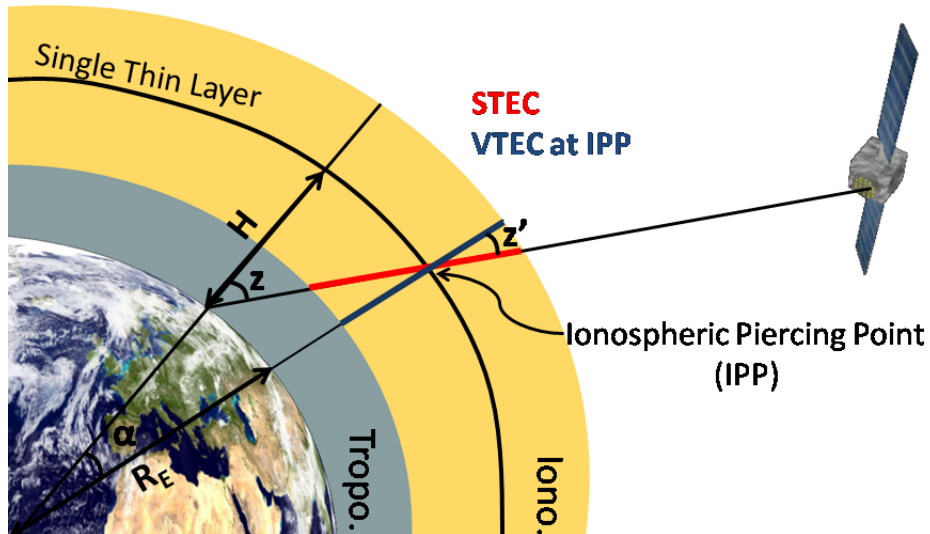


Figure 3.3: Diagram representing the thin shell assumption and also the ionospheric pierce point (IPP), slant-TEC (STEC), vertical-TEC (VTEC) are shown. Courtesy: Royal Observatory of Belgium.

3.3 Canadian High Arctic Ionospheric Network (CHAIN)

CHAIN comprises a cluster of ground-based instruments, used to monitor the ionosphere. It is situated in the Canadian arctic, distributed in different sites, as illustrated in Figure 3.4. The following is a description of these instruments.

3.3.1 GPS receivers

These are GPS Ionospheric Scintillation and TEC Monitors (GISTMs) model GSV4000B [Van Dierendonck and Arbesser-Rastburg, 2004]. Each one consists of a NovAtel OEM4 dual frequency receiver configured to record the phase and amplitude components of the GPS L1 signal. Also, the instrument can provide the TEC derived from the L1 and L2 GPS signals, by the different methods described in the previous section. This receiver enables one to track and record GPS L1 and L2 signals and TEC measurements from up to ten GPS satellites in view. The GPS signal components, phase and amplitude, are recorded at a rate of 50 Hz⁴.

⁴In the present thesis, we only use GPS L_1 signals sampled at 50 Hz. However, CHAIN is equipped with another model of GPS receiver, Septentrio PolaRxS, which can record the GPS signal at a sampling rate of 100 Hz.

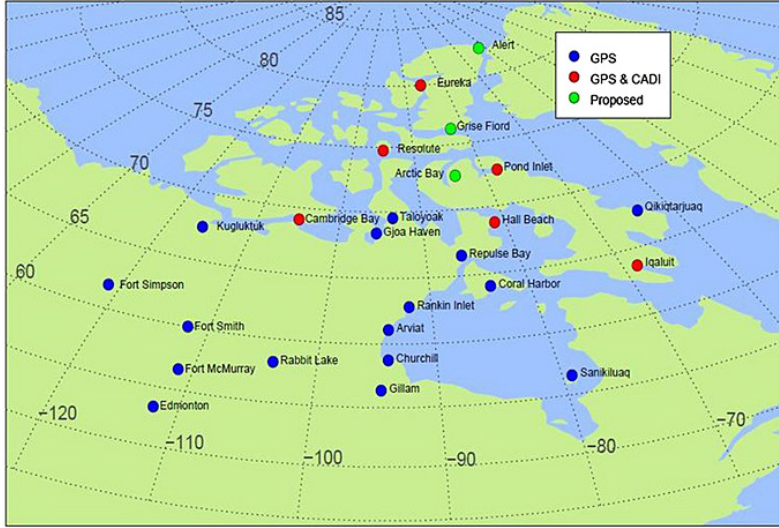


Figure 3.4: The distribution of the GPS receivers and Canadian Advanced Digital Ionosondes (CADIs) in the Canadian High Arctic Ionospheric Network.

3.3.2 Canadian Advanced Digital Ionosonde (CADI)

The Canadian Advanced Digital Ionosonde (CADI) consists of a transmitter antenna and four receiving antennas, arranged in a square geometry in order to perform Doppler interferometry, see Figure 3.6. The frequency range of operation is 0.1-30 MHz and the transmitted pulse power is 600 W.

The main CADI output is interpreted in terms of the ionospheric electron density profile up to the maximum ionospheric plasma frequency, see bottom-side profile⁵ (Figure 3.7). The second output of CADI is the drift velocity of the ionospheric plasma bulk, which is obtained via Doppler interferometry; the two components of the velocity, along with the azimuth angle, are

⁵In section 2.7 we have given the physical principle behind the construction of the ionospheric profile using an ionosonde.

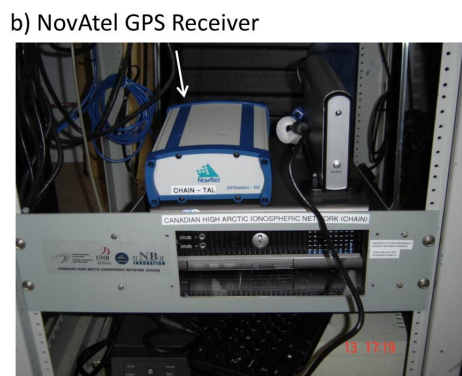


Figure 3.5: CHAIN GPS antenna (a) and NovAtel Receiver (b) located in Cambridge Bay, NU (<http://chain.physics.unb.ca/chain/>).

obtained: the horizontal component and the vertical component, see Figure 3.8.

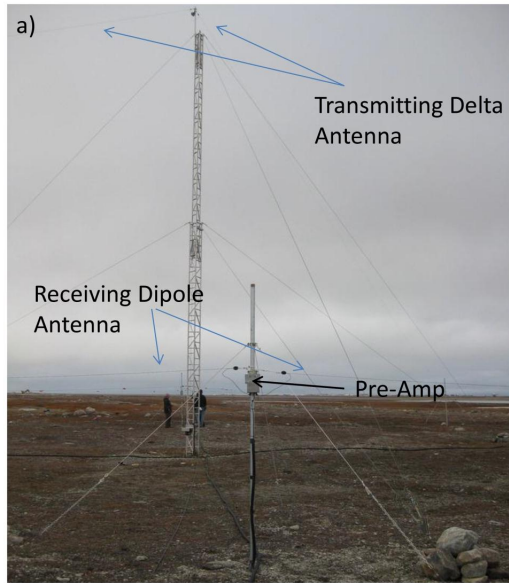


Figure 3.6: CHAIN CADI transmitting and receiving antennas (a) and box containing CADI receivers (b) located in Hall Beach, NU.

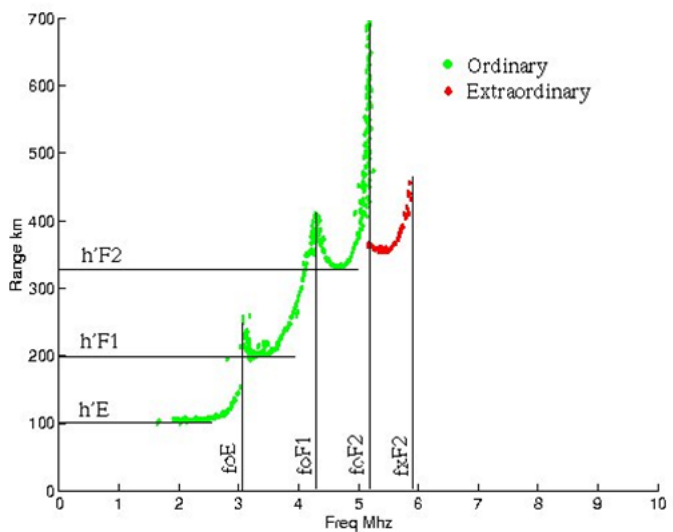


Figure 3.7: Ionogram from the Eureka CADI from signal broadcast at 03:00 UT on 1 November 2011. Received signal power as a function of reflected virtual height and broadcast frequency is indicated for ordinary and extraordinary modes.

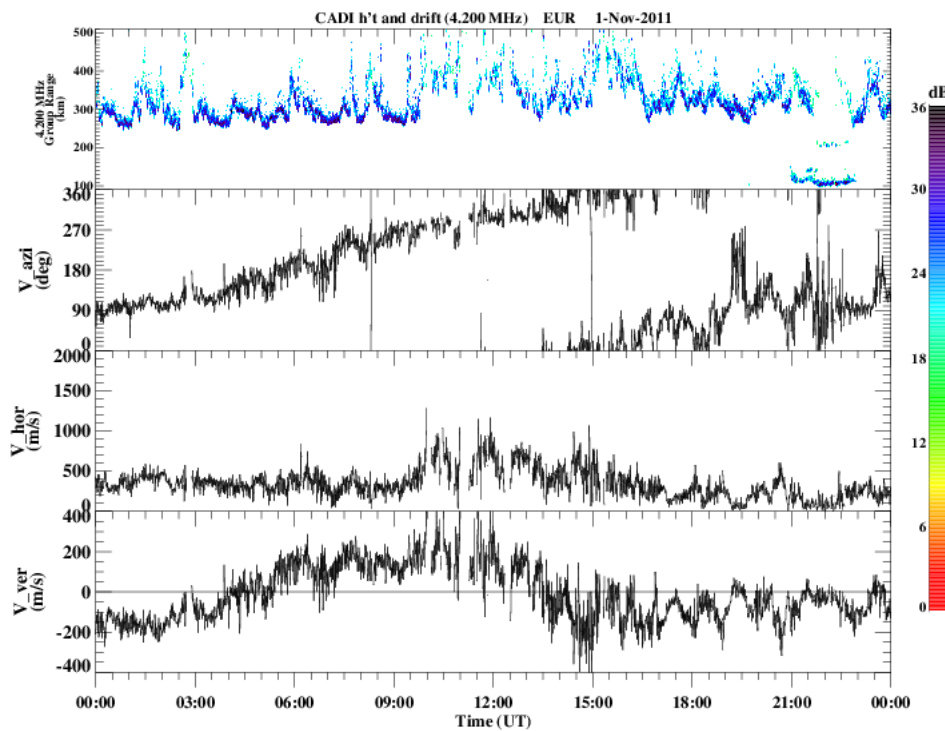


Figure 3.8: Measurements of the Eureka CADI for 24 hours on 1 November 2011. 4.2 MHz group range (top panel), azimuthal ionospheric drift direction (2nd panel), horizontal ionospheric drift speed (3rd panel), and vertical ionospheric drift speed (bottom panel). Drift velocity was calculated from the 4.2 MHz broadcast, while the color bar is the power of the reflected 4.2 MHz signal.

Chapter 4

Overview of ionospheric scintillation

Scintillation is the term given to the phenomenon of fluctuation of the components of an electromagnetic wave propagating in a medium characterized by a dielectric function. The ionospheric plasma is such a medium that is characterized by a highly fluctuating electron density. Therefore, trans-ionospheric radio signals experience perturbations in their phase and the amplitude components.

At high latitude, the irregularities in the plasma density are the product of plasma instabilities and energetic particles' precipitation from the solar wind. In this specific context, we are dealing with high latitude ionospheric scintillations.

4.1 Describing the dielectric function

4.1.1 Multi-scale aspect of the dielectric function

At this point, we want to describe the statistical behavior of the dielectric function, $\Delta\epsilon$, in the ionospheric medium. The time series of the dielectric function can be written under the following form:

$$\Delta\epsilon(t) = (\epsilon(t) - \epsilon_0) + \delta\epsilon(t) \quad (4.1)$$

The first term describes the slow change in the background permittivity. This slow change can be attributed to diurnal and seasonal variations of different ionospheric parameters, such as the temperature and the ionospheric electron density. It can also be the result of a sudden change in the values of the ionospheric parameters, caused by sudden enhancements in solar activity. The last term, $\delta\epsilon(t)$, describes the stochastic component of the dielectric function; compared to the first term, it is characterized by its rapid fluctuations, which are associated with ionospheric scintillation. A fundamental question can be posed here: what are the criteria to decide which are the scales corresponding to diurnal variations and the ones associated to the high-frequency stochastic component of the dielectric function? This is one of the objectives of the present thesis.

4.1.2 Stationarity

The objective of the exercise presented in this section is to separate out the stochastic component of the dielectric function from the slow component. We particularly seek a stationary solution characterized by a stochastic dielectric component that satisfies the following condition:

$$\frac{1}{T} \int_0^T dt \delta\epsilon(t) = 0 \quad (4.2)$$

Theoretically, the integral has to be estimated over an infinite time interval. However, in practice, it is obvious that this is not possible. Usually, the integration is performed over a large set of data in order to incorporate the low-frequency modes associated with the stochastic term $\delta\epsilon$.

A stochastic process can be characterized by its temporal covariance: considering two measurements, made at two different times, t_1 and t_2 , the temporal covariance is defined as

$$B_\epsilon(t_1, t_2) = \overline{\delta\epsilon(t_1)\delta\epsilon(t_2)} \quad (4.3)$$

The condition for stationarity is satisfied if the covariance depends only on the time increment, $\delta t = t_2 - t_1$, and not on the time at which the measurements were made. In this case, the covariance is defined as:

$$\overline{\delta\epsilon(t)\delta\epsilon(t + \tau)} = \frac{1}{T} \int_0^T dt \delta\epsilon(t)\delta\epsilon(t + \tau) = B_\epsilon(\tau) \quad (4.4)$$

A possible alternative approach is to estimate the autocorrelation function $C(\tau)$, defined as

$$C(\tau) = \frac{\overline{\delta\epsilon(t)\delta\epsilon(t+\tau)}}{\overline{\delta\epsilon^2}} \quad (4.5)$$

It is often the case that the ionospheric dielectric function is described by the Fourier transform:

$$B_\epsilon(\tau) = \frac{1}{2\pi} \int_{-\infty}^{\infty} d\omega W_\epsilon(\omega) \exp(i\omega\tau) \quad (4.6)$$

The term $W_\epsilon(\omega)$ is called the power spectrum, that can be thought of as the relative energy distribution in a finite frequency range.

4.1.3 Probability density function

The probability density function describes the probability for a given stochastic variable to take a specific value. For instance, let x be a stochastic variable and $F(x)$ its associated probability density function, then the quantity $F(x)dx = p$ is the probability of having a realisation of an event with a value between x and $x + dx$.

In the ionosphere, if the system is in thermodynamic equilibrium, and follows Boltzmann-Gibbs statistics, then the probability density function is described

by a Gaussian distribution, defined as:

$$F(x) = \frac{1}{\sqrt{2\pi}\sigma} \exp\left(-\frac{x^2}{\sigma^2}\right) \quad (4.7)$$

where σ represents the variance:

$$\sigma^2 = \int_{-\infty}^{+\infty} (x - \mu)^2 F(x) dx \quad (4.8)$$

with μ the first moment of the distribution, given by:

$$\mu = \int_{-\infty}^{+\infty} x F(x) dx \quad (4.9)$$

In general the nth order moment of the distribution is defined as:

$$\mu_n = \int_{-\infty}^{+\infty} (x - \mu)^n F(x) dx \quad (4.10)$$

The ionospheric scintillation is described by the moments of the stochastic part of the dielectric function, $\delta\epsilon$, with a vanishing first moment:

$$\langle \delta\epsilon \rangle = \int_{-\infty}^{+\infty} (\delta\epsilon) F(\delta\epsilon) d(\delta\epsilon) = 0 \quad (4.11)$$

This is equivalent to the stationarity condition, Equation 4.2, where the temporal average vanishes. This duality between moments of the probability density function and temporal averages is described by the ergodic theorem. The theorem states that for long integration periods, the moments and the

temporal averages converge. As a justification, one could argue that if we were to wait long enough, all possible realizations would materialize. As an analytical illustration, let us consider the finite second order moment of the probability density function of $\delta\epsilon$:

$$\int_{-\infty}^{+\infty} (\delta\epsilon - \mu)^2 F(\delta\epsilon) d(\delta\epsilon) \approx \frac{1}{T} \int_0^T dt (\delta\epsilon)^2 \quad (4.12)$$

It is important to emphasize that for short temporal scales, this approximation is not valid, and there could be an important discrepancy between the two quantities.

4.1.4 Spatial covariance

The spatial covariance is a quantity used to describe the distribution of a stochastic variable in space. In our context, the stochastic variable in question could be the stochastic part of the dielectric function $\delta\epsilon$ ¹. If we consider two positions, r_1 and r_2 , the corresponding covariance quantifies the similarity of the values taken by the function of interest at the two locations and is defined as:

$$B_\epsilon(r_1, r_2) = \langle \delta\epsilon(r_1, t) \delta\epsilon(r_2, t) \rangle \quad (4.13)$$

¹It is important to note that in this thesis we are interested in structures of a size in the range of small (0.1-10 km) and intermediate (10-100 km) scales, producing scintillation of the GPS L1 signal at 1.5 GHz. However, we do not have the spatial resolution to completely describe the spatial structure and, therefore, consider the temporal domain, assuming the Taylor hypothesis on the drifting ionospheric plasma layer.

where the brackets represent the ensemble average.

The covariance is used in almost every analytical description of an electro-magnetic wave propagating in a random medium. We note that, in practice, it is usual to replace the ensemble average by a time average:

$$B_\epsilon(r_1, r_2) = \frac{1}{T} \int_0^T dt \delta\epsilon(r_1, t) \delta\epsilon(r_2, t) \quad (4.14)$$

Two aspects of the ionospheric plasma can simplify the spatial covariance, namely, homogeneity and isotropy. In the case of homogeneity, the dielectric function measured at two different points, \vec{r}_1 and \vec{r}_2 , will not depend on the position at which the two points are translated to, but only on the separation vector $\vec{r}_1 - \vec{r}_2$:

$$B_\epsilon(\vec{r}_1 - \vec{r}_2) = < \delta\epsilon(\vec{r}_1, t) \delta\epsilon(\vec{r}_2, t) > \quad (4.15)$$

To a certain extent, this can represent a spatial analogy of the stationarity of $\delta\epsilon$, specifically when the Taylor hypothesis, introduced in the next sections, is assumed.

In the case of an isotropic medium, the covariance function depends on the magnitude of the separation, $|\vec{r}_1 - \vec{r}_2|$, and not on the orientation:

$$B_\epsilon(|\vec{r}_1 - \vec{r}_2|) = < \delta\epsilon(\vec{r}_1, t) \delta\epsilon(\vec{r}_2, t) > \quad (4.16)$$

4.1.5 Power spectra

As discussed before, the complexity of the ionospheric plasma is mainly due to the stochastic part of the dielectric function or, equivalently, the stochastic electron density. Let us turn our attention to the behaviour of the electron density distribution; more specifically, the fluctuations of the electron number density from the background N_0 : $\Delta N(\vec{r}) = N(\vec{r}) - N_0(z)$, and let the fractional fluctuation be the quantity $\xi = \frac{\Delta N(\vec{r})}{N_0(z)}$. In addition, let us make the assumption that ξ is a homogeneous field with zero mean and standard deviation σ_ξ . In this case, the autocorrelation function is defined by ²

$$B_\xi(\vec{r}_1 - \vec{r}_2) = \langle \xi(\vec{r}_1)\xi(\vec{r}_2) \rangle \quad (4.17)$$

The so-called Wiener-Khinchin theorem states that the correlation function and the spectrum form a Fourier pair. Hence, we can recover the spectrum of the electron number density via Fourier transform of the correlation function:

$$\Phi(\vec{k}) = \frac{1}{(2\pi)^3} \int \int \int_{-\infty}^{+\infty} B_\xi(\vec{r}) \exp(-i\vec{k} \cdot \vec{r}) d^3 r \quad (4.18)$$

Note that since the correlation and the spectrum form a Fourier pair, one can also recover back the correlation function by inverse Fourier transform:

$$B_\xi(\vec{r}) = \int \int \int_{-\infty}^{+\infty} \Phi_\xi(\vec{k}) \exp(i\vec{k} \cdot \vec{r}) d^3 k \quad (4.19)$$

²The temporal argument has been omitted for convenience. However, we will recover the time variable when we will assume the Taylor hypothesis.

Since ξ is purely real, symmetry conditions must be met:

$$B_\xi(-\vec{r}) = B_\xi(\vec{r}) \quad (4.20)$$

$$\Phi_\xi(-\vec{k}) = \Phi_\xi(\vec{k}) \quad (4.21)$$

Further, we assume isotropy—the correlation function depends only on $|\vec{r}_1 - \vec{r}_2|$, and the three-dimensional Fourier transform can be simplified:

$$\Phi_\xi(k) = \frac{1}{2\pi^2 k} \int_0^\infty B_\xi(r) r \sin(kr) dr \quad (4.22)$$

$$B_\xi(r) = \frac{4\pi}{r} \int_0^\infty \Phi_\xi(k) k \sin(kr) dk \quad (4.23)$$

Also, one can define one-dimensional and two-dimensional spectra, respectively, as:

$$V_\xi(k_x, y, z) = \frac{1}{2\pi} \int_{-\infty}^\infty B_\xi(\vec{r}) \exp(-ik_x x) dx \quad (4.24)$$

$$F_\xi(k_x, k_y, z) = \frac{1}{2\pi} \int \int_{-\infty}^{+\infty} B_\xi(\vec{r}) \exp(-i(k_x x + k_y y)) dx dy \quad (4.25)$$

In the case of an isotropic medium the three-dimensional spectrum and the one-dimensional spectrum are related as follows:

$$\Phi_\xi(k) = -\frac{1}{2\pi k} \frac{dV_{\xi,0,0}}{dk_\xi} |_{k_x=k} \quad (4.26)$$

We have to emphasise that the relation 4.26 can only be derived in the case of an isotropic medium. In the general case, when the medium is anisotropic, it

is not possible to deduce a relation between the three-dimensional spectrum and the one-dimensional spectrum.

Different experiments, carried out using sounding rockets and sensors on-board satellites, have shown evidence for a power law spectrum of the form $V_\xi \propto k_x^{-m}$ with m close to 2, for spatial scales ranging from tens of meters to tens of kilometres. If we assume an anisotropic irregularity distribution, the three-dimensional spectrum could be then deduced:

$$\Phi_\xi(k) \propto k^{-p} \quad (4.27)$$

with the spectral index p close to 4 for m close to 2. Usually, the power spectrum is compared to the spectrum obtained from the turbulence theory, where the eddies in the flow are assumed to be cascading down from scale to scale with a certain energy transfer rate ϵ . The input of the energy occurs at the largest scale and the dissipation at smallest scales. In between is the inertial range, where the cascade takes place. The three regions are delimited by the inner scale and the outer scale. The inner scale is defined as the largest scale in the dissipation region, and the outer scale, on the other hand, is defined as the smallest scale in the energy injection region. A schematic illustration is given in Figure 4.1.

Shkarofsky, [Shkarofsky, 1968], generalized the powerlaw irregularity spec-

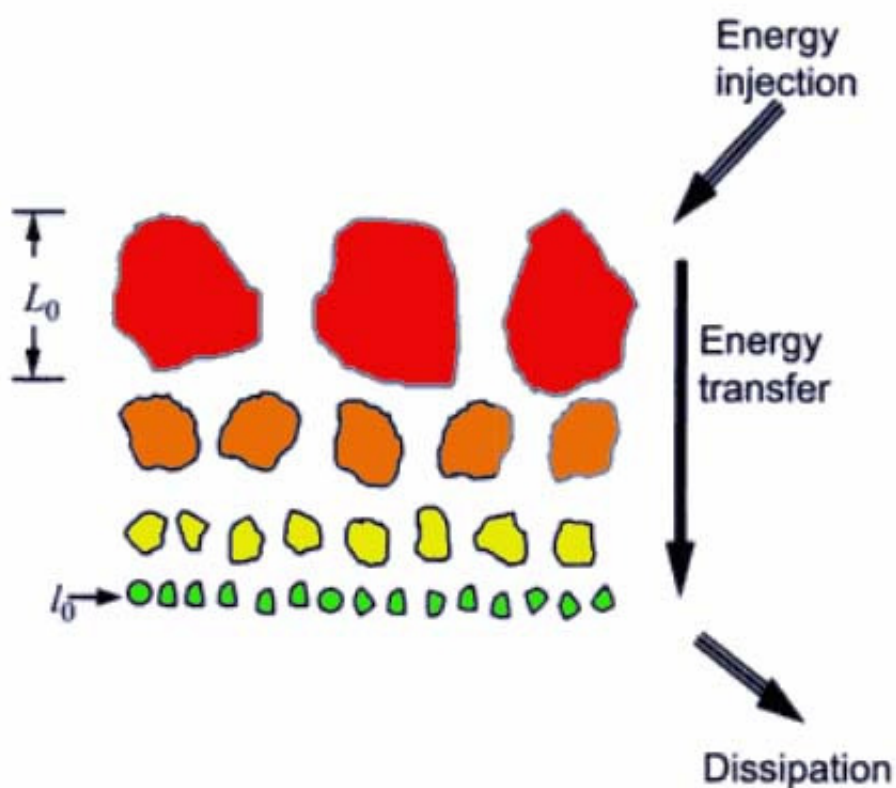


Figure 4.1: A conceptual description of the process of turbulence decay as it proceeds through an energy cascade in which eddies subdivide into progressively smaller eddies until they finally dissipate

trum and the corresponding correlation function:

$$\Phi_\xi(k) = \frac{\sigma_N^2 (k_0 r_0)^{(p-3)/2} r_0^3}{(2\pi^{3/2}) K_{(p-3)/2}(k_0 r_0)} (r_0 \sqrt{k^2 + k_0^2})^{-p/2} \cdot K_{p/2}(r_0 \sqrt{k^2 + k_0^2}) \quad (4.28)$$

$$B_\xi(r) = \frac{\sigma_N^2}{(k_0 r_0)^{(p-3)/2} K_{(p-3)/2}(k_0 r_0)} (k_0 \sqrt{r^2 + r_0^2})^{(p-3)/2} \cdot K_{(p-3)/2}(k_0 \sqrt{r^2 + r_0^2}) \quad (4.29)$$

where r_0 is the inner scale and $l_0 \equiv \frac{2\pi}{k_0}$ is the outer scale. For wavenumber values that lie in the inertial range, defined as the range of k for which $k_0 \ll k \ll \frac{2\pi}{r_0}$, the spectrum defined in 4.28 simplifies to:

$$\Phi_\xi(k) = \frac{\sigma_N^2 \Gamma(p/2) k_0^{p-3}}{\pi^{3/2} \Gamma(\frac{p-3}{2})} \frac{1}{(k^2 - k_0^2)^{p/2}} \propto \frac{1}{k^p} \quad (4.30)$$

which has the same form as in 4.27. In the dissipation range, where $kr_0 \gg 1$, 4.28 reduces to:

$$\Phi_\xi = \frac{\sigma_N^2 (k_0 r_0)^{p-3} r_0^3}{2^{(p-1)/2} \pi \Gamma(\frac{p-3}{2})} \frac{1}{(kr_0)^{(p+1)/2}} \exp(-kr_0) \quad (4.31)$$

where it can be verified that this function converge for $k \rightarrow \infty$. The correlation function presents a maximum value with a vanishing first derivative and a negative second derivative at $\vec{r} = 0$, which is what one would expect, for there the correlation of the field with itself should be maximum [Shkarofsky, 1968].

4.2 Geometric optics

4.2.1 Optical path

Let us consider a ray path in the ionospheric medium, characterized by a homogeneous background of the electron number density. The ray is assumed to be pointing parallel to the z-axis. In this case, one can express the fluctuation in the optical path as follows:

$$\Delta\phi(\vec{\rho}) = \int_{z_0}^{z_l} \Delta n(\vec{\rho}, z) dz \quad (4.32)$$

where $\vec{\rho} = (x, y)$ is the transverse coordinate and the integral is carried out from some initial point, z_0 , to a final point, z_l . The index of refraction is represented by n . The standard deviation of the optical path can be expressed as follows:

$$\Delta\phi(\vec{\rho}) = \frac{-e^2}{2m\epsilon_0\omega^2} \Delta N_T(\vec{\rho}) = \frac{-\lambda^2}{2\pi} r_e \Delta N_T(\vec{\rho}) \quad (4.33)$$

with e the electronic charge and m the mass of the electron, ϵ_0 is the free space permittivity, $\omega = 2\pi f$ is the radio frequency, and r_e represents the classical electron radius. The deviation in the electron content, ΔN_T , is defined as:

$$\Delta N_T(\vec{\rho}) = \int \Delta N(\vec{\rho}, z) dz \quad (4.34)$$

The correlation between two optical paths separated by a distance $\vec{\rho}$ is given

by:

$$B_{\Delta\phi}(\vec{\rho}) = \langle \Delta\phi(\vec{\rho}') \Delta\phi(\vec{\rho} + \vec{\rho}') \rangle = C^2 B_{\Delta N_T}(\vec{\rho}) \quad (4.35)$$

where $C = 2\pi\lambda^2 r_e$. Using Equation 4.34, one can rewrite the correlation of the optical path as follows:

$$B_{\Delta N_T}(\vec{\rho}) = z \int_{-\infty}^{+\infty} B_{\Delta N}(\vec{\rho}, z) dz = 2\pi z \int \int_{-\infty}^{+\infty} \Phi_{\Delta N}(\vec{k}_\perp, 0) e^{ik_\perp \cdot \vec{\rho}} d^2 k_\perp \quad (4.36)$$

with $\vec{k}_\perp = (k_x, k_y)$. By inserting 4.36 into 4.35, one can directly relate the correlation of the optical path to the correlation of the ionospheric irregularities.

The wave propagation in a random media is described by the integrated correlation function:

$$A_{\Delta N}(\vec{\rho}) = \frac{\sigma_{\Delta N}^2 (2/\pi)^{1/2}}{k_0 (k_0 r_0)^{(p-3)/2} K_{(p-3)/2}} (k_0 \sqrt{\rho^2 + r_0^2})^{(p-2)/2} K_{(p-2)/2} (k_0 \sqrt{\rho^2 + r_0^2}) \quad (4.37)$$

The corresponding one-dimensional spectrum is given by:

$$W_{\Delta N}(k_x) = \frac{\sigma_{\Delta N}^2 (k_0 r_0)^{(p-3)/2} r_0^2}{K_{(p-3)/2} (k_0 r_0)} (r_0 \sqrt{k_0^2 + k_x^2})^{-(p-1)/2} \cdot K_{(p-1)/2} (r_0 \sqrt{k_0^2 + k_x^2}) \quad (4.38)$$

Similarly to the stationarity of the dielectric function discussed earlier, the electron number density can possess a homogeneous aspect locally but exhibit a trend at long scales. Therefore, it is more convenient to deal with the

structure function, defined as follows:

$$D_{\Delta N}(\vec{r}) = < [\Delta N(\vec{r} + \vec{r}') - \Delta N(\vec{r}')]^2 >. \quad (4.39)$$

For the optical path, the structure function is defined as the mean square value of the optical path difference between two points separated by a distance $\vec{\rho}$ on a constant plane denoted z:

$$D_{\Delta\phi}(\vec{\rho}) = C^2 D_{\Delta N_T}(\vec{\rho}) = C^2 z \int_{-\infty}^{\infty} [D_{\Delta N}(\vec{\rho}, z) - D_{\Delta N}(0, z)] dz. \quad (4.40)$$

One can notice the direct proportionality between the optical path structure function and the electron content structure function.

4.2.2 Taylor hypothesis: frozen fields

The Taylor hypothesis (also, referred to as the frozen field approximation), applied to the ionospheric plasma, assumes that the ionospheric medium is frozen during the measurement interval. Additionally, the velocity component of the eddies, $\vec{v}(\vec{r}, t)$, is considered to be constant. As a result, the assumption implies that the whole bulk is transported horizontally at a constant velocity without being deformed. In our context, the ionospheric plasma bulk motion is equivalent to moving the ray path parallel to itself through a stationary ionosphere. The phase covariance measured at t and $t + \tau$ is identical to the spatial correlation between parallel rays separated by

a vector:

$$\vec{\rho} = \vec{v}\tau \quad (4.41)$$

The ionospheric plasma dynamic is characterized by spatial and temporal variations. Hence, in general, the fields are written as a function of time and space. More specifically, the electron number density is described by a space time correlation function:

$$B_\xi(\vec{r}, t) = \langle \xi(\vec{r} + \vec{r}', t + t') \xi(\vec{r}, t) \rangle \quad (4.42)$$

The four-dimensional Fourier transform is given by:

$$S_\xi(\vec{k}, \omega) = \frac{1}{((2\pi)^{-4})} \int \int \int \int B_\xi(\vec{r}, t) e^{-i(\vec{k} \cdot \vec{r} + \omega t)} d^3 r dt \quad (4.43)$$

In practice, when a satellite signal emits a radio signal through the ionospheric layer, the received signal exhibits a Doppler shift due to the ionospheric convection and satellite motion, and will also exhibit a Doppler broadening due to the temporal variation of the irregularities. Frozen fields are generally described by the following space-time spectrum:

$$S_\xi(\vec{k}, \omega) = \Phi_\xi(\vec{k}) \delta(\omega + \vec{k} \cdot \vec{v}_0) \quad (4.44)$$

In the case where the frozen field is assumed isotropic then the spatial spectrum can be related to the frequency spectrum as:

$$\Phi_\xi(k) = -\left(\frac{v_0^2}{2\pi k}\right) \frac{d}{d\omega} W_\xi|_{kv_0} \quad (4.45)$$

with $W_\xi(\omega)$ representing the frequency spectrum on a time series $X(\vec{r}, t)$ obtained by a fixed observer (for a given \vec{r}).

4.2.3 Case of non-frozen fields

For non-frozen fields, one has to take into account, in addition to the convection of the plasma bulk, the temporal evolution of the irregularities. This task can be analytically difficult to accomplish. However, given some assumptions, the solution can be obtained for a non-frozen field approach. Two spectrum regions have to be taken into account: large irregularities in the inertial range can be assumed stationary, at least for short time scales, where smaller irregularities in the dissipation range present a variation with time. Shkarofsky [Shkarofsky, 1968], taking this approach, decomposed the spectrum as follows:

$$S_\xi(\vec{k}, \omega) = \Phi_\xi(\vec{k}) Y(\vec{k}, \omega) \quad (4.46)$$

with the normalization condition:

$$\int_{-\infty}^{\infty} Y(\vec{k}, \omega) d\omega = 1 \quad (4.47)$$

Considering the one-dimensional Fourier transform $\psi(\vec{k}, t) = \int Y(\vec{k}, \omega) d\omega$, the spectrum 4.46 in addition to the normalization condition implies:

$$\psi(\vec{k}, t = 0) = 1 \quad (4.48)$$

$$B_\xi(\vec{r}, t = 0) = B_\xi(\vec{r}) \quad (4.49)$$

Comparing 4.44 with 4.46 leads to

$$\psi(\vec{k}, \omega) = \delta(\omega + \vec{k} \cdot \vec{v}_0) \quad (4.50)$$

or, by Fourier transforming:

$$\psi(\vec{k}, t) = e^{-i\vec{k} \cdot \vec{v}_0 t} \quad (4.51)$$

in the case of frozen flows. For the case of non-frozen flows, the spectrum will depend on the distribution associated with the velocity fluctuations. For example, if the velocity is assumed to follow a Gaussian distribution, then the dissipation range spectrum, will be given by:

$$\psi(\vec{r}, t) = e^{-i\vec{k} \cdot \vec{v}_0 t - k^2 \sigma_v^2 t^2 / 2} \quad (4.52)$$

The general spectrum, including the inertia range, can be given by:

$$S_\xi(\vec{k}, t) = \Phi_\xi(\vec{k}) e^{-i\vec{k} \cdot \vec{v}_0 t - k^2 \sigma_v^2 t^2 / 2} \quad (4.53)$$

Up to this point, we have described the phase fluctuation of an electromagnetic wave, which is the result of phase-velocity perturbations induced by the electron density irregularities. This could be a good approximation for scales much greater than the Fresnel scale, for which smaller scales induce diffraction. However, in order to take into account contributions from all scales, one has to include the diffraction in the problem, and geometric optics fails at this task. In the next section we will solve Maxwell's equations in order to give an optimum description of the propagation of an electromagnetic wave in the ionosphere.

4.3 Maxwell's equations in a random medium

Our first goal is to establish the equation describing the propagation of the radio wave in the random medium. The starting point is Maxwell's equations, governing the electric displacement and the magnetic induction fields, \vec{D} and \vec{B} respectively, given by

$$\vec{\nabla} \times \vec{E} = -\frac{1}{c} \frac{\partial \vec{B}}{\partial t} \quad (4.54)$$

$$\vec{\nabla} \times \vec{H} = \frac{\epsilon \partial \vec{E}}{\partial t} + \vec{J} \quad (4.55)$$

$$\vec{\nabla} \cdot \epsilon \vec{E} = \rho_e \quad (4.56)$$

$$\vec{\nabla} \cdot \vec{B} = 0 \quad (4.57)$$

where \vec{J} is the current and ρ_e is the net charge density.

By taking the divergence of 4.55 and using 4.56 one can establish the continuity equation

$$\vec{\nabla} \cdot \vec{J} + \frac{\delta \rho_e}{\delta t} = 0 \quad (4.58)$$

This equation describes the balance involving the current and the charge on the antenna. In the transmission region, these two quantities can be ignored and the divergence of the displacement field \vec{D} vanishes:

$$\vec{\nabla} \cdot \vec{D} = 0 \quad (4.59)$$

In the context of the ionospheric studies, one can consider $\vec{B} = \mu_m \vec{H} = \vec{H}$.

On the other hand, the dielectric function $\epsilon(\vec{r}, t)$ is of primary interest, as it describes the dynamic and the statistical characteristics of the plasma and provides all the information we need to describe the propagation of the electromagnetic wave in the ionospheric plasma.

In the following, we establish the wave features of the electromagnetic propagation. First, we apply the curl operator to 4.54 and, using 4.55, we obtain the following:

$$\vec{\nabla} \times \vec{\nabla} \times \vec{E} = -\frac{1}{c^2} \frac{\partial^2(\epsilon \vec{E})}{\partial t^2} - \frac{\partial \vec{J}}{\partial t} \quad (4.60)$$

we can simplify the equations by using the relation:

$$\vec{\nabla} \times \vec{\nabla} \times \vec{E} = -\nabla^2 \vec{E} + \vec{\nabla}(\vec{\nabla} \cdot \vec{E}) \quad (4.61)$$

The dielectric function is time and space dependent and has to be taken into account when taking the derivative in 4.59

$$\vec{\nabla} \cdot \vec{D} = \vec{\nabla} \cdot (\epsilon \vec{E}) = \vec{E} \cdot \vec{\nabla} \epsilon + \epsilon \vec{\nabla} \cdot \vec{E} = 0 \quad (4.62)$$

Consequently

$$\vec{\nabla} \cdot \vec{E} = -\vec{E} \cdot \vec{\nabla}(\log \epsilon) \quad (4.63)$$

Combining these results, we obtain a general equation for the electric field vector:

$$\nabla^2 \vec{E} - \frac{1}{c^2} \frac{\partial^2}{\partial t^2} [(1 + \delta\epsilon) \vec{E}] = \frac{4\pi}{c} \frac{\partial \vec{J}}{\partial t} - \vec{\nabla} \vec{E} \cdot \vec{\nabla}[\log(1 + \delta\epsilon)] \quad (4.64)$$

The last term in 4.64 describes the polarization changes induced by the scattering in the random medium. In the context of this thesis, these effects are not relevant, and the last term will be dropped.

Both the current density on the GPS antenna and the dielectric function in the ionospheric layer are functions of space and time. However, the character-

istics are quite different. More specifically, the frequency at which the signal is transmitted (e.g., 1.5 GHz for the GPS L1 signal) is much higher than the frequency characterizing the fluctuations in the dielectric function. One can exploit this difference in order to simplify the wave equation 4.64. The current density, as is the case for GPS, can present a complicated function describing pulses, codes and modulation formats used to carry information. If the dielectric function $\epsilon(\vec{r}, t)$ had no dependence on time, then the electric field and the current density, \vec{E} and \vec{J} would be linear functions in 4.64. Both quantities can then be Fourier analyzed, and their modes related algebraically. It is possible to do so in the case where we take into account the high discrepancy between the value of the electromagnetic wave frequency and the frequency characterizing the dielectric function fluctuations. In this case, the mixing of frequency in the term $\delta\epsilon\vec{E}$ can be neglected. We can then consider a common frequency for the source current and the electric field:

$$\vec{J}(\vec{r}, t) = \vec{J}(\vec{r}) \exp(-i\omega t) \quad (4.65)$$

$$\vec{E}(\vec{r}, t) = \vec{E}(\vec{r}) \exp(-i\omega t) \quad (4.66)$$

Considering the Fourier components of the electric field and the current density, we can rewrite equation 4.64:

$$\nabla^2 \vec{E}(\vec{r}) - \vec{E}(\vec{r}) \frac{1}{c^2} \exp(i\omega t) \frac{\partial^2}{\partial t^2} [1 + \Delta\epsilon(\vec{r}, t)] \exp(-i\omega t) = -\frac{4\pi i\omega}{c} \vec{J}(\vec{r}) \quad (4.67)$$

First, we focus on the temporal variations of the dielectric function and write the second term in 4.67 as follows:

$$\begin{aligned} & \frac{1}{c^2} \exp(i\omega t) \frac{\partial^2}{\partial t^2} [1 + \Delta\epsilon(\vec{r}, t)] \exp(-i\omega t) = \\ & k^2 [1 + \Delta\epsilon(\vec{r}, t)] - \frac{2ik}{c} \frac{\partial}{\partial t} \Delta\epsilon(\vec{r}, t) + \frac{1}{c^2} \frac{\partial^2}{\partial t^2} \Delta\epsilon(\vec{r}) \end{aligned} \quad (4.68)$$

Here, $k = \frac{2\pi}{\lambda}$ is the electromagnetic wavenumber.

Second, we need to estimate each term proportional to the stochastic dielectric function $\Delta\epsilon$.

Let us consider the first and the second terms on the right hand side of equation 4.67 for comparison. The first derivative of $\Delta\epsilon$ with respect to the time can be estimated with the following qualitative argument. In the ionospheric plasma, the variations of the dielectric function with respect to time are basically due to both the drift of the whole plasma bulk and the rearrangement of the turbulent eddies within the ionospheric layer. However, the drift velocity is considerably greater than the turbulent velocities. Therefore, the first derivative of ϵ with respect to time is proportional to the drift velocity of the prevailing wind; we can then write, considering eddies of size l , the

following approximation:

$$\frac{\delta}{\delta t} \Delta\epsilon(\vec{r}, t) \approx \frac{v}{l} \Delta\epsilon \quad (4.69)$$

To this, we must add consideration of the Doppler shift due to the moving irregularities:

$$\frac{\partial}{\partial t} \Delta\epsilon(\vec{r}, t) \approx v \Delta\epsilon \left(\frac{1}{l} + \frac{1}{\lambda} \right) \quad (4.70)$$

Comparing 4.70 with the first term on the right hand side of 4.68, we note that

$k^2 \Delta\epsilon \gg \Delta\epsilon \frac{2vk}{c} \left(\frac{1}{l} + \frac{1}{\lambda} \right)$, because the drift speed is negligible relative to the speed of light. A similar argument can be considered for the second derivative of the dielectric function, and the latter can be dropped.

At this point, we can write the final wave equation:

$$\nabla^2 \vec{E} + k^2 [1 + \epsilon_1(\vec{r})] \vec{E} = 0 \quad (4.71)$$

where ϵ_1 is the stochastic component of the dielectric function.

The current density has been dropped since we are interested in the propagation of the wave far from the antenna. This wave equation, describing the wave propagation in a random medium, is the starting point of any full description of the ionospheric scintillation.

In order to solve 4.71, let us consider a vertical incidence and a propagation parallel to the z axis, we can write the electric field \vec{E} by introducing the

complex amplitude u :

$$\vec{E} = \vec{u}(\vec{r}) \exp(-ikz) \quad (4.72)$$

Replacing the electric field by 4.72 in 4.71 leads to the following equation:

$$-2jk \frac{\partial u}{\partial z} + \nabla^2 u = -k^2 \epsilon_1(\vec{r}) u \quad (4.73)$$

The wavelength of a radio wave is much smaller than the characteristic wavelength of the dielectric function (forward scattering assumption), $\epsilon(\vec{r}, t)$, in the ionosphere; therefore we have $|2k \frac{\delta}{\delta z}| \gg |\frac{\delta^2 u}{\delta z^2}|$ and the parabolic approximation is applicable:

$$-2jk \frac{\partial u}{\partial z} + \nabla_{\perp}^2 u = -k^2 \epsilon_1(\vec{r}) u \quad (4.74)$$

where ∇_{\perp}^2 is the transverse Laplacian.

We can note that two contributions are described by this equation: scattering diffraction of the wave by the electron density irregularities and the random phase fluctuations introduced by the dielectric function in the ionospheric layer.

In the case where the Fresnel scale is much smaller than the outer scale, l_0 , diffraction can be ignored and equation 4.74 becomes:

$$-2jk \frac{\partial u}{\partial z} = -k^2 \epsilon_1(\vec{r}) u \quad (4.75)$$

the solution is then given by:

$$u(\vec{r}, t) = u_0 \exp(-i\phi(\vec{r}, t)) \quad (4.76)$$

where the phase can be expressed as:

$$\phi(\vec{r}, t) = \frac{k}{2} \int_0^z \epsilon(\rho, z', t) dz' = -\lambda r_e \Delta N_T(\rho, z, t) \quad (4.77)$$

Here, r_e and ΔN_T represent the electron radius and the fluctuations of the electron content, respectively. The vector quantity $\vec{\rho}$ represents the transverse spatial components, $\vec{\rho} = x\hat{e}_x + y\hat{e}_y$. This approximation is the basis of the phase screen theory [Booker et al., 1950; Rino, 1976].

Upon emergence from the screen, the wave undergoes a free propagation and experiences phase mixing due to the distortion of the wavefront. The phase equation to solve is then given by Equation 4.74 without the dielectric term:

$$-2jk \frac{\partial u}{\partial z} + \nabla_{\perp}^2 u = 0 \quad (4.78)$$

In order to account for the scattering, diffraction and phase changes induced by the screen, a procedure that consists of solving successively 4.78 and 4.77 can be applied by solving for each step and injecting the solution as the initial condition for the next one.

Scintillation is a stochastic phenomenon, and therefore one needs to characterize the statistical properties of the observed signal in order to have a proper

understanding in the physical mechanism at play. In other words, one needs to characterize the statistical behavior of the complex amplitude $u(\vec{r}, t)$. For example, the computation of the higher order moments are required, and an assumption about the distribution that fits the probability density function needs to be identified. Historically, this latter is assumed to be Gaussian with a zero mean. In this case, the first moment of the distribution is given by [Yeh and Liu, 1982]:

$$\langle u \rangle = \exp(-\phi_0^2/2) \quad (4.79)$$

where ϕ_0 is the variance of the phase introduced by the medium. The average intensity on the ground can be given as:

$$\langle u(\vec{r}, z)u^*(\vec{r}, z) \rangle = u_0^2 \quad (4.80)$$

which is consistent with the forward scattering assumption and the conservation of the energy of the wave.

However, there is no conclusive evidence about the Gaussianity of the field, and a universal function describing the scintillation is still under investigation.

4.4 General solutions

Usually, the complex amplitude is written under the following form:

$$u(\vec{\rho}, z) = u_0 \exp[\Xi(\vec{\rho}, z) - iS_1(\vec{\rho}, z)] \quad (4.81)$$

where $\Xi(\vec{\rho}, z)$ is the so-called log-amplitude and $S_1(\vec{\rho}, z)$ the phase departure of the wave.

In the case where the fluctuations on the phase are not important (shallow screen) such that $\phi_0 \ll 1$, the wave equation can be solved analytically:

$$\Xi(\vec{\rho}, z) = \frac{k}{2\pi z} \int_{-\infty}^{\infty} \int_{-\infty}^{\infty} \phi(\vec{\rho}') \cos\left[\frac{k|\vec{\rho} - \vec{\rho}'|^2}{2z}\right] d^2\rho' \quad (4.82)$$

$$S_1(\vec{\rho}, z) = \frac{k}{2\pi z} \int_{-\infty}^{\infty} \int_{-\infty}^{\infty} \phi(\vec{\rho}') \sin\left[\frac{k|\vec{\rho} - \vec{\rho}'|^2}{2z}\right] d^2\rho' \quad (4.83)$$

The different moments can be derived, such as the mean:

$$\langle \Xi \rangle = \langle S_1 \rangle = 0 \quad (4.84)$$

Also, from the correlation functions

$$B_{\Xi}(\vec{\rho}) = \int_{-\infty}^{\infty} \int_{-\infty}^{\infty} \Phi_{\phi}(\vec{k}_{\perp}) \sin^2\left(\frac{\vec{k}_{\perp}^2 z}{2k}\right) \cos(\vec{k}_{\perp} \cdot \vec{\rho}) d^2 k_{\perp} \quad (4.85)$$

$$B_{S_1}(\vec{\rho}) = \int_{-\infty}^{\infty} \int_{-\infty}^{\infty} \Phi_{\phi}(\vec{k}_{\perp}) \cos^2\left(\frac{\vec{k}_{\perp}^2 z}{2k}\right) \cos(\vec{k}_{\perp} \cdot \vec{\rho}) d^2 k_{\perp} \quad (4.86)$$

where the $\Phi_\phi(\vec{k}_\perp)$ is the power spectrum of the phase $\phi(\vec{\rho})$, given by

$$\phi(\vec{\rho} = \lambda^2 r_e^2 \Phi_{\Delta N_T}(\vec{k}_\perp, 0)) \quad (4.87)$$

we obtain the mean-square fluctuations for Ξ and S_1 :

$$\langle \Xi^2 \rangle = 2\pi L \lambda^2 r_e^2 \int_{-\infty}^{\infty} \int_{-\infty}^{\infty} \Phi_{\Delta N_T}(\vec{k}_\perp, 0) \sin^2\left(\frac{\vec{k}_\perp^2 z}{2k}\right) d^2 k_\perp \quad (4.88)$$

$$\langle S_1^2 \rangle = 2\pi L \lambda^2 r_e^2 \int_{-\infty}^{\infty} \int_{-\infty}^{\infty} \Phi_{\Delta N_T}(\vec{k}_\perp, 0) \cos^2\left(\frac{\vec{k}_\perp^2 z}{2k}\right) d^2 k_\perp \quad (4.89)$$

(4.90)

Although we have considered an incident plane wave, the results could be applied in the case of spherical waves. However, these results are only valid when the fluctuations in the phase component, induced by the irregularities, are minor. Usually, in the case of high latitude scintillation, this condition is rarely met, and one has to turn to other techniques in order to solve the wave equation.

4.5 Rytov's approximation

4.5.1 The Rytov transformation

In equation 4.71 the stochastic term $\epsilon_1(\vec{r}, t)$ multiplies the electric field that we try to solve for. In an ideal situation, one would like to separate these two terms and have a source term that depends only on the dielectric function.

The Rytov transformation achieves this precise goal and is described in what follows.

The starting point of Rytov's idea was to write the electric field as the product of the unperturbed field with a phasor term characterized by a complex phase $\Psi(\vec{r})$ (also termed as the surrogate function):

$$\vec{E} = \vec{E}_0 \exp(\Psi(\vec{r})) \quad (4.91)$$

Considering the following identity:

$$\nabla^2(AB) = A\nabla^2B + 2\nabla A \cdot \nabla B + B\nabla^2A \quad (4.92)$$

and substituting in 4.71, one obtains the equation:

$$E_0 \nabla^2(e^\Psi) + 2\nabla E_0 \cdot \nabla(e^\Psi) + k^2 \epsilon_1 E_0 e^\Psi = -e^\Psi \nabla^2 E_0 - k^2 E_0 e^\Psi \quad (4.93)$$

and keeping in mind that the unperturbed field strength satisfies

$$\nabla^2 E_0 + k^2 E_0 = 0, \quad (4.94)$$

one can write the following equation:

$$\nabla^2(e^\Psi) + 2\nabla(\ln E_0) \cdot \nabla(e^\Psi) + k^2 e^\Psi \epsilon_1 = 0 \quad (4.95)$$

Considering the differential identity

$$\nabla^2(e^\Psi) = \nabla \cdot (e^\Psi \nabla \Psi) = e^\Psi (\nabla \Psi)^2 + e^\Psi \nabla^2 \Psi, \quad (4.96)$$

and substituting in equation 4.95, we obtain:

$$\nabla^2 \Psi + (\nabla \Psi)^2 + 2\nabla(\ln E_0) \cdot \nabla(\Psi) = -k^2 \epsilon_1(\vec{r}, t) \quad (4.97)$$

At this point, it is convenient to write the unperturbed field as the exponential of a dimensionless function similar to the surrogate function:

$$E_0(\vec{r}) = \exp(\Psi_0(\vec{r})) \quad (4.98)$$

The total field can be then written as follows:

$$E(\vec{r}) = \exp(\Psi_0(\vec{r}) + \Psi(\vec{r})) \quad (4.99)$$

When we substitute into 4.97, we obtain:

$$\nabla^2 \Psi + (\nabla \Psi)^2 + 2\nabla \Psi_0 \cdot \nabla \Psi + k^2 \epsilon_1 = 0 \quad (4.100)$$

The unperturbed field E_0 is assumed to have a perpendicular propagation. Therefore, the gradient of the corresponding complex phase is given by:

$$\nabla \Psi_0 = \frac{\partial}{\partial z} \Psi_0 \hat{e}_z = -jk \hat{e}_z \quad (4.101)$$

with this assumption the final form of equation 4.5.1 is given by:

$$-2jk \frac{\delta \Psi}{\delta z} + \Delta_{\perp}^2 \Psi + (\Delta_{\perp} \Psi)^2 = -k^2 \epsilon_1(\vec{r}) \quad (4.102)$$

This equation can be solved by expanding the function $\Psi(\vec{r})$ into powers of the dielectric function ϵ :

$$\Psi(\vec{r}) = \psi_1(\vec{r}) + \psi_2(\vec{r}) + \psi_3(\vec{r}) + \dots \quad (4.103)$$

where each term ψ_n is proportional to the nth power of the dielectric function ϵ_1 . In order to have the equations satisfied by the surrogate function ψ at different order, we substitute 4.103 into 4.5.1 and get the following set of equations:

$$\nabla^2 \psi_0 + (\nabla \psi_0)^2 + k^2 = 0 \quad (4.104)$$

$$\nabla^2 \psi_1 + 2\nabla \psi_0 \cdot \nabla \psi_1 + k^2 \epsilon_1 = 0 \quad (4.105)$$

$$\nabla^2 \psi_2 + 2\nabla \psi_0 \cdot \nabla \psi_2 + (\nabla \psi_1)^2 = 0 \quad (4.106)$$

$$\nabla^2 \psi_3 + 2\nabla \psi_0 \cdot \nabla \psi_3 + 2\nabla \psi_1 \cdot \nabla \psi_2 = 0 \quad (4.107)$$

$$\nabla^2 \psi_4 + 2\nabla \psi_0 \cdot \nabla \psi_4 + 2\nabla \psi_1 \cdot \nabla \psi_3 + (\nabla \psi_2)^2 = 0 \quad (4.108)$$

$$\nabla^2 \psi_n + 2\nabla \psi_0 \cdot \nabla \psi_n + \sum_{p=1}^{n-1} \nabla \psi_p \cdot \nabla \psi_{n-p} = 0 \quad (4.109)$$

One can notice that the unperturbed field E_0 , defined by 4.94 comes into

play via the coupling term $2\nabla\psi_0 \cdot \nabla\psi_n$ in each approximation.

4.5.2 The Basic Rytov Solution

In this solution, we use the first term in 4.103 in equation 4.105, which we rewrite in the following form:

$$\nabla^2\psi_1 + 2\nabla\psi_0 \cdot \nabla\psi_1 = -k^2\epsilon_1 \quad (4.110)$$

In order to solve this equation, let us make the following substitution:

$$\psi_1 = \alpha(\vec{r})\exp[-\psi_0(\vec{r})] \quad (4.111)$$

This can be simplified to

$$\nabla^2\alpha + \alpha[-\nabla^2\psi_0 - (\nabla\psi_0)^2] = -k^2e^{\psi_0}\epsilon_1(\vec{r}, t) \quad (4.112)$$

This equation can be solved using Green's function:

$$\alpha(\vec{R}) = -k^2 \int d^3r G(\vec{R}, r)\epsilon_1(\vec{r}, t)\exp[\psi_0(\vec{r})] \quad (4.113)$$

Combining this with 4.110, we obtain:

$$\psi_1 = -k^2 \int d^3r G(\vec{R}, r)\epsilon_1(\vec{r}, t) \frac{E_0(\vec{r})}{E_0(\vec{R})} \quad (4.114)$$

Taking into account the expression of ψ_1 , the Rytov approximation becomes:

$$E_1(\vec{R}) = E_0(\vec{R}) \exp\left(-k^2 \int d^3r G(\vec{R}, \vec{r}) \epsilon_1(\vec{r}, t) \frac{E_0(\vec{r})}{E_0(\vec{R})}\right) \quad (4.115)$$

In the case of weak scattering, the exponential can be expanded:

$$E_1(\vec{R}) = E_0(\vec{R})(1 + \psi_1 + \dots) \quad (4.116)$$

This is the so-called Born approximation. However, in the context of the ionospheric scintillation, the term in the exponent is usually high, due to the non-linear aspect of the medium, and the Born approximation is not valid.

From 4.115, it is clear that one can associate the phase with the imaginary part of the scattering integral:

$$\phi(\vec{R}) = \left(-k^2 \int d^3r \mathbf{Im} \left(G(\vec{R}, \vec{r}) \epsilon_1(\vec{r}, t) \frac{E_0(\vec{r})}{E_0(\vec{R})} \right) \right) \quad (4.117)$$

The amplitude, on the other hand, can be associated to the real part of the electric field:

$$A(\vec{R}) = |E_0(\vec{R})| \exp \left[\left(-k^2 \int d^3r \mathbf{Re} \left(G(\vec{R}, \vec{r}) \epsilon_1(\vec{r}, t) \frac{E_0(\vec{r})}{E_0(\vec{R})} \right) \right) \right] \quad (4.118)$$

It is culture to deal with the logarithmic amplitude defined as follows

$$\Xi = \log \left(\frac{A}{E_0} \right) = -k^2 \int d^3r \mathbf{Re} \left(G(\vec{R}, \vec{r}) \epsilon_1(\vec{r}, t) \frac{E_0(\vec{r})}{E_0(\vec{R})} \right) \quad (4.119)$$

Let us pose

$$G(\vec{R}, \vec{r}) \frac{E_0(\vec{r})}{E_0(\vec{R})} = A(\vec{R}, \vec{r}) + iB(\vec{R}, \vec{r}) \quad (4.120)$$

At this point, we can write the variances for the logarithm amplitude and the phase, respectively, as follows:

$$\langle \Xi^2 \rangle = k^4 \int d^3 r A(\vec{R}, \vec{r}) \int d^3 r' A(\vec{R}, \vec{r}') \langle \epsilon_1(\vec{r}, t) \epsilon_1(\vec{r}', t) \rangle \quad (4.121)$$

$$\langle \phi^2 \rangle = k^4 \int d^3 r B(\vec{R}, \vec{r}) \int d^3 r' B(\vec{R}, \vec{r}') \langle \epsilon_1(\vec{r}, t) \epsilon_1(\vec{r}', t) \rangle \quad (4.122)$$

In order to estimate the double volume integrations, one has to have a good understanding of the behavior of the dielectric function ϵ_1 . This is the main challenge in the ionospheric scintillation problem, since the ionosphere is a nonlinear medium with a potentially chaotic behavior, making it difficult to define the appropriate function describing the fluctuations of the permittivity at different scales.

Chapter 5

Application of the maximum entropy principle in the determination of the scintillation components

The ionosphere, being a highly dynamic multi-scale system, requires an optimum characterization of its statistical and spectral properties, in order to understand the mechanism at play during ionospheric scintillation. This is possible only if we have robust mathematical tools that enable us to extract information about the system's properties.

In the present chapter, we introduce such mathematical tools, namely, the wavelet transform and the wavelet based entropy. We characterize the statis-

tical properties of the phase and the signal component of the GPS L1 signal during scintillation. Using the entropy maximization principle, we develop a technique to single out critical scales and filter out the non-scintillation component from the raw GPS signal.

5.1 Wavelet transform

5.1.1 Introduction

The most commonly used basis, in the context of Fourier transforms, are the trigonometric functions, for the main fact that they constitute an orthogonal basis of $L(0, 2\pi)$. Therefore, they allow the decomposition of any function into a linear combination of Fourier vectors, defined by the Fourier coefficients $\hat{f}(\omega) = \langle e^{i\omega t} | f(t) \rangle$. The inconvenience induced by the Fourier transform is the delocalization of the information content of $f(t)$ among all the spectral coefficients $\hat{f}(\omega)$. This could prevent the characterization of a given function $f(t)$ from the properties of $\hat{f}(\omega)$, due to the contamination of all the Fourier components.

On the other hand, the wavelet transform, due to its local aspect, allows the reconstruction of a part of a signal without losing information about its properties. For example, singularities in the signal $f(t)$ will correspond to a wavelet coefficient with a drastically increased amplitude in its vicinity. Therefore, it is possible to retrieve information about the smoothness of the function from the characteristics of its wavelet coefficients. Consequently,

the local aspect of the wavelet transform makes it a very robust method for reconstruction, and any error in the wavelet coefficient will affect the signal locally, whereas in the case of the Fourier transform the error would spread out everywhere in the reconstructed signal.

5.1.2 Definition

The wavelet transform allows one to unfold a signal into its conjugate components. As opposed to the Fourier transform, it is localized in space or time, and therefore does not take into account the behavior of the signal at infinity.

The transform uses functions, wavelets ψ , that must satisfy certain conditions. The first one is stationarity, which implies that the wavelet must be integrable and its average should be zero, i.e.

$$\int_{-\infty}^{\infty} \psi(x)dx = 0 \quad (5.1)$$

The second requirement for a function to be used as a wavelet is similarity, or scale invariance. Since the wavelet decomposition is obtained by the translation and dilation of the wavelet and convolution with the signal, all of the analyzing wavelets should have the same number of oscillations. This condition will lead to an optimum compromise in the context of the uncertainty principle. Figure 5.1 gives an illustration of the convolution of the basis wavelet (mother wavelet) with the signal.

In order to parametrize the operation of shifting and scaling, the wavelet is written in the following form:

$$\Psi_{a,b}(t) = \frac{1}{\sqrt{a}} \Psi\left(\frac{(t-b)}{a}\right) \quad (5.2)$$

with “a” being the scaling parameter and “b” representing the shifting parameter. The wavelet is then convolved with the signal to obtain the wavelet transform:

$$\gamma(a, b) = \int_{-\infty}^{+\infty} f(t) \frac{1}{\sqrt{a}} \Psi^*\left(\frac{t-b}{a}\right) dt, \quad (5.3)$$

where $\gamma(a, b)$ represent the wavelet transform coefficient, given a certain scale “a”.

In practice, the signals are recorded at a sampling rate, and present a discrete aspect. Therefore, one has to consider the wavelet transform in a discrete space.

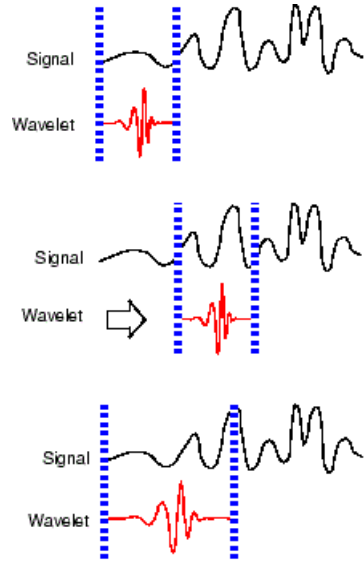


Figure 5.1: An illustration of shifting and scaling of a mother wavelet in order to calculate the wavelet transform [Mushini, 2013].

5.1.3 Wavelet transform of a discrete signal

Let us consider a signal recorded at a certain sampling rate and denote the different components of the signal as $x_0, x_1, x_2, \dots, x_N$, where N is the total number of sample points. Let δt be the spacing between two samples. The wavelet transform is then given by:

$$W(s) = \sum_{n'=0}^{N-1} x_{n'} \Psi^* \left[\frac{(n' - n)\delta t}{s} \right], \quad (5.4)$$

where Ψ^* represents the complex conjugate of Ψ . In order to obtain the wavelet transform of the total signal, N convolutions are required for every

scale. In the case of a high time-resolution signal, this would be computationally expensive. For the sake of efficiency, the convolutions are usually computed in Fourier space using discrete Fourier transforms. This is made possible by the fact the convolution of two sequences that are circularly-extended is the product of the Fourier transforms of these two sequences. Given this property, the wavelet transform of a discrete signal is given by:

$$W(s) = \sum_{k=0}^{N-1} \hat{X}_k \hat{\Psi}^*(s\omega_k) e^{i\omega_k n\delta t} \quad (5.5)$$

where \hat{X}_k represents the Fourier transform of the signal x_n , and $\hat{\Psi}^*$ represents the Fourier transform of the function $\Psi(t/s)$, where s and t represent the scale and the time, respectively. The angular frequency ω_k is given by:

$$\omega_k = \frac{2\pi k}{N\delta t} : k \leq \frac{N}{2} \quad (5.6)$$

$$\omega_k = -\frac{2\pi k}{N\delta t} : k > \frac{N}{2} \quad (5.7)$$

In order to perform the wavelet transform, one has to define a scale range at a certain sampling rate. In the present work, we define the range of scales in terms of fractional powers of two:

$$s_j = s_0 2^{j\delta j} \quad (5.8)$$

$$J = \delta j^{-1} \log_2 \left(\frac{N\delta t}{s_0} \right) \quad (5.9)$$

where s_0 (the smallest resolvable scale) was chosen to be $2 * \delta t$, where δt is 0.02 sec (50 Hz) and δj (the resolution in scale) was chosen to be 0.125.

5.1.4 Basis wavelet

The basis function used to obtain the wavelet coefficients is characterized by its shape in the time-domain. In Figure 5.2, four examples of basis wavelet are shown. Let us emphasize the complex aspect of the Morlet and Paul wavelets (Figure 5.2a and Figure 5.2b), where the dashed line represents the imaginary part and the solid line the real part. On the other hand, the DOG and Mexican hat wavelets are real valued and constitute derivatives of the Gaussian function. Different other basis function can be investigated, e.g., Harr, Daubechies etc.

Defining the criteria for a wavelet in order to have an optimum characterization of a given signal is of primary interest. When it comes to defining the optimum wavelet function that is the most suitable for a given signal analysis, different parameters need to be considered. The wavelet has to reflect certain aspects of the signal under consideration. For example, in the context of the investigation of the oscillatory behaviour of a signal, a complex wavelet is the most suitable, as it would give information about the amplitude and the phase of the signal. However, if one needs to analyse a signal that presents a discontinuous aspect or isolated peaks, the real valued wavelets are the most appropriate. Another aspect of the basis wavelet that has to be taken into account is the width in real space and in the frequency space. According to

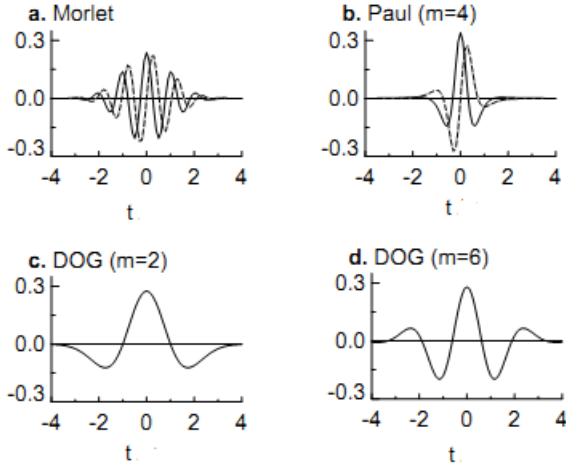


Figure 5.2: Illustration of four different mother wavelets: (a) Morlet, (b) Paul, (c) Mexican hat, and (d) DOG. The parameter m represents the number of vanishing moments and the solid line shows the real part, while dashed line shows the imaginary part of the signal [Mushini, 2013].

the Heisenberg principle, a narrower width in time would correspond to wider width in frequency and vice versa. Therefore, one has to find a compromise between reaching a high resolution in time and having a high resolution in frequency.

5.1.5 Morlet wavelet

This wavelet was proposed by a French geophysicist, Jean Morlet, in collaboration with Pierre Goupillaud and A. Grossmann [Farge, 1992]. The wavelet in question is the product of a sine function with a Gaussian envelope, as illustrated in Figure 5.3.

The advantage put forth by this function is that it is characterized by a

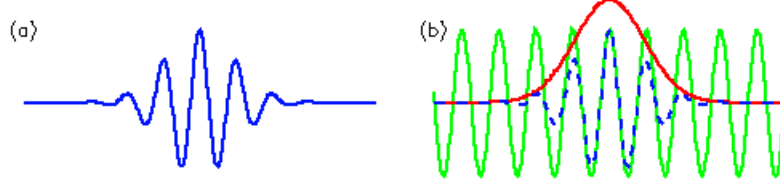


Figure 5.3: Construction of the Morlet wavelet is illustrated. (a) representation of a Morlet wavelet and (b) construction of a Morlet wavelet by convolving a Gaussian curve with a sine wave [Mushini, 2013].

certain frequency and a local aspect (by the fact of being finite in its extent). In addition, due to its small time-bandwidth product, the Morlet wavelet constitutes the best compromise between the time and frequency resolution. The Morlet wavelet is given by the following expression:

$$\Psi_0(t) = \pi^{0.25} e^{i\omega_0 t - \frac{1}{2}t^2} \quad (5.10)$$

with ω_0 being a non-dimensional frequency. The Morlet wavelet is not completely stationary and hence the admissibility condition is not satisfied unless small correction terms are added. However, in practice we utilize the value of $\omega_0 = 6$, as for this value of the dimensionless frequency the correction terms are negligible.

The Fourier wavelength and the wavelet scale are related by [Farge, 1992]

$$\lambda_{Fourier} = \frac{4\pi s}{\omega_0 + \sqrt{2 + \omega_0^2}} \quad (5.11)$$

Due to its local aspect, the Morlet wavelet function can be considered as

a wave function. It follows that the time indetermination and the scale indetermination are, respectively, restricted as follows([Farge, 1992]):

$$\Delta t = \frac{l}{\sqrt{2}}, \Delta l = \frac{l}{\sqrt{2\omega_0}} \quad (5.12)$$

Considering the multi-fractal aspect of the ionospheric scintillation, all these aspects of the Morlet wavelet make it well suited to the analysis of the GPS signal during scintillation events.

5.1.6 Signal reconstruction

The reconstruction of the signal from the wavelet coefficient is possible by summing the real part of the wavelet coefficients over the available scales. Let us stress that after performing a wavelet transform of the signal, using an "analysing wavelet" it is possible to reconstruct the original signal using a different wavelet, usually referred to as the "synthesizing wavelet". This can be effectuated using the empirical formula developed by Jean Morlet and defined as follows:

$$x_n = \frac{\delta j \sqrt{\delta t}}{C_\delta \psi_0(0)} \sum_{j=0}^J \frac{\mathbf{R}(W_n(s_j))}{\sqrt{s_j}} \quad (5.13)$$

The parameter $\psi_0(0)$ is used to remove the energy scaling, while the term $\sqrt{s_j}$ is introduced in order to give an energy density aspect to the wavelet transform. C_δ is the result of the reconstruction of the delta function using a given wavelet. This is achieved in the following way. Considering a time series

with a δ function, at time $t = 0$, given by $x_n = \delta_{n0}$, the corresponding Fourier transform is given by $\hat{x}_k = N^{-1}$ and the associated wavelet coefficients can be constructed, using Equation 5.5, as follows:

$$W_\delta(s) = \frac{1}{N} \sum_{k=0}^{N-1} \hat{\psi}^*(s\omega_k) \quad (5.14)$$

The parameter C_δ is then obtained by substituting in 5.13:

$$C_\delta = \frac{\delta\sqrt{\delta t}}{\psi_0(0)} \sum_{j=0}^J \frac{\mathbf{R}(W_n(s_j))}{\sqrt{s_j}} \quad (5.15)$$

Equation 5.13, representing the reconstruction of the signal, can be modified in the following way in order to filter out unwanted components of the signal (such as non-scintillation components, in our case of interest):

$$x_n = \frac{\delta j \sqrt{\delta t}}{C_\delta \psi_0(0)} \sum_{j=j_1}^{j_2} \frac{\mathbf{R}(W_n(s_j))}{\sqrt{s_j}}, \quad (5.16)$$

with j_1 and j_2 representing the lower and the inner cut-off frequencies, respectively.

5.1.7 Multifractal nature of the ionospheric scintillation

Basically, the characteristic spectrum of the ionospheric electron irregularities is composed of different regions: the energy input region, the inertia range and the dissipation region. All of these regions can have different sta-

tistical behaviors. In addition, as discussed in Chapter 4, the background electron number density can present low frequency components, induced by diurnal variations. Finally, one has to take into account the Doppler effect, due to the drift of the irregularities and the motion of the satellite, which induces a trend (a non-stationary component) in the transionospheric signal. In order to characterize the ionospheric scintillation caused by intermediate ($0.1 - 10$ km) scale irregularities at high latitudes, it is important to remove all the non-contributing scales from the GPS L1 signal components. Failure to properly filter-out the signal will inevitably lead to biased observables, e.g., scintillation indices, probability density function or entropy.

During scintillation, the trans-ionospheric signal is characterized by a multi-scale structure and can be decomposed via wavelet transform. In our case, we are interested in the time series of the phase (accumulated Doppler range) and the power components of the GPS L1 signal.

Given a signal $x(t)$, the energy distribution of the wavelet transformed signal is given by $\kappa(s, t)$ defined by

$$\kappa(s, t) = |W(s, t)|^2 \quad (5.17)$$

where $W(s, t)$ is the wavelet coefficient.

The energy distribution in the scale-time space can be represented by a contour (scalogram) as illustrated in Figure 5.4. The multi-scale structure is apparent in the non-homogeneity of the energy distribution, both in time and scale (period). As we will see next, this aspect of the trans-ionospheric signal can be revealed as a very useful property, as it will permit the construction of statistical tools that are of primary importance in the characterization of the ionospheric scintillation.

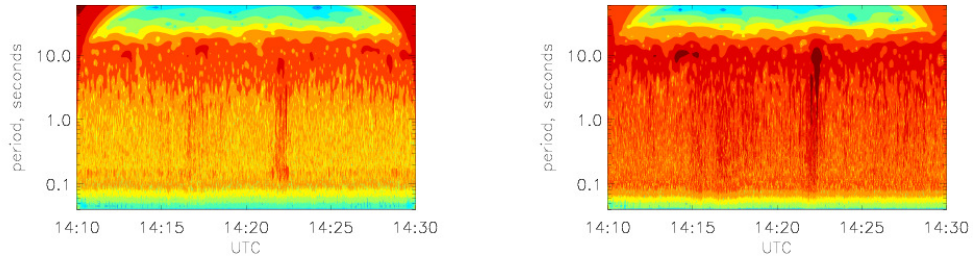


Figure 5.4: Example of a scalogram of the power (left panel) and the phase (right panel) components of the GPS L1 signal, during the scintillation event at Cambridge Bay, 7th of March, 2008, PRN 31.

5.2 Entropy

In statistical mechanics and information theory, the quantification of the information (the construction of the entropy) of a system can be used in order to perform a statistical inference. For example, the probability distribution describing the stochastic behavior of a variable can be defined and charac-

terized, by maximizing the entropy describing the microscopic state. The Boltzmann-Gibbs formalism works very well for systems that are in thermodynamic equilibrium, but for systems that happen to be away from thermal equilibrium and those that are strongly correlated one needs to use other tools to account for the observations. In the case of the ionospheric system, there is a strong ionosphere-magnetosphere and solar wind correlation, and the system shows a multi-fractal structure with strong correlation between different scales. Therefore, it is most likely that the ionospheric system is out of thermal equilibrium.

There is a need to define a generalized entropy that allows the quantification of the disorderliness of the system during ionospheric scintillation. The entropy in question will take into account the non-extensivity of the system. Tsallis, inspired by the probabilistic approach of the multi-fractal geometry, proposed a generalized entropy, characterized by the parameter q , that leads to non-extensive statistics [Tsallis, 1988]:

$$S_q = k_B \frac{1 - \sum_{i=1}^N p_i^q}{q - 1}, \quad (5.18)$$

where p_i represents the probability associated with the microscopic configurations, and N is the total number of elements. The parameter q is a real number, quantifying the non-extensivity, and k_B is the Boltzmann constant.

One can recover the Boltzmann-Gibbs entropy in the limit, $q \rightarrow 1$:

$$S_1 = \lim_{q \rightarrow 1} S_q = k_B \lim_{q \rightarrow 1} \frac{1 - \sum_{i=1}^N p_i \exp[(q-1) \log p_i]}{q-1} = -k_B \sum_{i=1}^N p_i \log p_i \quad (5.19)$$

In the following, in the context of the ionospheric scintillation, we present a technique of constructing the probability p_i and the entropy S_q in the scale domain, using the wavelet transform.

5.2.1 Wavelet-based general Tsallis entropy

In order to study the complexity of the ionospheric plasma dynamics, we construct the Tsallis entropy for the two components of the L1 GPS signal, power and phase, sampled at 50 Hz.

Let's first define a probability based on the distribution of the energy per temporal scale $p(s)$ as:

$$p(s) = \frac{\Sigma_\tau \kappa(s, \tau)}{\Sigma_{\tau, s} \kappa(s, \tau)} \quad (5.20)$$

One can, easily, see that the normalization condition is satisfied, i.e., $\sum_s p(s) = 1$.

It follows that the Tsallis entropy of the system could be expressed under the following form:

$$S_q = k_B \frac{1 - \sum_{i=1}^N p(s_i)^q}{q-1} \quad (5.21)$$

For each temporal scale we have a certain probability and hence the summa-

tion is performed over all possible scales.

5.2.2 Optimization of the detrending scale

Only electron density irregularities with a size below the Fresnel scale contribute to the amplitude scintillation. The phase scintillation, on the other hand, is a result of the irregularities of all resolvable scales. However, the trend, due to the background electron density and the Doppler effect of the relative motion of the satellite with respect to the ionosphere and the ground, is a component of both the amplitude and the phase scintillating signal. This effect induces an aspect of non-stationarity (a non constant mean).

In this thesis, we use the wavelet transform of the signal in order to filter-out all non-scintillation scales from the GPS L1 signal. As a first step, we need to define criteria for the optimization of the cut-off scale. The criteria that we propose are based on the construction of the Tsallis entropy for both the scintillation and non-scintillation component of the system. The system is hence sub-divided into two subsystems, namely, the scintillation and non-scintillation systems, A and B, respectively. The general Tsallis entropy can be, then, given by

$$S_q(A + B) = S_q(A) + S_q(B) + (1 - q)S_q(A)S_q(B) \quad (5.22)$$

The fact that the parameter q quantifies the additivity (extensivity) of the

system is made clear by equation 5.22. In the limit, $q \rightarrow 1$, the entropy converges towards Boltzmann-Gibbs entropy with extensive statistics.

In order to define criteria for the optimum scale, we need to define the expressions of the probabilities associated with scintillation and background variability respectively.

Let's denote by s_{opt} the optimum cut-off scale delimiting the scintillation from the trend. Then the probabilities for scintillation and background are given, respectively, by:

$$p_{scin}(s, s_{opt}, s_{min}, t_{max}) = \frac{\sum_{t=0}^{t=t_{max}} \epsilon(s, t)}{\sum_{t=0}^{t=t_{max}} \sum_{s=s_{min}}^{s=s_{opt}} \epsilon(s, t)} \quad (5.23)$$

$$p_{bg}(s, s_{opt}, s_{max}, t_{max}) = \frac{\sum_{t=0}^{t=t_{max}} \epsilon(s, t)}{\sum_{t=0}^{t=t_{max}} \sum_{s=s_{opt}+1}^{s=s_{max}} \epsilon(s, t)} \quad (5.24)$$

We then define the entropy for each system (scintillation and trend, respectively):

$$S_{q-scin}(s_{min}, s_{opt}) = k_B \frac{1 - \sum_{s_{min}}^{s_{opt}} p_{scin}(s)^q}{q - 1} \quad (5.25)$$

$$S_{q-bg}(s_{opt}, s_{max}) = k_B \frac{1 - \sum_{s_{opt}+1}^{s_{max}} p_{bg}(s)^q}{q - 1} \quad (5.26)$$

The total entropy is then given by the sum of the two entropies associated to both components and a term representing the non-extensivity, proportional to the product of the two:

$$S_q(s_{min}, s_{max}, s_{opt}) = S_{q-scin} + S_{q-bg} + (1 - q) S_{q-scin} S_{q-bg} \quad (5.27)$$

The optimum scale criterion is the maximization of the information for both systems, hence the scale for which the total entropy is a maximum:

$$s_{opt} = \operatorname{argmax}(S_q) \quad (5.28)$$

A maximum for the total entropy S , for given s_{min} and s_{max} can be translated into

$$\frac{\partial S_q}{\partial s_{opt}} = [1 + (1 - q)S_{q-scin}] \frac{\partial S_{q-bg}}{\partial s_{opt}} + [1 + (1 - q)S_{q-bg}] \frac{\partial S_{q-scin}}{\partial s_{opt}} = 0 \quad (5.29)$$

and

$$\frac{\partial^2 S_q}{\partial s_{opt}^2} \leq 0 \quad (5.30)$$

which in turn lead to

$$\left[\frac{p_{bg}(s_{opt} + 1)}{p_{scin}(s_{opt})} \right]^q = \frac{1 + (1 - q)S_{q-bg}(s_{opt} + 1)}{1 + (1 - q)S_{q-scin}(s_{opt})} = \frac{\sum_{s_{opt}+1}^{s_{max}} p_{bg}(s)^q}{\sum_{s_{min}}^{s_{opt}} p_{scin}(s)^q} \quad (5.31)$$

This clearly defines an equation for the optimum scale s_{opt} . Moreover, using equation 5.29, one can show that equation 5.30 reduces to

$$\frac{\partial^2 S_q}{\partial s_{opt}^2} = -2k_B \frac{p_{scin}(s_{opt})^q p_{bg}(s_{opt} + 1)^q}{1 - q} \quad (5.32)$$

which remains negative for all $q < 1$, and assures a maximum for the entropy at s_{opt} .

We follow the approach used by [Tsallis, 1988] in the determination of the entropy. In order to optimize S_q we impose the conditions:

$$\sum_{i=1}^{i=N} p(s_i) = 1 \quad (5.33)$$

where N is the number of scale in the system, $s_1 = s_{min}$, $s_N = s_{max}$, and we have set $k_B = 1$.

$$\sum_{i=1}^{i=N} p(s_i)s_i = \langle s \rangle. \quad (5.34)$$

And define the quantity Γ as follows:

$$\Gamma = S_q + \alpha \sum_{i=1}^{i=N} p(s_i) - \alpha\beta(q-1) \sum_{i=1}^N p(s_i)s_i \quad (5.35)$$

Using a variational principle imposing the condition $\delta\Gamma/\delta p_i = 0, \forall i$, one can determine the expression for the probability:

$$p(s_i) = \frac{(1 - \beta(q-1)s_i)^{\frac{1}{q-1}}}{Z_q} \quad (5.36)$$

with the partition functions given by:

$$Z_q = \sum_{i=1}^N [1 - \beta(q-1)s_i]^{\frac{1}{q-1}} \begin{cases} Z_{q-scin} = \sum_{s_{min}}^{s_{opt}} [1 - \beta(q-1)s_i]^{\frac{1}{q-1}} \\ Z_{q-bg} = \sum_{s_{opt}+1}^{s_{max}} [1 - \beta(q-1)s_i]^{\frac{1}{q-1}} \end{cases} \quad (5.37)$$

These distributions exhibit power law decays for $q < 1$, which can be exploited empirically to estimate the Tsallis index. By fitting the "tails" of the

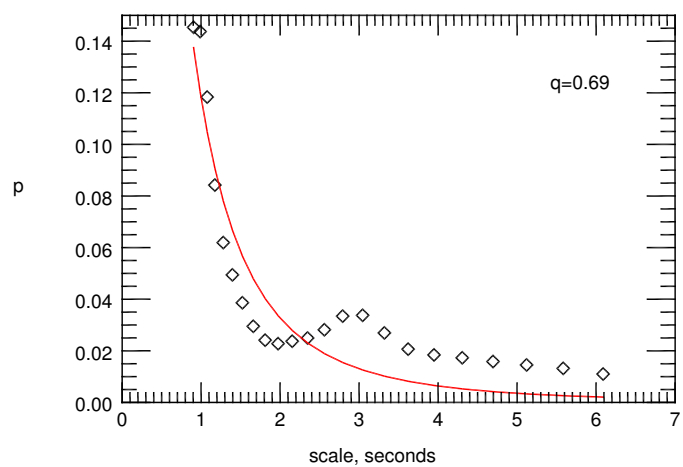


Figure 5.5: The fit of the probability density function during the event at Qikiqtarjuaq, 2011/02/14, PRN 15, dotted points and solid line represent the data and the fit, respectively.

probability function to the expression of p_i one can determine the parameter q . In Figure 5.5, we constructed the probability density function in the space of temporal scales, applying the definition given in equation 5.20 to the data recorded during a scintillation event, for the power component of the signal. A fit to the expression of the probability density function, equation (5.26), is then performed, using the least-squares method. The value of the non-extensivity parameter obtained in this case is $q = 0.69$, indicating a case of super-additivity of the total entropy, since in equation 5.27 the term $(1 - q)$ is positive.

We now go back to expression 5.31 and use the result expressed by equation 5.36 and the partition functions to obtain:

$$\left[1 - \frac{\beta(q-1)}{1 - \beta(q-1)s_{opt}}\right]^q = \frac{\left(1 - \beta \frac{\partial}{\partial \beta}\right) Z_{q-bg}^{q-1}}{\left(1 - \beta \frac{\partial}{\partial \beta}\right) Z_{q-scin}^{q-1}} \quad (5.38)$$

Computing the partition functions for the scintillations and the background components completely defines the optimum scale s_{opt} .

5.2.3 Gaussian statistics

Unlike the power, the phase component of the GPS L1 signal presents a quasi-Gaussian behavior. In order to illustrate this fact, in Figure 5.6, we construct the probability density function for the time series of the recorded GPS L1 signal, during the scintillation event at Qikiqtarjuaq. To quantify the

departure from Gaussianity, we estimate two higher order moments, namely, the kurtosis and the skewness; which are, respectively, defined by

$$k = \int_{-\infty}^{\infty} (x - \mu)^4 P(x) dx \quad (5.39)$$

$$s = \int_{-\infty}^{\infty} (x - \mu)^3 P(x) dx \quad (5.40)$$

where μ is the central moment of the PDF given by:

$$\mu = \int_{-\infty}^{\infty} x P(x) dx \quad (5.41)$$

x being the time series component, and P represents the probability density function of the time series, power or phase.

Therefore, the entropy functional that best characterizes the phase is the Boltzmann-Gibbs entropy, defined as follows:

$$S = -k_B \sum_{i=1}^N p(s_i) \ln p(s_i) \quad (5.42)$$

The system is then subdivided into two subsystems, as in the previous section. For the same event, the entropy variation is examined and analyzed. A similar analysis, as for the power, can easily be reproduced for the case when the classical Boltzmann-Gibbs formalism is applicable, such as in the case of the phase. The result for the optimum scale is given by the following

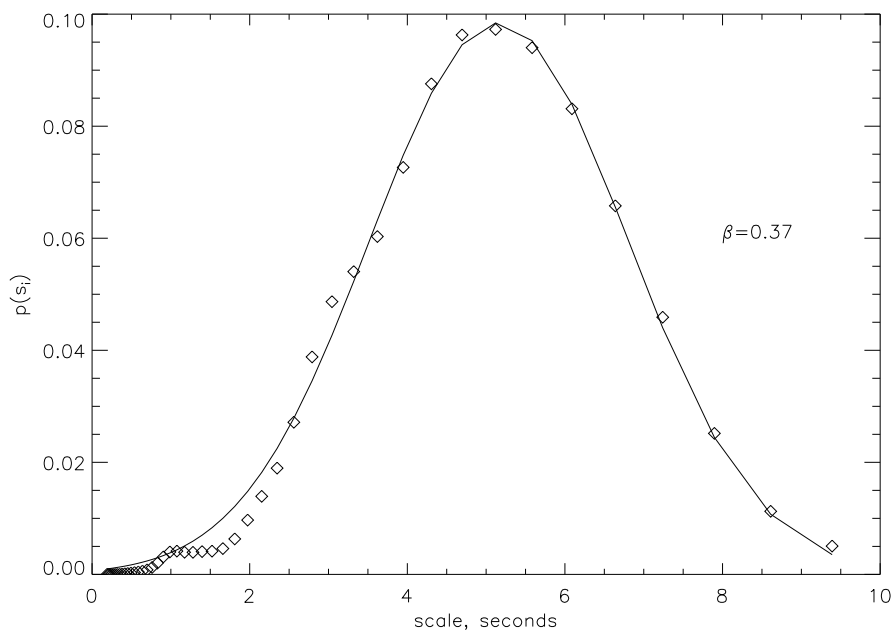


Figure 5.6: The fit of $p(s_i)$ for the phase, solid line, $\beta = \frac{1}{\sigma^2} = 0.37$. The distribution presents quasi-Gaussian statistics, with a kurtosis, $k=3.03$, and a skewness, $s=0.08$.

expression

$$1 = \frac{\sum_{s_{opt}+1}^{s_{max}} e^{-\beta(s_i-1)}}{\sum_{s_{min}}^{s_{opt}} e^{-\beta s_i}} \quad (5.43)$$

or

$$\sum_{s_{min}}^{s_{opt}} e^{-\beta s_i} = \sum_{s_{opt}+1}^{s_{max}} e^{-\beta(s_i-1)} \quad (5.44)$$

By making the following change of variable

$$x_i = s_i - s_{min} \quad (5.45)$$

$$y_i = s_i - s_{opt} - 1 \quad (5.46)$$

we can write the left and right hand side, respectively, as follows:

$$I_1 = \sum_{x_i=0}^{s_{opt}-s_{min}} e^{-\beta x_i} e^{-\beta s_{min}} = e^{-\beta(s_{min}-s_{opt})} \frac{1 - (e^{-\beta})^{s_{opt}-s_{min}+1}}{1 - e^{-\beta}} \quad (5.47)$$

$$I_2 = \sum_{y_i=0}^{s_{max}-s_{opt}-1} e^{-\beta y_i} e^{-\beta s_{opt}} = \left(\frac{1 - (e^{-\beta})^{s_{max}-s_{opt}}}{1 - e^{-\beta}} \right) e^{-\beta s_{opt}} \quad (5.48)$$

After equating the two terms, and some algebra, one can recover the following expression for the optimum scale:

$$s_{opt} = s_{min} + \frac{1}{\beta} \ln \left(\frac{1 + e^{-\beta}}{1 + e^{-\beta(s_{max}-s_{min})}} \right) \quad (5.49)$$

where s_{min} corresponds to the lowest scale for which the wavelet energy density is non-zero.

Therefore, for the phase component of the GPS L1 signal, the determination of the optimum scale depends only on the fit of the PDF, namely the parameter β and the scale s_{min} . Figure 5.6 illustrates the case of the scintillation event at Qikiqtarjuaq, 2011/02/14, PRN 15. In this case the fit has given $\beta = 0.37$ and $s_{min} = 0.8$, for which the result is $s_{opt} = 3.26$ s.

5.3 Summary and conclusion

The general Tsallis entropy allows us to take into account the extensivity of a system. In the context of ionospheric scintillation, power components of the signal exhibit, mostly, a non Gaussian behavior and an extensive statistics. Therefore, in order to compute the entropy of the power, we construct the General Tsallis entropy using the wavelet-based probability density function. On the other hand, for the phase component of the signal, Gaussian statistics are exhibited and the appropriate entropy tends to be the Boltzmann-Gibbs entropy.

The GPS L1 signal contains all the contributions, namely, the diurnal variations of the electron background and the Doppler shift due to the ionospheric turbulence. In order to isolate scintillation components, we use the maximum entropy principle by writing the system as the sum of the scintillation components and the rest of the contributions. The scale corresponding to the maximum entropy is then defined as the scale for which the energy is injected during ionospheric scintillation (outer scale), or the Fresnel scale, in the case

of power scintillation (diffraction component).

Chapter 6

Intermittent scintillation

A signal is intermittent if it is characterized by large amplitude fluctuations with finite probability. This leads to the build up of "tails" in the corresponding PDF, which define the departure from Gaussian statistics. In our context, defining a suitable distribution, within the scope of understanding the mechanism at play in the ionospheric scintillation, is of fundamental interest. A non-Gaussian signal is often characterized by a flat and skewed distribution. The flatness of the probability density function is often quantified using the fourth normalized moment, the kurtosis. The asymmetry, on the other hand, is quantified via the third normalized moment, the skewness. For a Gaussian distribution, the flatness is constant and equals to 3. For an intermittent signal, presenting a bursty behavior, the kurtosis will depart from this value.

In the context of ionospheric scintillation, one can argue that the turbulent

nature of the ionospheric plasma translates into an intermittent signature in the scintillation signal. We hereby propose a model that enables the quantification of the intermittency in the signal.

6.1 A simple intermittency model

6.1.1 Higher order moments

In the following, we start by introducing an example that enables the quantification of intermittency in the signal. In order to do that, we start by performing a multi-scale analysis of the GPS L1 signal by constructing the differential signal defined as $\delta A(\tau, t) = A(t) - A(t + \tau)$ over various temporal scales τ , where A represents the power.

By reproducing an analogous argument to the one used by Chatwin and Sullivan, [Chatwin and Sullivan, 1989], presented in the context of the advection and diffusion of the pollutant in a neutral fluid, we define the probability density function:

$$P(x; \tau, t) = \frac{d}{dx} [\text{prob}\{\delta A(\tau, t) \leq x\}] \quad (6.1)$$

with x taking all the possible values of $\delta A(\tau, t)$. $P(x; \tau, t)\delta x$ can be interpreted as the probability for the amplitude $\delta A(\tau, t)$ to fall between x and $x + \delta x$. The equation governing the evolution of the probability $P(x; \tau, t)$ can be derived from the equation governing the evolution of the amplitude

$\delta A(\tau, t)$.

In the absence of ionospheric turbulence, and the presence of a uniform ionospheric electron density, one should not expect scintillations and $\delta A(\tau, t)$ should vanish or take a value $x_0(\tau)$, which in turn leads to the following probability density function

$$P(x; \tau, t) = \Gamma(\tau, t)\delta(x - x_0) + (1 - \Gamma(\tau, t))\delta(x) \quad (6.2)$$

where $\Gamma(\tau, t)$ represents the degree of intermittency of the signal.

We are now able to compute all the moments of the probability density function, and in particular the mean μ , the variance σ , the skewness S and the kurtosis K using the following definitions:

$$\begin{aligned} <[\delta A(\tau, t)]^n> &= \frac{\mu_n}{\sigma^n} \\ \mu_n(\tau, t) &= \int_0^\infty x^n P(x; \tau, t) dx \end{aligned} \quad (6.3)$$

This leads to

$$\begin{aligned} \mu &= \mu_1 = \Gamma(\tau, t)x_0(\tau) \\ \sigma^2 &= \mu_2 - \mu_1^2 = x_0(\tau)^2(\Gamma(\tau, t) - \Gamma^2(\tau, t)) = \mu(x_0 - \mu) \\ S^2 &= \frac{(x_0 - 2\mu)^2}{\mu(x_0 - \mu)} \\ K &= \frac{(x_0^2 - 3x_0\mu + 3\mu^2)}{\mu(x_0 - \mu)} = S^2 + 1 \end{aligned} \quad (6.4)$$

Notice that both relationships between σ^2 and μ on the one hand, and K and S^2 on the other, respectively, are independent of the intermittency factor Γ . Using the expression for μ in terms of Γ and x_0 leads to the following expressions for the skewness S and the kurtosis K

$$\begin{aligned} S^2 &= \frac{(1 - 2\Gamma)^2}{\Gamma(1 - \Gamma)} \\ K &= \frac{(1 - \Gamma)^3 + \Gamma^3}{\Gamma(1 - \Gamma)} \end{aligned} \quad (6.5)$$

Let us assume, for the sake of argument, that the intermittency factor can have the following form:

$$\Gamma(\tau, t) = \frac{1}{1 + e^{\tau_i/\tau}} \quad (6.6)$$

where τ_i is an arbitrary constant to be determined. This then leads to

$$S^2 = e^{\tau_i/\tau} + e^{-\tau_i/\tau} - 2 = 2 [\cosh(\tau_i/\tau) - 1] = 4 \sinh^2 \left[\frac{1}{2} \frac{\tau_i}{\tau} \right] \quad (6.7)$$

$$K = e^{\tau_i/\tau} + e^{-\tau_i/\tau} - 1 = 2 \left[\cosh(\tau_i/\tau) - \frac{1}{2} \right] = 4 \sinh^2 \left[\frac{1}{2} \frac{\tau_i}{\tau} \right] + 1 \quad (6.8)$$

In the limit of long time lags τ , the skewness vanishes and the kurtosis tends toward a constant value of one (1). For short time lags, both the skewness and the kurtosis diverge.

6.1.2 Castaing distribution

We shall analyze these results after looking at another type of probability distribution function (PDF) introduced by [Castaing et al., 1990] while attempting to understand experimental signatures observed in a turbulent neutral fluid, namely the differential velocity signal. Castaing and Gagne constructed a PDF by modifying Kolmogorov's original argument of energy cascade, which he introduced in 1941 (see for example [Frisch, 1995]). Kolmogorov's argument postulates that the rate of energy transfer ϵ between scales in the inertial range is constant; the self-similarity assumption along with the use of the central limit theorem allow the estimation of the variance of the distribution of velocity fluctuations using dimensional arguments only, and which lead to $\sigma \sim (\epsilon l)^{1/3} \rightarrow \ln(\sigma) \sim \frac{1}{3}\ln(\epsilon) + \frac{1}{3}\ln(l)$ (where l represents the fluctuation scale and σ the variance of the normal distribution in the case of a constant rate of energy transfer). The next assumption consists of postulating a scale dependent rate of energy transfer between scales in the inertial range as suggested by Kolmogorov: a suggestion adopted by Castaing who postulated that the PDF is the result of the superposition of normal distributions whose variances are log-normal distributed. The PDF is then constructed using the convolution of a normal distribution for the fluctuations and a log-normal distribution for the variances. The resulting PDF can be written in the following closed form:

$$P_\lambda(\delta A(\tau, t)) = \frac{1}{\lambda 2\pi} \int_0^\infty \exp\left(-\frac{\delta A(\tau, t)^2}{2\sigma^2}\right) \exp\left(-\frac{\ln^2(\frac{\sigma}{\sigma_0})}{2\lambda^2}\right) \frac{d\sigma}{\sigma^2} \quad (6.9)$$

where λ is a parameter that quantifies the degree of non-Gaussianity of the distribution and σ_0 is the most probable value of the standard deviation.

The scale-dependent rate of energy transfer leads to distributions that deviate from the conventional Gaussian/normal distributions. The Castaing distributions, through the superposition of normal distributions with varying variances, are broader than the classical thermal distributions and possess tails that suggest intermittency.

Our primary goal in the present study is to evaluate the fourth moment, kurtosis, of the PDFs. A complete study would have to include the odd moments. However, it has been argued, as mentioned earlier that one potential measure of intermittency is the flatness/kurtosis of the PDF, which we propose to quantify for the power component of the scintillations (see [Batchelor and Townsend, 1949]). We have defined above the following quantities:

$$\langle (\delta A(\tau, t))^n \rangle = \frac{\mu_n}{\sigma^n}$$

where μ_n is the central moment of the PDF given by:

$$\mu_n = \int_0^\infty x^n P(x) dx$$

We examine three different cases of scintillation events using the CHAIN data from three different stations (Qikiqtarjuaq, Resolute Bay and Iqaluit) in order to illustrate the intermittent behaviour of the signals studied.

Figures 6.1, 6.3 and 6.2 illustrate differential PDFs, with given temporal lags τ (0.02 s, 0.15 s and 0.2 s) for the three events and a fit is performed using the Castaing distribution. We observe a good fit of the “tails” which represent the non-Gaussian nature of the signals. Along with the kurtosis, the parameters λ and σ_0 constitute a good representation of the intermittency of the signal and the flatness of the distribution as can be seen in the case of σ_0 for example; the event recorded at Iqualuit has the flattest distribution obtained corresponding to the highest value of σ_0 (11.15 against 6.71 and 6.95 for the remaining two events).

An interesting question may be raised as to whether the intermittency at small scales observed in fluid turbulence could manifest itself in a similar way for ionospheric scintillation, and if it does, would it mean that the actual plasma within the ionospheric layer is in an intermittent state?

In order to obtain a preliminary indication about the answer to the first part of the question, in Figure 6.4 we illustrate the behaviour of the kurtosis estimated for different time lags during the event at Qikiqtarjuaq for a time of integration of 5 minutes from 19:25 to 19:30 UT, and a cut off scale of 0.095 seconds. The results reveal that the kurtosis decreases with increasing τ suggesting that the intermittency is most likely prevalent at small temporal lags. This is consistent with the model presented above, as it is illustrated in Figure 6.4 where we have fitted the kurtosis versus time-lag profile with the analytical function $K = 4 \sinh^2 \left[\frac{1}{2} \frac{\tau_i}{\tau} \right] + 4$, with $\tau_i = 1.75s$ corresponding to

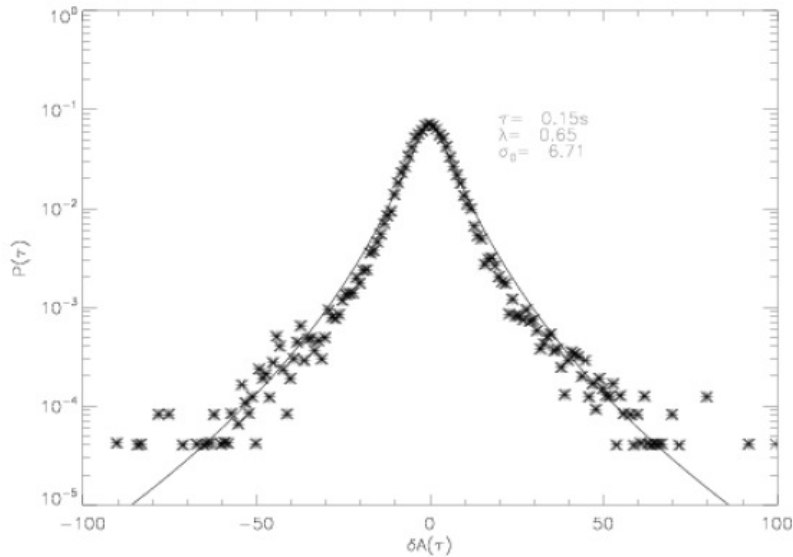


Figure 6.1: Differential power signal recorded at Qikiqtarjuaq during scintillation on the 14th of February 2011 for a time lag of 0.15 second, PRN 15.

the best fit. There is a vertical shift of 3 of the analytical function resulting from the simple intermittency model proposed; this suggests that one would have to use a different functional form for the intermittency factor for the kurtosis to converge towards the Gaussian value.

6.2 Discussion and conclusion

Castaing distributions, constructed using the convolution of a Gaussian with a log-normal distribution of the variance, were considered as fits of the scintillation data. The Castaing distribution functions provided a good fit of

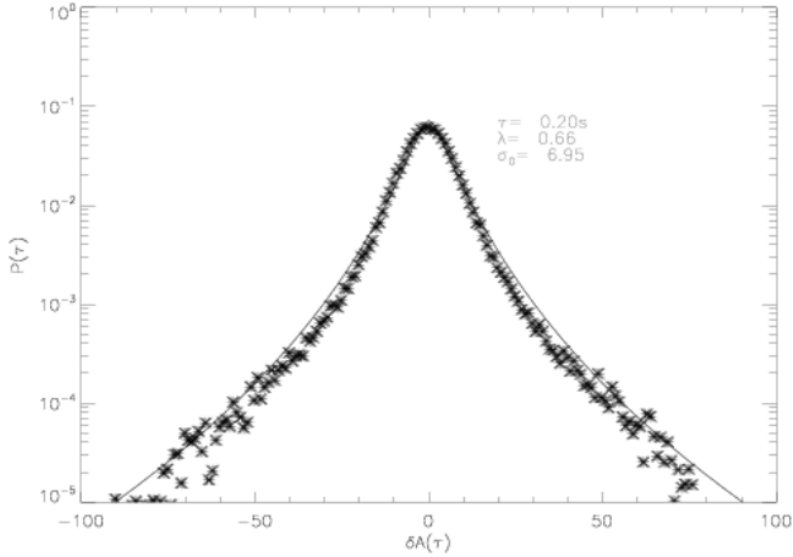


Figure 6.2: Differential power signal recorded at Resolute Bay during scintillation (21 October 2010) for a time lag of 0.2 second, PRN 19

the power fluctuation signal; they also provide a two-parameter description of the statistical characteristics of the differential signal. We quantified the intermittency of the signal by evaluating the kurtosis of the probability density function for different time lags. It has been found that the signal is intermittent for small temporal scales. This is a natural result that has been confirmed by various experiments in the context of neutral fluid turbulence as well as in laboratory plasmas where the tails of the probability density function have been found to be more important for small-scale fluctuations of the floating potential at the edges of the plasma.

We have also proposed a model for the PDF of the power fluctuations based on intermittency. The fourth moment of the proposed PDF suggests a high

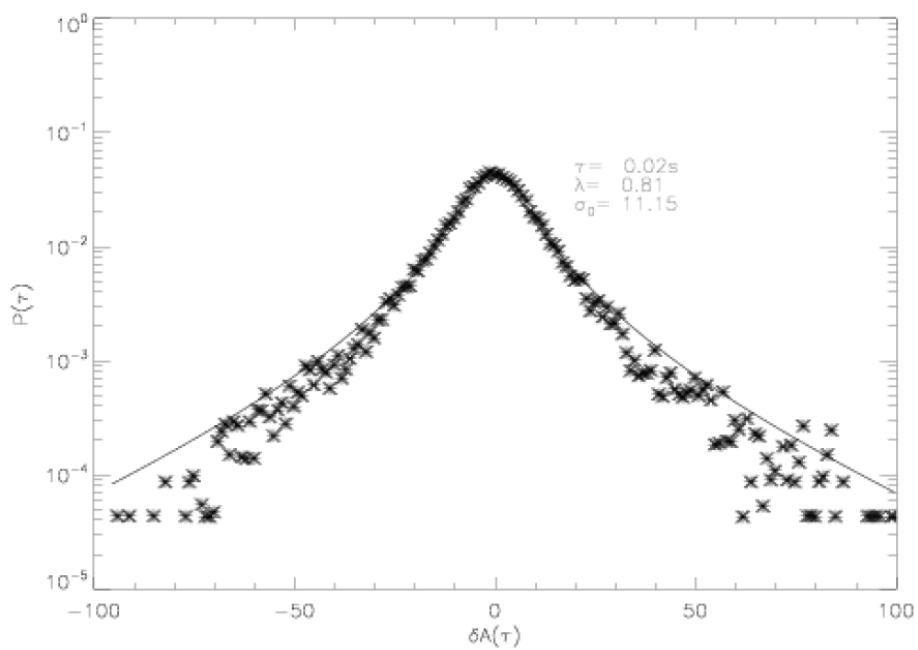


Figure 6.3: Differential power signal recorded at Iqaluit during scintillation on the 22nd of February 2011 for a time lag of 0.02 second, PRN 31

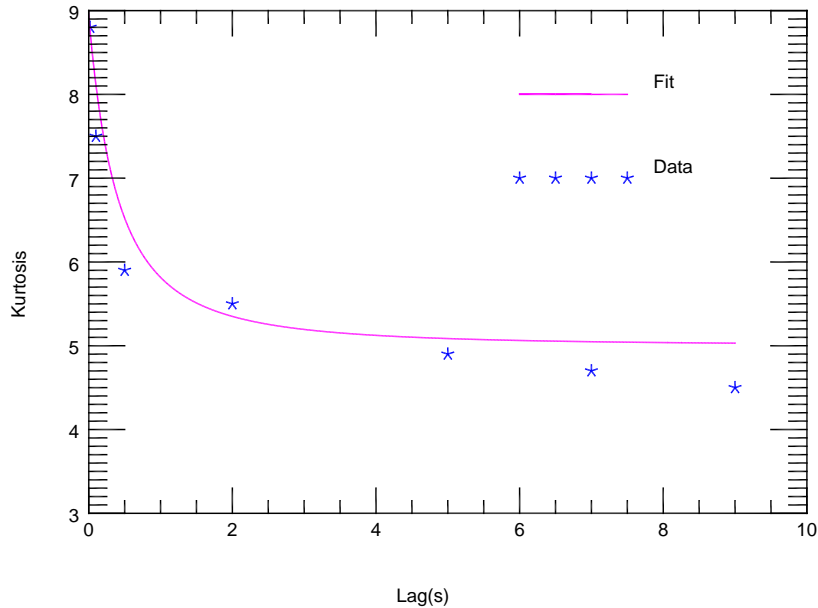


Figure 6.4: Example of Kurtosis vs temporal lag for the event at Qikiqtarjuaq during scintillation on the 14th of February 2011. Starting from a lag value of 0.02s a fast decrease in the kurtosis is observed for larger time lags. The fit is performed using the relation. $K = 4 \sinh^2 \left[\frac{1}{2} \frac{\tau_i}{\tau} \right] + 4$, with $\tau_i = 1.75s$

degree of intermittency at small scales. The fit of the actual data with the proposed model suggested another form of intermittency factor should be considered.

The proposed model is key to investigating a potential one-to-one relationship between the in situ statistical behaviors of the turbulent plasma and those of the components of the diffracted or refracted transionospheric signal (scintillation signal). The present characterization gives a better insight into the mechanisms at play during a scintillation event with specific statistical signatures, for example, as mentioned already in a Kolmogorov-like behavior.

Chapter 7

Statistical characteristics of ionospheric scintillations

Scintillation measurements allow us to unveil a different type of information about the structure of the ionospheric electron density irregularities. For example, the power spectra of the amplitude and the phase components of the GPS L1 signal can lead to different indications about the form of the power spectrum of the electron density irregularities in the ionospheric layer [Yeh and Liu, 1982]. However, the description of the ionospheric turbulence can also be made using the concept of chaos. In addition to the entropy, an independent measure known as fractal dimension can be used to characterize the chaotic behavior of the system and quantify the corresponding dimensionality.

In the present chapter, we investigate the chaotic behavior of the ionospheric

scintillation using the GPS L1 signal components, namely, the phase and the power, by estimating the information dimension associated to the system; the computation of the fractal dimension, defined later in the text, along with the Tsallis entropy are used in order to quantify the chaoticity of the ionospheric system.

7.1 Phase space reconstruction

7.1.1 Information Dimension

In order to reconstruct the phase-space of a time series, the conventional approach is to use the method of time delay coordinates. A vector \vec{X}_i in an m -dimensional phase space is obtained by considering the delayed time series as coordinates, i.e.,

$$\vec{X}_i = (x(t_i), x(t_i + \tau) \dots x(t_i + (m - 1)\tau)) \quad (7.1)$$

where τ is the time delay and t_i is the discrete time, with $\tau = n\Delta t$ and Δt being the time resolution of the system.

In previous studies, it has been shown that in order to reconstruct the phase-space of dimension d the embedding dimension m must be at least equal to $2d + 1$ [Takens, 1981]. The choice of the delay τ is of primary importance since the coordinates of the reconstructed phase-space must be statistically independent.

One way of choosing the optimum τ is to use the mutual information of the two vectors considered in the phase space reconstruction:

$$MI(X, Y) = H(X) + H(Y) - H(X, Y) \quad (7.2)$$

where $H(X_i)$ is the entropy of the i -th vector considered in the phase space reconstruction:

$$H(X) = -\sum P_X(X) \log P_X(X) dX \quad (7.3)$$

and

$$H(X, Y) = - \int P_{XY}(X, Y) \log P_{XY}(X, Y) dX \quad (7.4)$$

where $P(X)$ is the probability density function associated to the time series X and $P(X, Y)$ is the joint probability associated to X and Y .

The optimum value of the delay τ is then chosen as the delay for which the mutual information is minimized, minimizing the correlation between the two coordinates of the reconstructed phase-space [Fraser and Swinney, 1986]. In Figure 7.1, the variation of the mutual information with the time delay is illustrated for a scintillation event. The corresponding optimum time delays are 0.3 seconds and 0.4 seconds for the phase and the power, respectively.

7.1.2 Attractor dimension reconstruction

Before going any further in the present analysis, let us define the concept of an attractor. An attractor of a given dynamical system is a set of numerical values, in the phase-space, towards which the system tends to evolve from different initial conditions.

Let us give an example of a method of dimensionless reconstruction of the attractor proposed by Grassberger and Procaccia [Grassberger and Procaccia, 1983]. The method consists in counting the number of points N_{X_0} within a sphere of radius r , in phase space, centered at a certain point X_0 and computing the dimension D_I defined as:

$$D_I = \lim_{r \rightarrow 0} \frac{\ln N_{X_0}(r)}{\ln r} \quad (7.5)$$

For a sufficiently large embedding dimension m , D_I should become independent of m . The value of D_I is then said to be the lower bound of the fractal dimension d . In Figure 7.2, we illustrate the phase-space reconstruction for both the power and phase components of the signal. For the shortest time delay, $\tau = 0.02$ s, the attractor is stretched due the high degree of correlation between components in the phase space. The estimation of the attractor dimension will be underestimated in this case. For the optimum time delay τ the attractor presents a fairly good symmetry in the phase space.

In the context of the present study, we propose a new definition of the fractal dimension based on the wavelet transform of the GPS L1 scintillating signal.

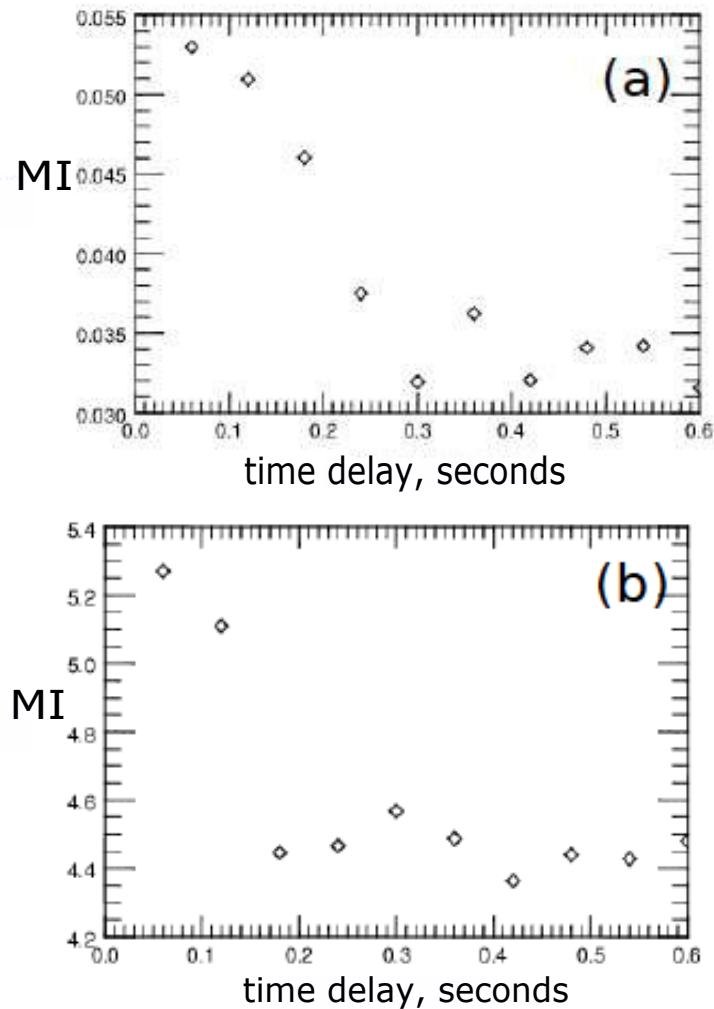


Figure 7.1: Illustration of mutual information against time delay obtained from the detrended power (a) and phase (b) components during the event at Qikiqtarjuaq, 2011/02/14, PRN 15.

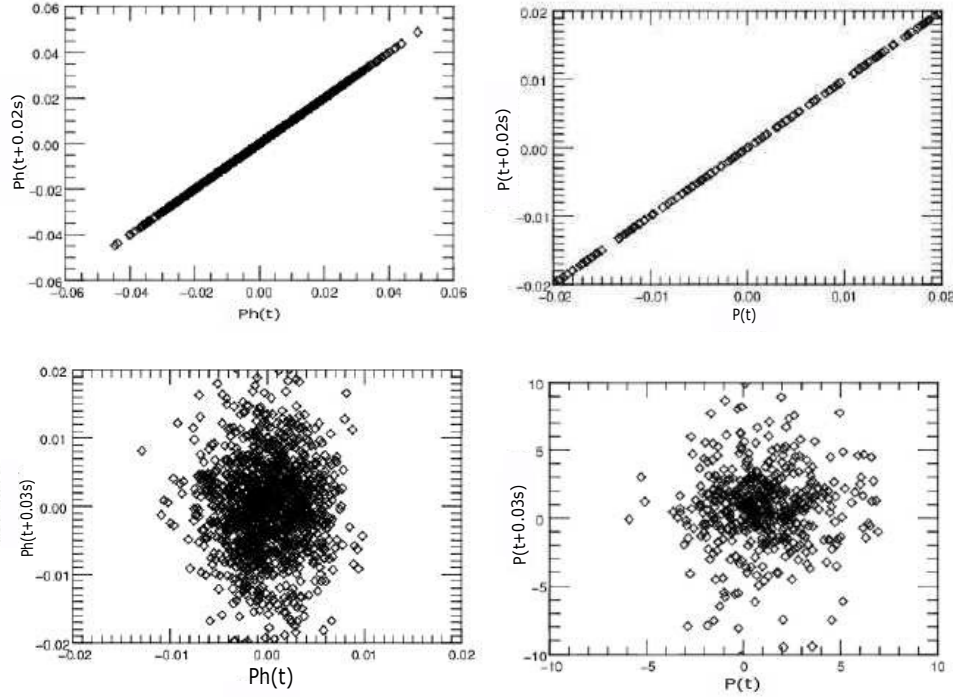


Figure 7.2: Example of a scintillation event at Qikiqtarjuaq, 2011/02/14, PRN 15. The phase space reconstruction is presented for two temporal delays ($\tau = 0.02 \text{ s}, 0.03 \text{ s}$), for the phase and the power components of the GPS L1 signal.

7.1.3 Wavelet-based fractal dimension

By definition, the wavelet transform gives the distribution of the energy of the signal in phase space. Therefore, there is a possibility to define a fractal dimension based on the distribution of the energy.

Let us define the fractal dimension of the signal for a given time interval T

as follows:

$$D(T, a : b) = \frac{\int_0^T \int_a^b \epsilon(s, t) dt ds}{\int_0^T \int_{s_{min}}^{s_{max}} \epsilon(s, t) dt ds} \quad (7.6)$$

where a and b define a band in the scale range (chosen arbitrarily). In the following, we chose s_{min} and s_{max} as the upper and the lower band limits, respectively, using the entropy maximization criterion.

During scintillation, an increase in the dimensionality of the signal fluctuation occurs. In Figure 7.3, as an illustration of the behavior of the dimensionality of the ionospheric scintillation, an example of a scintillation event is given. One can notice that the variation is representative of the bursty aspect of the signal, associated with the occurrence of the scintillation.

Fractal dimensions are very important statistical techniques that can be used to describe the dynamical nature of the ionospheric system. Therefore, the benefits of computing the wavelet-based fractal dimension of the system are twofold: it enables us to quantify the “severity” of a scintillation event and qualify the statistical properties of the system. For these reasons, in the present study, we adopt the wavelet-based fractal dimension as a scintillation index.

7.2 Climatology

Climatology constitutes an important component in the modeling of the ionospheric scintillation. Indeed, climatology gives information about the statis-

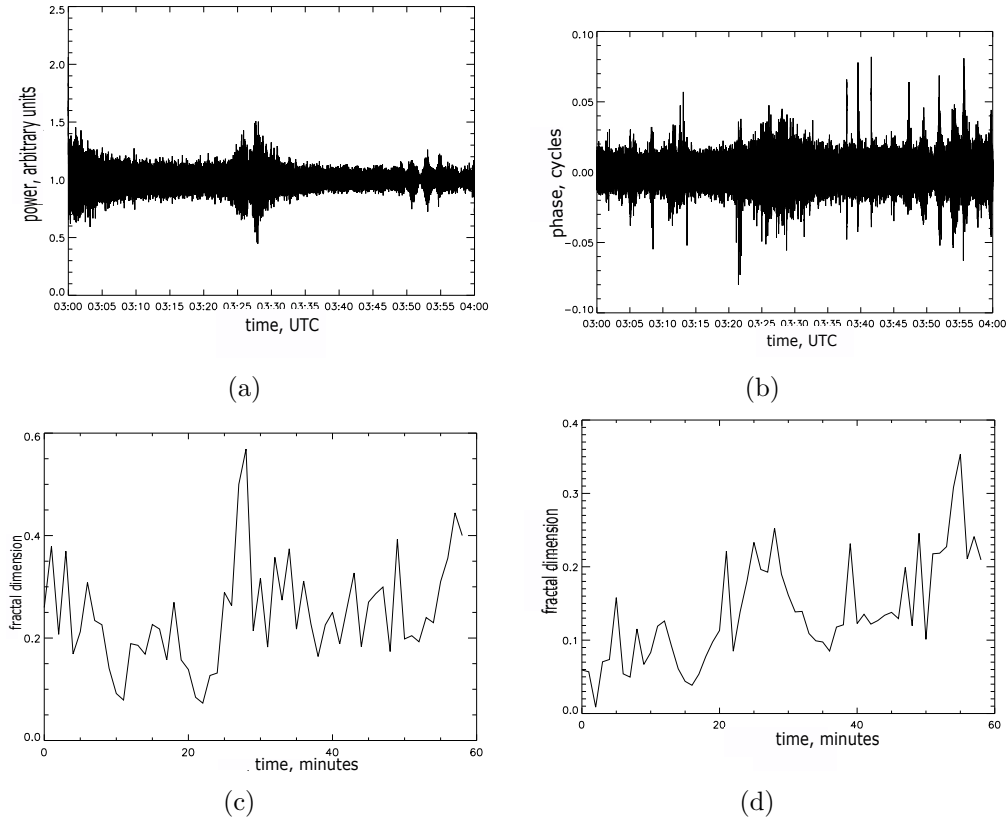


Figure 7.3: Illustration of the variation of the fractal dimension with the occurrence of the power scintillation (left panel) and phase scintillation (right panel) on 01 March 2009 on PRN 20 between 03:00 and 04:00 UTC at Cambridge Bay (69.10° N 254.88° E).

tical behavior of different ionospheric observables in space and time domains, which in turn gives an insight into the mechanisms at play during ionospheric scintillation. Different climatology studies have been used in the past to construct ionospheric scintillation models [Secan et al., 1995, 1997].

In previous studies, high latitude scintillation climatology studies were mainly performed in the VHF/UHF range, using geostationary satellites or middle to low earth orbiting satellites. In the context of the study and the investigation of the high latitude ionospheric plasma, the High Latitude Research Satellite (HILAT) was launched in the 1980s, transmitting at five frequencies: 138, 390, 413, 536, 1239 MHz [Gola et al., 1992].

Seasonal and diurnal variations in ionospheric scintillation were observed at high and low latitudes. It was also found that scintillations at VHF/UHF frequency ranges exhibited seasonal and UT variations [Aarons, 1982]. Let us stress that these studies were performed using only S_4 , defined as the normalized variance of the intensity component of the GPS signal, as a scintillation index.

More recently, Mushini [2013] performed an analysis of ionospheric scintillation using CHAIN. Both amplitude and phase components of the GPS L1 signal were considered in the study. It was found that the power spectra of the phase and the amplitude components of the GPS L1 signal exhibit different behaviors. More specifically, it was found that the power law, characterizing the power spectra of the amplitude scintillation, breaks at the Fresnel frequency, while contributions from all scales constitute the phase

| Station | Geog. Lat. ($^{\circ}$ N) | Geog. Long. ($^{\circ}$ E) | Corrected Geomag. Lat. ($^{\circ}$ N) | Corrected Geomag. Long. ($^{\circ}$ E) |
|---------------|-------------------------------|--------------------------------|-------------------------------------------|--------------------------------------------|
| Eureka | 79.99 | 274.10 | 88.10 | 329.86 |
| Resolute Bay | 74.75 | 265.00 | 83.13 | 320.61 |
| Pond Inlet | 72.69 | 282.04 | 81.67 | 0.69 |
| Cambridge Bay | 69.12 | 254.97 | 77.24 | 310.11 |
| Taloyoak | 69.54 | 266.44 | 78.75 | 329.70 |
| Hall Beach | 68.78 | 278.74 | 78.33 | 353.45 |
| Qikiqtarjuaq | 67.53 | 295.97 | 75.77 | 22.57 |
| Iqaluit | 63.73 | 291.46 | 72.85 | 14.04 |
| Sanikiluaq | 56.54 | 280.77 | 67.19 | 356.44 |

Table 7.1: The CHAIN stations and the corresponding geographic and corrected geo-magnetic coordinates.

scintillation.

In the present climatology study, we use a set of CHAIN data for the period extending from March 2009 to March 2011. The geographic and magnetic coordinates of the CHAIN stations, used in the present study, are given in Table 7.1.

The raw phase and power components of the GPS signal were detrended using the wavelet transform and constrained by the entropy maximization criterion introduced in Chapter 5. All the scintillation observables considered are derived from the detrended data.

In the context of the investigation of the ionospheric climatology, let us stress the importance of using the Altitude Corrected Geomagnetic Coordinates (AACGM) [Baker and Wing, 1989; Shepherd, 2014]. Where the geomagnetic coordinates are defined in terms of magnetic latitude (MLAT) and magnetic

longitude. In order to have a reference with respect to the position of the sun, we use the magnetic local time (MLT) [Prikryl et al., 2011; Spogli et al., 2009]. After an investigation of the ionograms during the scintillation events, it was concluded that most of the irregularities were at an altitude of 350 km. Therefore, in the following we consider the Ionospheric Pierce points to be located at this altitude. In addition, in order to minimize the multipath effect, all the events considered were recorded for an elevation greater than 30° .

In order to perform an analysis of the seasonal variations of the various ionospheric observables, the year has been divided into four equal intervals of three months, each one being a period of three months centered on equinoxes and solstices [Prikryl et al., 2011]:

Winter → November to January

Spring → February to April

Autumn → August to October

Summer → May to July

Using the presented frame, we proceeded with the climatology study. The following text details the procedure used in this analysis.

7.2.1 Optimum scale

Different studies have been conducted in the past in order to have an insight into the range of scales of ionospheric irregularities responsible for the iono-

spheric scintillation [Basu et al., 1990, 1988, 1987; Cronyn, 1970; Tsunoda, 1988; Urneki et al., 1977]. This is basically done in an effort towards understanding the mechanisms at play and the main irregularity sizes. It has been found that the spectral index depends on the geometry of the propagation path with respect to the magnetic field. Also, it has been shown that, at high latitude, the spectrum along the magnetic field exhibits a larger slope than across the field [Wernik et al., 1990].

7.2.1.1 Analysis of the optimum scale using the entropy maximization technique

In the present section, the variation of the optimum temporal scale/frequency obtained by maximizing the wavelet-based entropy of the system was investigated.

In Figure 7.4, we illustrate the PDF of the optimum scale estimated for the phase component of the GPS L1 signal. One can notice multiple peaks corresponding to multiple optimum scales. During winter and summer, we observe two major peaks. During winter, there is a higher probability of having smaller optimum scales.

As illustrated in Figure 7.4, there is a clear change in terms of the value of the PDF at the most probable optimum scale (the mode): the corresponding probability shows the highest value during summer and decreases during winter.

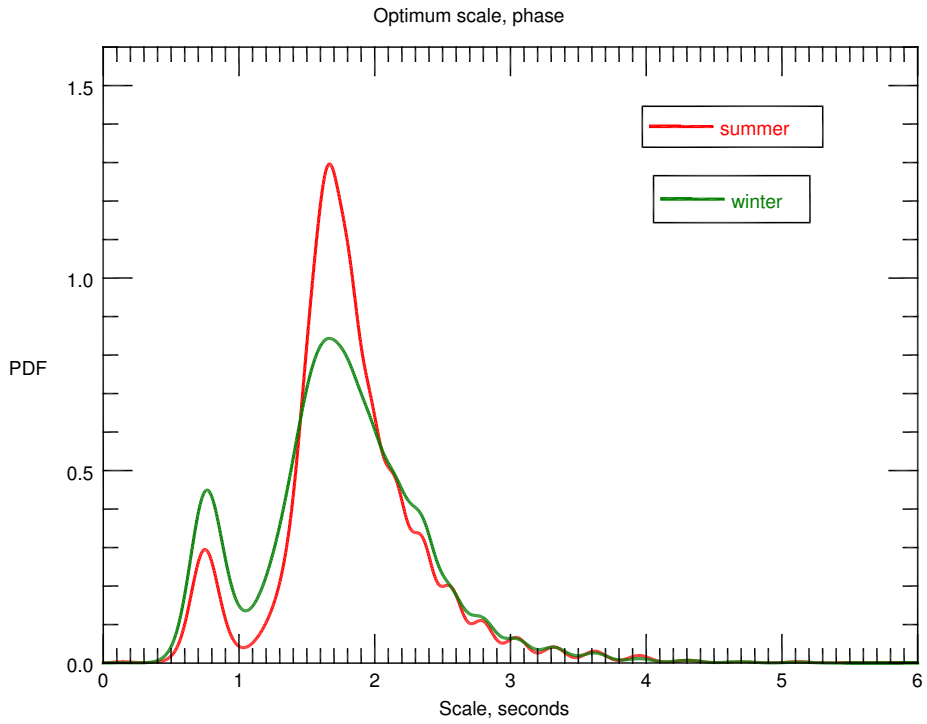


Figure 7.4: Probability density function of the optimum scale associated with the phase component of the signal.

The PDF describing the optimum scale corresponding to the power component is depicted in Figure 7.5. It shows an average scale smaller than the one corresponding to the phase component. During the winter the probability attributed to the smallest scale (laying on the left tail of the distribution) is at its highest.

The power and phase PDFs present the following discrepancies. The phase component has a PDF with two peaks, corresponding to two major optimum

scales. This is most likely a signature of two different mechanisms with energy injected at two different scales. However, one has to keep in mind the role played by the Fresnel scale, defined by $d_f = \sqrt{\lambda z}$, where λ is the wavelength of the transionospheric radio wave and z the height of the diffracting ionospheric layer. For irregularities larger than the Fresnel scale, the diffraction component is minimum. Therefore, given that the observables obtained in our case are derived from time series, an ambiguity arises: the Fresnel scale cannot be directly estimated, but can be computed, approximately, using the Taylor hypothesis and assuming a certain plasma drift velocity V . The Fresnel scale can be then obtained simply by $d_F = \frac{V}{f_F}$. The ambiguity arises from the competition between the drift velocity variation and the variation of the height of the irregularities. Nevertheless, to a first approximation, given that most of the scintillation events were associated with irregularities at a height of 350 km and assuming a drift velocity of around 350 m/s (typical value in the high latitude region [Mushini, 2013]), one can argue that in general the optimum scale is representative of the outer scale, or the largest scale at which the energy is injected.

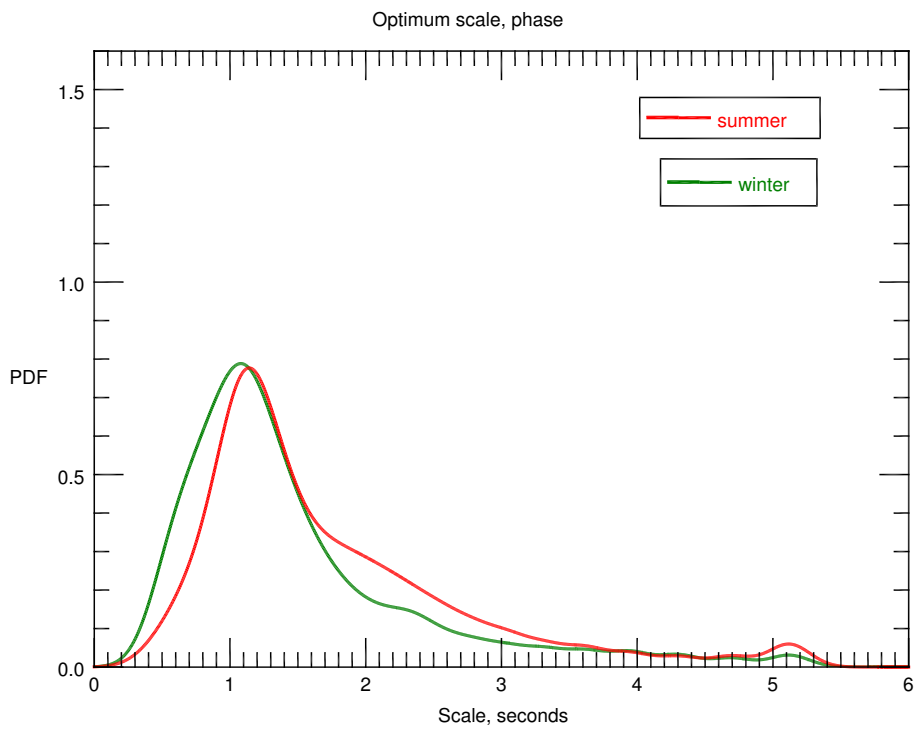


Figure 7.5: Probability density function of the optimum scale associated with the power component of the signal.

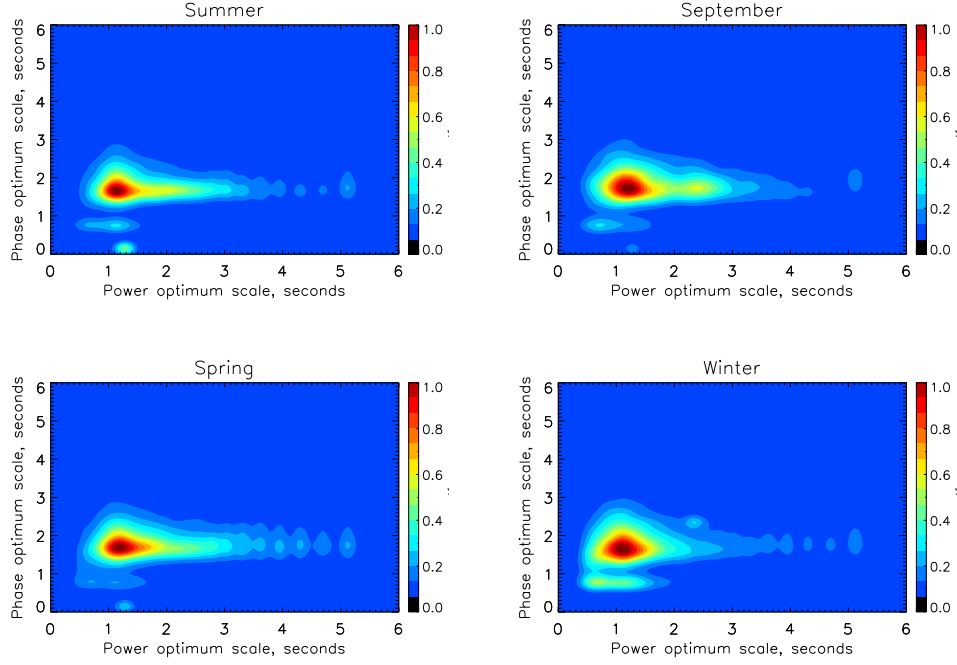


Figure 7.6: Joint probability density function constructed for the power and phase components for the winter, summer and solstices.

In Figure 7.6, we constructed the joint probability density function of occurrences of the optimum scale for the phase and the power components. One can notice the asymmetric aspect of the distribution. During the summer and the solstices, there is a built up of a tail for the power component for a fixed value of the optimum scale associated with the phase component. During winter, the built up of the tail is minimum, and a singularity at around 1 s arises for the phase component.

7.2.1.2 Variation of the optimum scale with the elevation angle

It has been found that the spectral properties of a scintillating trans-ionospheric signal depend on the propagation path [Wernik et al., 1990]. More particularly, the spectral properties of the trans-ionospheric radio signal on the ground depend on the angle between the ray path and magnetic field lines, these being quasi-perpendicular in the high latitude region.

In the following, we particularly investigate the dependence of the optimum scale with the elevation angle.

In Figure 7.7, we present the PDF of the optimum scale occurrences for different intervals of elevation. It is clear that, for higher elevation angles, the optimum scale is predominantly smaller than at low elevation angles, for both the phase and power components.

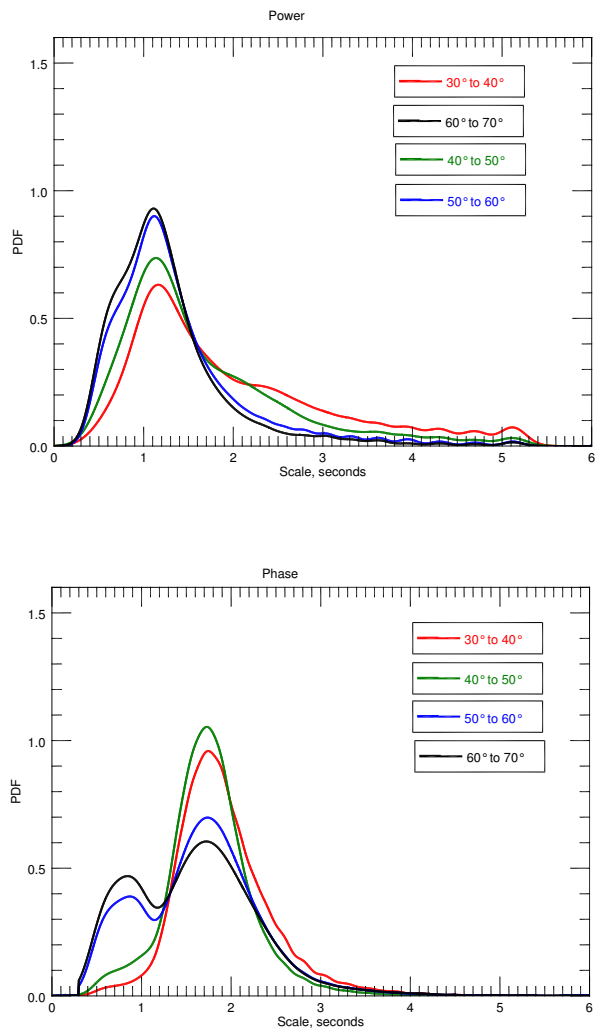


Figure 7.7: Variation of the optimum scale with the elevation angle of the GPS satellite for the power and the phase components of the signal.

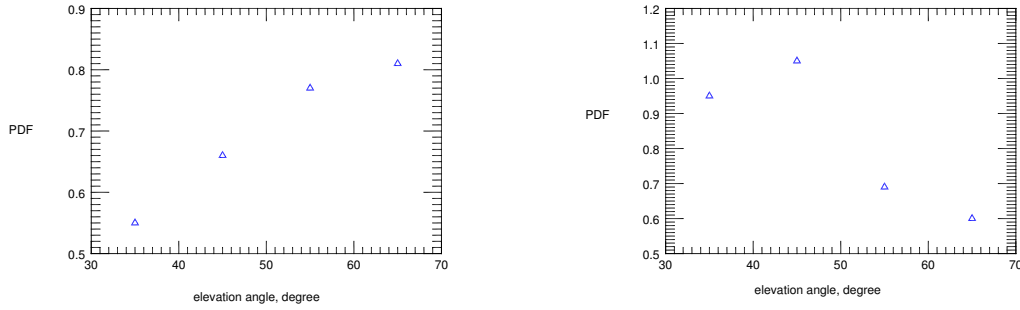


Figure 7.8: Variation of the value of the PDF at the most probable optimum scale for the power (left) and the phase (right) components.

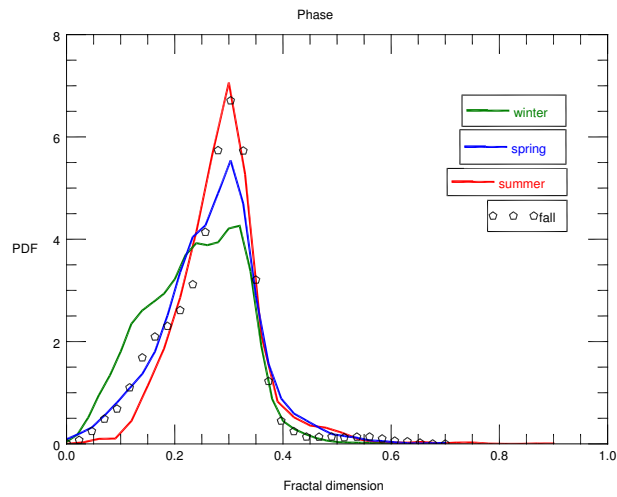
In Figure 7.8, we illustrate the variation of the maximum value of the PDF with the elevation angle. Different characteristics can be stressed for the phase and the power components. The power component exhibits a PDF value proportional to the elevation angle, whereas the phase component exhibits a PDF value at the most probable scale that is inversely proportional to the elevation angle.

7.2.2 Variation of the fractal dimension

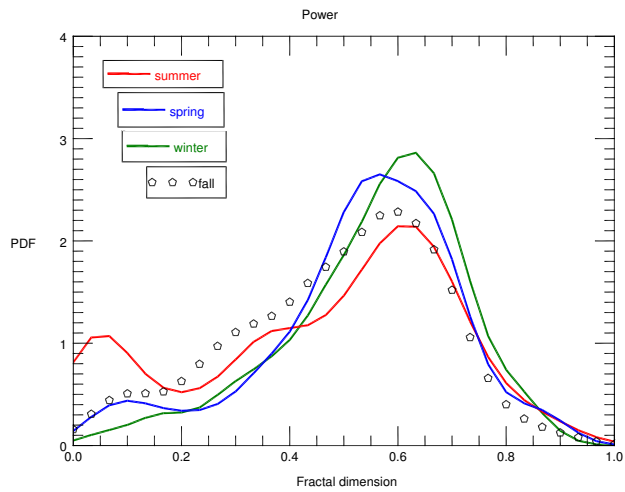
In this section, we investigate the dimensionality of the phase and power scintillation using the wavelet-based fractal dimension. We take $a = s_{min} + \frac{s_{max}-s_{min}}{3}$ and $b = s_{min} + \frac{2(s_{max}-s_{min})}{3}$, where s_{min} and s_{max} , chosen using the maximum entropy criterion, are the scales delimiting the scintillation band in the temporal scale domain. In Figure 7.9, PDFs of the wavelet-based

fractal dimension for different seasons are constructed. For the case of phase scintillation, during winter, a high probability of having low dimensionality is found, while the probability of having higher dimensionality increases when approaching summer.

On the other hand, the power component exhibits an opposite trend: the probability of having the highest dimensionality is at its maximum during winter and decreases when approaching summer. This may indicate a fundamental difference in the nature of the phase and amplitude scintillation.



(a)



(b)

Figure 7.9: PDF associated with the variation of the wavelet-based fractal dimension for the phase and the power components.

The occurrences of high dimensionality events were characterized by constructing scintillation maps. These maps consist of joint probability density function of the fractal dimension lying in the geomagnetic domain.

The joint PDF is defined as follows:

$$\int P(X, Y) dXdY \sim \text{prob}\{D_{min} \leq D \leq D_{max}\} \quad (7.7)$$

where X and Y represent the magnetic local time (MLT) and magnetic latitude (mlat), respectively; D is the fractal dimension, D_{min} and D_{max} represent the lowest and highest boundary, respectively.

Based on the data set, I have selected a threshold of 0.4 for the dimensionality of the power and a threshold of 0.2 for the phase component. These observed thresholds represent the delimiter between scintillation and no scintillation. The range in the magnetic latitude domain chosen for this maps is from 60° MLAT to 90° MLAT.

Figures 7.10 and 7.11 illustrate the distribution of the wavelet-based fractal dimension for the power and the phase, respectively. It is seen that the power and phase components of the signal show similar variation with the seasons. For both the phase and the power components of the signal, one can observe an annual cycle. High order dimensionality occurrences are concentrated in the cusp region (75 MLAT and 85 MLAT); this is most likely the result of energetic particles, originating from the solar wind, precipitating along the magnetic field lines. The distributions are asymmetric during

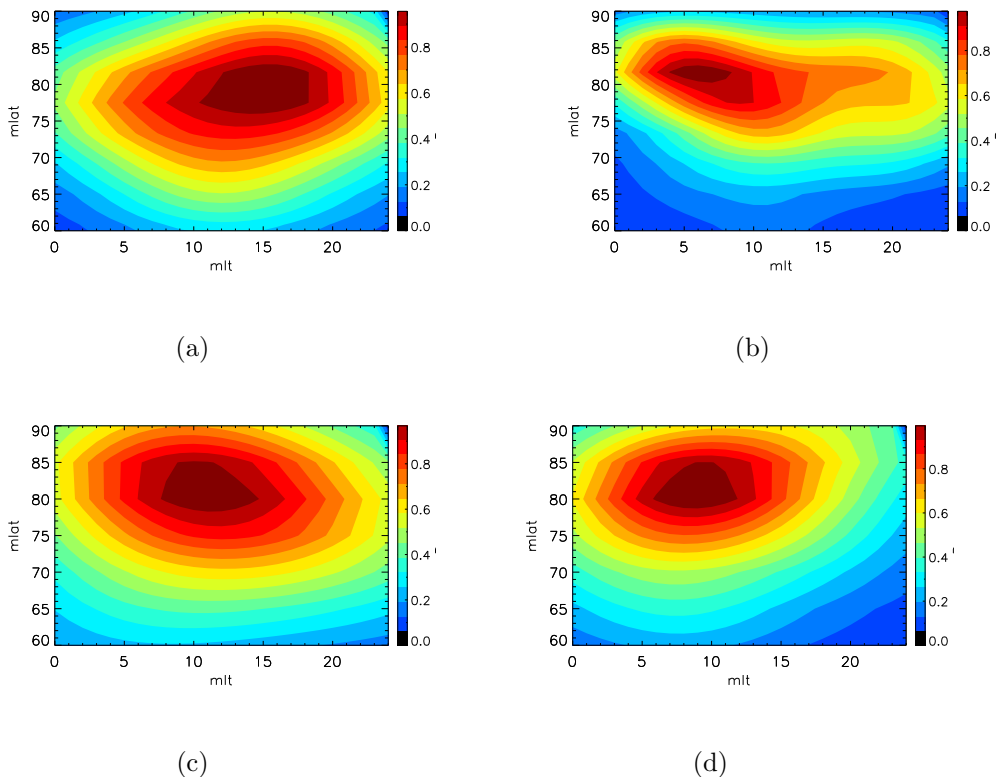


Figure 7.10: Normalized joint probability density function of power scintillation events characterized by $D > 0.4$ for fall (a), winter (b), spring (c), and summer (d).

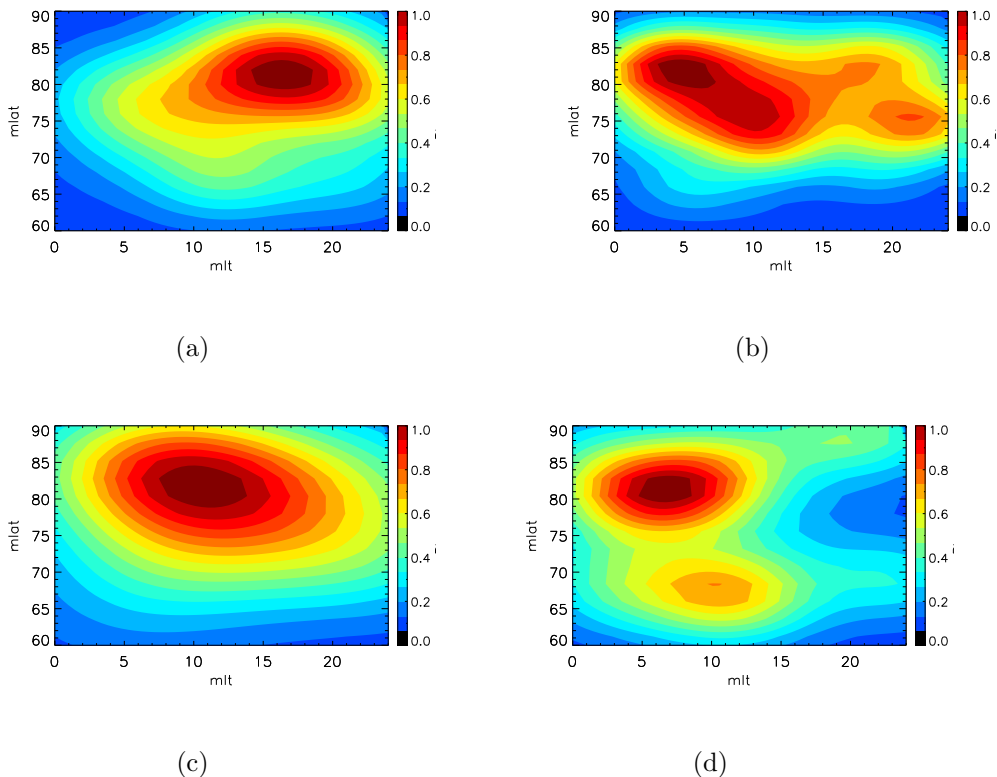


Figure 7.11: Normalized joint probability density function of phase scintillation events characterized by $D > 0.2$ for fall (a), winter (b), spring (c), and summer (d).

winter and symmetric during summer. During winter, the electron density background is low and the occurrences of electron density enhancements are local and singular in nature, and do not follow Gaussian statistics. In addition, conjugacy may play an important role in the local enhancement of the electron density during winter, where electric fields have the possibility to map from the southern hemisphere, characterized by a high conductivity during summer, creating local enhancement responsible for the non-Gaussian aspect observed in the distribution of the fractal-dimension.

7.2.3 Variation of the entropy

In order to relate the chaotic behavior of the ionospheric plasma to the amplitude and phase scintillation, the Tsallis and the Boltzmann-Gibbs entropies were constructed for the power and phase components, respectively. Only scales up to the optimum scale were considered. The corresponding PDFs are illustrated in Figure 7.12. It is seen that the entropy reveals a high probability of having low values during winter, whereas during summer the probability of having a low value of the entropy is lower. This is consistent with the higher stochasticity of the ionospheric plasma during summer, when the ionosphere is directly exposed to the turbulent solar wind, whereas during winter, under night condition, the chaoticity is lower.

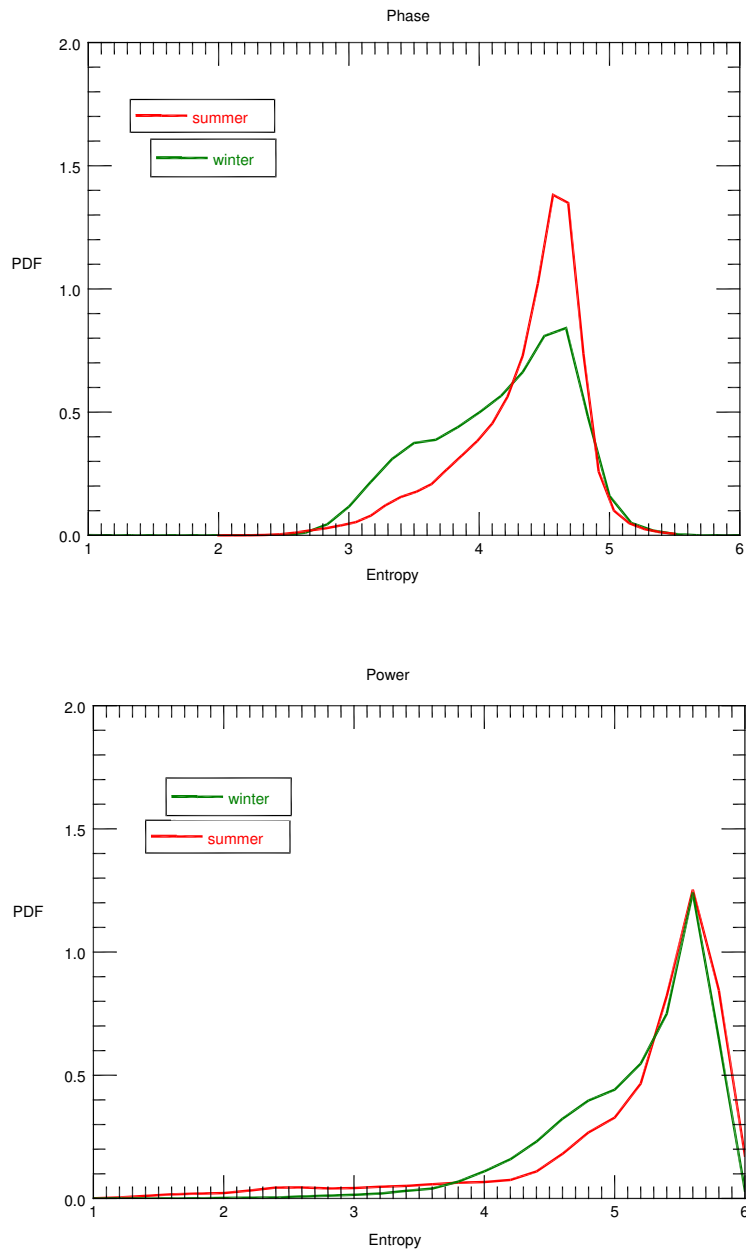


Figure 7.12: PDF associated with the entropy variation of the phase (top panel) and the power (bottom panel) components.

Both the phase and the power entropies exhibit the same behavior. However the phase has a more pronounced discrepancy between the two seasons. In order to characterize the distribution of the entropy, in the following, maps are constructed, where only events with an entropy greater than a certain threshold are taken into account. The threshold is defined as the point where the two distributions, corresponding to the summer and winter conditions, intersect; this corresponds to a threshold of 4.3 for the phase component and 5.3 for the power component.

For the case of power scintillation, there is a discrepancy between summer and winter (Figure 7.13). For winter, the distribution of the entropy is highly asymmetric and centered at $5 \text{ MLT} \pm 1\text{MLT}$, while for the summer the distribution is more symmetric and centered at about $10 \text{ MLT} \pm 2 \text{ MLT}$. The PDF is more skewed towards low latitude during winter, while for the summer time, there is a clear symmetric aspect, except for the singularity at mid-latitude (60 MLAT to 70 MLAT and 12 MLT and 17 MLT).

Most of the occurrences of events with high entropy values are within the cusp region (between 75 MLT and 85 MLT). During winter, the phase entropy presents a localized aspect, both in magnetic local time and magnetic latitude, with a singularity at $20 \text{ MLT} \pm 5 \text{ MLT}$. Whereas, during summer, the distribution is broadened in both domains.

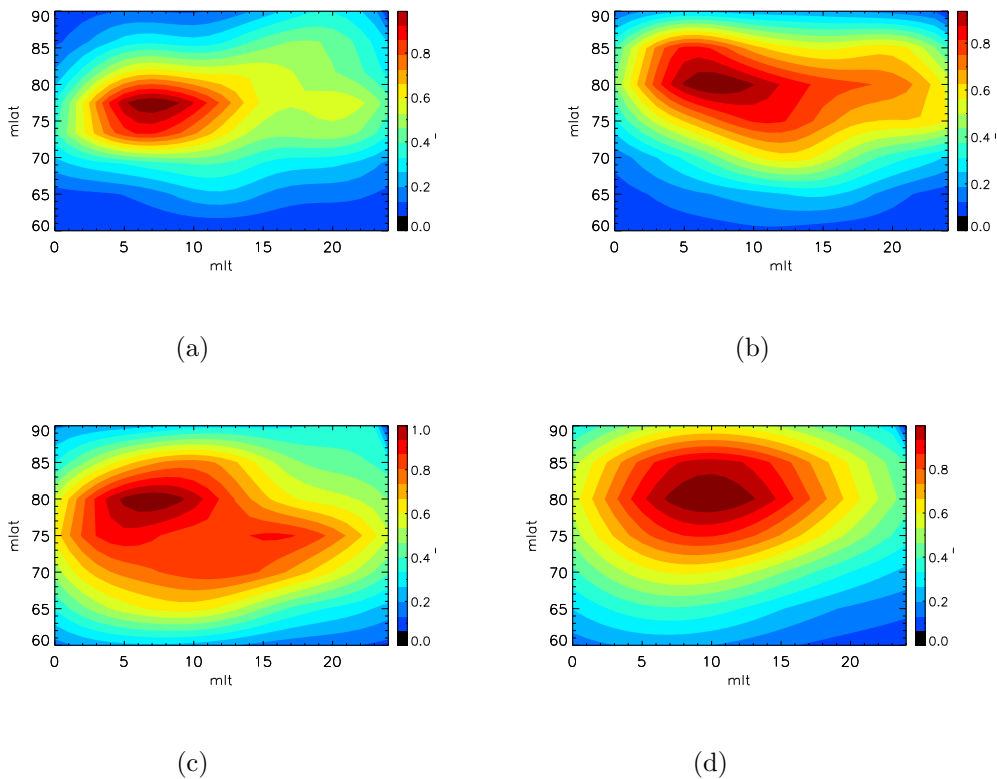


Figure 7.13: Normalized joint probability density function of power scintillation events characterized by an entropy $S > 5.3$ for fall (a), winter (b), spring (c), and summer (d).

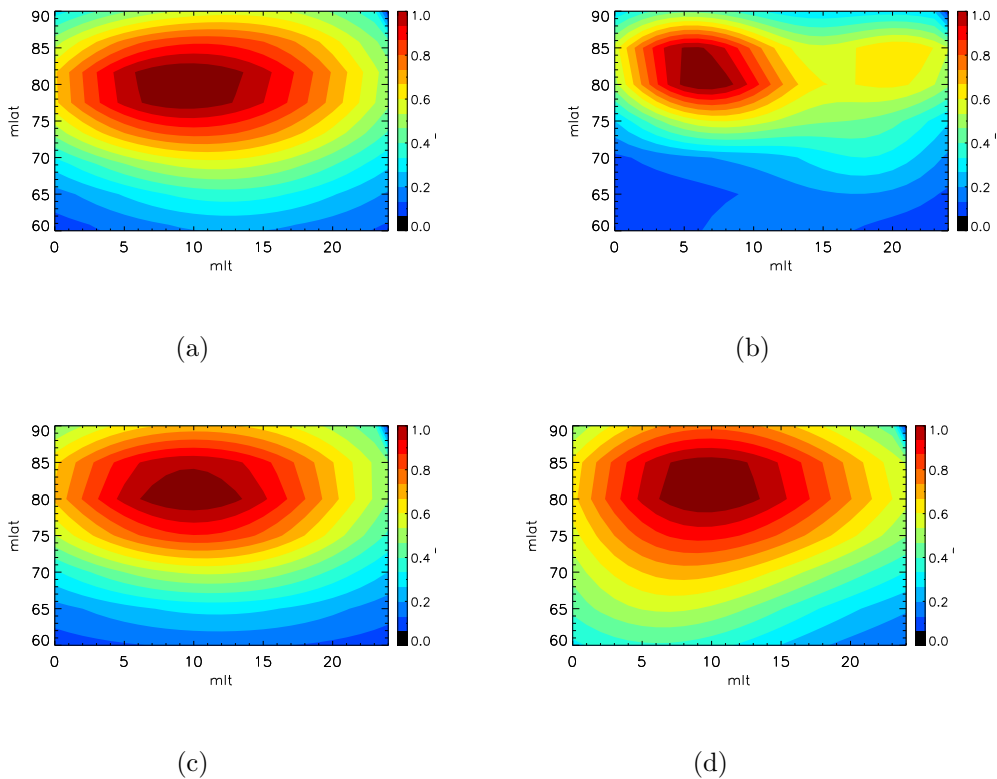


Figure 7.14: Normalized joint probability density function of phase scintillation events characterized by an entropy $S > 4.3$ for fall (a), winter (b), spring (c), and summer (d).

7.3 Conclusion

Using the maximum entropy principle, the scintillation components of the GPS L1 signal were isolated and analyzed. More particularly, we investigated the statistical and the spectral characteristics of the GPS L1 signal during scintillation events. It was found that the optimum scale presents a dependence on the seasons. Also, this statistical signature can constitute an indication about the most predominant Fresnel scale. It is clear that the phase exhibits an optimum scale greater than the one for the power component. This is consistent with the power spectra analyzed during scintillation events for which the breakdown of the power law characterizing the power spectra of the power component of the signal occurs at a low frequency, while the power spectra associated with the phase component do not seem to be characterized by a break down of the power law [Mushini, 2013].

The dimensionality of the phase and the power components of the scintillating GPS signal was quantified. An annual cycle was made evident, and the differences between the phase and the power scintillation components were highlighted. The chaotic behavior and the dynamical complexity were quantified using the wavelet-based entropy. Evidence of an annual cycle was put forth. It was found that the ionospheric scintillation observables present a higher chaoticity during summer. It was also found that the chaoticity is characterized by an assymetric distribution during winter.

Chapter 8

Simulator of the trans-ionospheric channel

The electron density profile in the high latitude region is characterized by a preference of the electrons to align along the magnetic field lines. This makes the geometry of the transionospheric channel completely different from the one at the equatorial region. Contrary to low latitude regions, the propagating trans-ionospheric radio wave (sent from a GPS satellite, in our case of interest) follows a propagation path that is quasi-parallel to the magnetic field lines, with a small angle of incidence. Thus, the approximation which is used in the study of the equatorial scintillation, namely, that the thickness of the ionospheric layer integrated through is much larger than the size of the irregularities, is no longer valid.

In order to have an insight into the different mechanisms at play during the high latitude scintillation, there is a need to construct a numerical model simulating the propagation of the radio wave through the ionospheric layer. In the following, we present a numerical model capable of taking into account the complex geometry of the high latitude ionospheric morphology. In addition, we aim to consider the case of strong scintillation, i.e., we consider the case where the scattering and the diffraction within the ionospheric layer are not neglected. This is achieved by using the split step method [Béniguel and Hamel, 2011].

8.1 Spectral model

In the case of the trans-ionospheric GPS signal, one has to take into account the oblique propagation. Therefore, we will work in the continuously displaced coordinate system (CDCS) [Rino and Carrano, 2011] (see Figure 8.2), where the new modified coordinates are defined as

$$\vec{\rho}_m = \vec{\rho} + \tan(\theta)\hat{a}_\perp z, \quad (8.1)$$

with θ being the complement of the elevation angle, and $\hat{a}_\perp = \cos\phi\vec{e}_x + \sin\phi\vec{e}_y$. The angle ϕ represents the azimuth angle, and the vector $\vec{\rho}$ is the 2-D position vector, given by $\vec{\rho} = x\hat{x} + y\hat{y}$. The propagation problem is then tackled by solving the Helmholtz equation:

$$[\nabla^2 + k^2(1 + \epsilon_1(\vec{\rho}_m, z))]u(\vec{\rho}, z) = 0 \quad (8.2)$$

where k is the wavenumber of the trans-ionospheric radio wave and $\vec{\rho}$ is the vector of the point inside the medium on the plane perpendicular to the axis of propagation z^1 .

The function $\epsilon_1(\vec{\rho}_m, z)$ is the stochastic part of the relative dielectric permittivity, defined as follows:

$$\epsilon_1(\vec{\rho}_m, z) = -\frac{(\omega_p/\omega)^2[\Delta N(\vec{\rho} + \tan \theta \hat{a}_\perp, z)/N_0]}{1 - (\omega_p/\omega)^2} \quad (8.3)$$

¹We use a wavelength $\lambda = 0.19$ m, corresponding to the wavelength of the GPS L1 carrier.

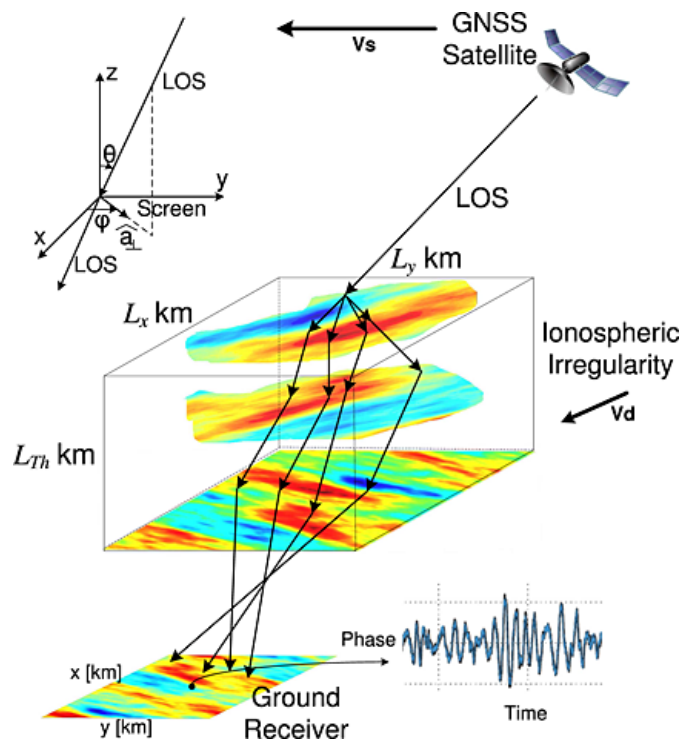


Figure 8.1: Illustration of different parameters of the model [Deshpande et al., 2014].

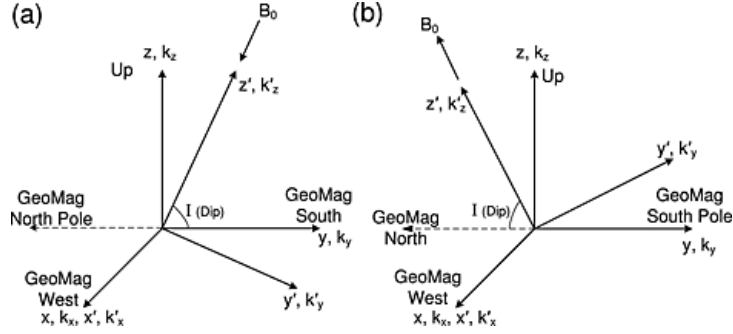


Figure 8.2: The geometry of the GPS signal propagation from the satellite to the ground , for the north hemisphere (a) and the south hemisphere (b) [Deshpande et al., 2014].

The term $\frac{\Delta N(\vec{\rho} + \tan \theta \hat{a}_\perp, z)}{N_0} = \xi$ represents the percentage fluctuation of the electron density, where ω_p is the ionospheric plasma frequency (≈ 12 MHz). By defining a complex amplitude $U(\vec{\rho}, z)$ of the field

$$u(\vec{\rho}, z) = U(\vec{\rho}, z) \exp(jkz), \quad (8.4)$$

one can rewrite the Helmholtz equation in the following form:

$$2jk \frac{\partial U(\vec{\rho}, z)}{\partial z} + (d^2/dx^2 + d^2/dy^2)U(\vec{\rho}, z) + k^2 \epsilon_1(\vec{\rho}_m, z)U(\vec{\rho}, z) = 0 \quad (8.5)$$

The Helmholtz equation is solved using the split step technique, in CDSC, in order to take into account both the scattering effect and the phase change induced by the electron density in the ionospheric layer (Figure 8.1). The procedure is explained in the following text.

As a first step, we solve the equation describing the phase change induced by the non-homogeneous dielectric function:

$$2jk \frac{\partial U(\vec{\rho}, z)}{\partial z} + k^2 \epsilon_1(\vec{\rho}_m, z) U(\vec{\rho}, z) = 0 \quad (8.6)$$

with a solution given by:

$$U(\vec{r}_\perp, z_1) = U(\vec{\rho}, z_0) \exp(j \frac{k}{2} \int_{z_0}^{z_1} \sec \theta \epsilon_1(\vec{\rho} + \tan \theta \hat{a}_\perp, z) dz) \quad (8.7)$$

In the high-latitude context, we adopt the power spectrum proposed by [Costa and Kelley, 1977] for the electron density fluctuations, where the electron density irregularities are represented by ellipsoids aligned along the magnetic field lines.

The spectrum is given in a reference frame with k'_z aligned with the magnetic field line direction (Figure 8.2), by

$$P(\vec{k}') = \frac{a(p_H - 2)}{2\pi^{3/2} k_0^2} \Delta N(\vec{\rho} + \tan \theta \hat{a}_\perp, z)^2 \left(1 + \frac{k_x'^2 + k_y'^2}{k_0^2}\right)^{-p_H/2} \exp(-(ak)^2 \frac{k_z'^2}{k_0^2}) \quad (8.8)$$

with $k_0 = \frac{2\pi}{l_0}$, where l_0 is the outer scale. The exponent p_H is referred to as the spectral index. Here $a = \frac{AXR}{k_0}$, where AXR is the axial ratio characterizing the ellipsoid representative of the electron density irregularity.

The electron density fluctuations are proportional to the power spectrum:

$$N_e(x, y, z) = \Re(\mathbf{F}^{-1}[\sqrt{P} * \exp(i\phi_r)]), \quad (8.9)$$

where \mathbf{F}^{-1} is the inverse Fourier transform and ϕ_r is a random phase between 0 and 2π .

The solution of this equation is input as an initial value for the differential equation describing the free propagation between two phase screens and is defined as follows:

$$2jk \frac{\partial U(\vec{\rho}, z)}{\partial z} + (d^2/dx^2 + d^2/dy^2)U(\vec{\rho}, z) = 0 \quad (8.10)$$

The solution is obtained, in the CDSC, by alternating between the propagation in the ionospheric phase-changing screen and the free propagation. In this work, we solve this partial differential equation numerically using a Crank-Nicolson like stencil. We also assume periodic boundary conditions to simulate an infinite plane in the x-y directions.

8.2 Numerical results

8.2.1 Time series generation

The developed simulator reproduces the components of the field, phase and amplitude, given different parameters characterizing the random medium. It is important to stress that, in practice, the signal recorded with the receiver is a time series. To express the solution of the equation as a time series, one

has to assume a certain drift velocity of the bulk of the ionospheric plasma and apply the Taylor hypothesis (see Chapter 4). Assuming that the spatial structure of the irregularities is moving with a velocity \vec{v}_k , the 3-D electron density field will move across the line of sight. Assuming a "frozen-in" aspect of the field, we can express that motion by translating the coordinates of the plasma bulk:

$$\vec{r} \rightarrow \vec{r} + \vec{v}_d t \quad (8.11)$$

with \vec{v}_d being the combination of the horizontal drift component as well as the vertical component. The time series has been obtained for a thickness of the ionospheric layer $L_{th} = 50$ km, a height of 350 km, and an outer scale, $l_0 = 2$ km. The plasma frequency assumed for the medium is $\omega_p = 12$ MHz and the spectral index for the electron density fluctuations $p_H = 4$. An elevation angle of 49° , an azimuth $\phi = 45^\circ$ and a dip angle $\theta_{dip} = 65^\circ$ have been chosen for the slant propagation.

We assume a drift velocity of 350 m/s, which is the typical value of the velocities for the high latitude region. In Figure 8.3, we give an illustration of a time series output by the simulator given the input parameters mentioned above.

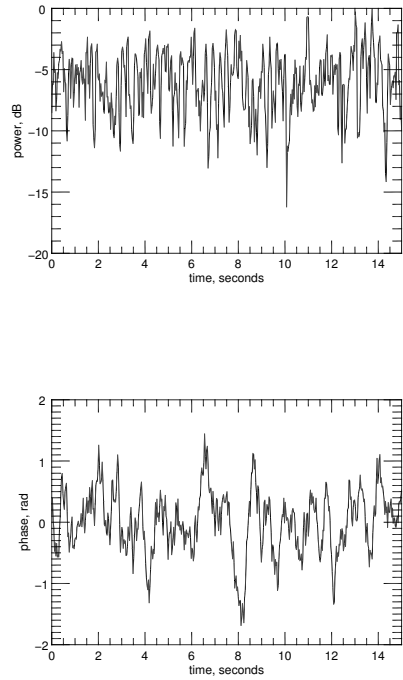


Figure 8.3: Example of the power and phase time series on the ground (top and bottom panels, respectively).

8.2.2 Effect of the spectral index on the field

As discussed previously, the electron density fluctuations in the ionospheric layer are characterized by a power spectrum with a certain spectral index p_H . Different studies, where sounding rockets and satellites were used, revealed such spectral aspects for the high latitude ionospheric irregularities [Costa and Kelley, 1977; Dyson et al., 1974]. Further, it has been shown that the

trans-ionospheric scintillating signals on the ground show similar characteristics [Mushini, 2013; Yeh and Liu, 1982].

In Figure 8.5, we give an example of the power spectra associated with the phase and the power component of the GPS L1 signal during two scintillation events at two different CHAIN stations. One can notice the power law characteristic. The power component presents a breakdown of the power law at a Fresnel frequency. While for the phase component, there is no clear break down of the power law.

In Figure 8.4, we illustrate the effect of the spectral index p_H on the wave front. The contour is constructed for the phase occurrence on the ground. At a lower spectral index, the structure is composed of small-scale irregularities, which spread and increase in size as we go towards large spectral indices.

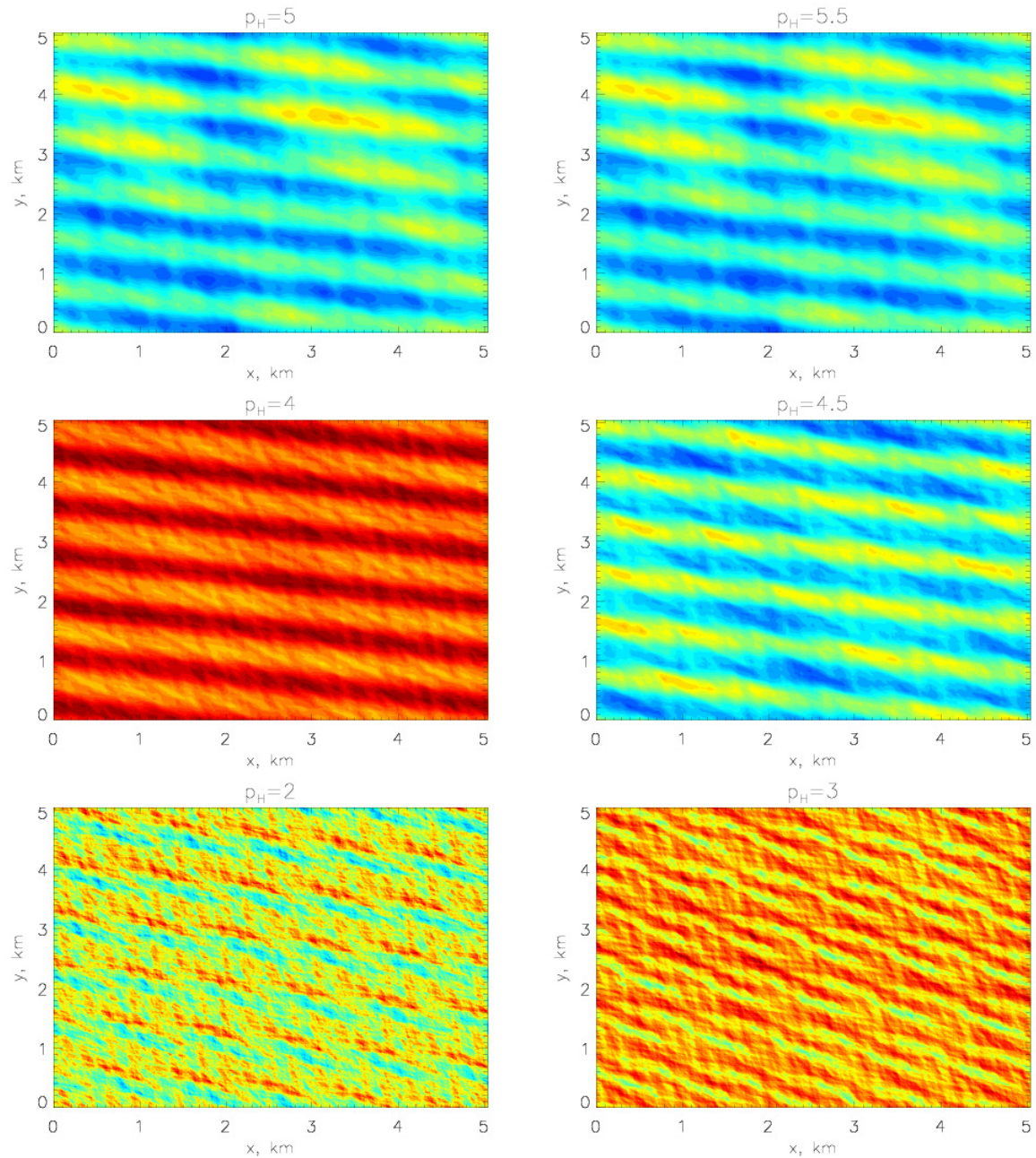


Figure 8.4: Illustration of the phase contour on the ground for different values of the spectral index p_H .

In the present section, we aim at characterizing the competition between the refractive and the diffractive contributions. In order to do so, we investigate the behavior of the spectral index on the ground, characterizing the phase and the power components of the field, against the variation of the local spectral index p_H ².

In Figure 8.6, the variation of the power spectra densities (PSDs) associated with the phase and the power components of the field on the ground, with the local spectral index p_H are shown. Both components exhibit a power law that is characterized by a spectral index that increases consistently with p_H . However, the power component presents a break down of the power law at the Fresnel wavenumber of $k_F = \frac{2\pi}{\lambda_F} = 0.02 \text{ m}^{-1}$, where $\lambda_F = 257 \text{ m}$ is the Fresnel scale for a height of 350 km and a wavelength of 0.19 m (GPS L1 signal carrier). These features are consistent with our observations at high latitudes (Figure 8.5).

For higher values of the spectral index p_H , the slope characterizing the power spectrum is steeper, meaning that contributions from scales greater than the Fresnel scale are important. Hence, in this case, the refractive components are the most dominant. On the other hand, in the case where the power spectrum illustrates a lower value, the diffractive contributions are the most dominant.

²Throughout the remaining text, the input parameters considered are the same as the ones used in the previous sections, unless indicated otherwise.

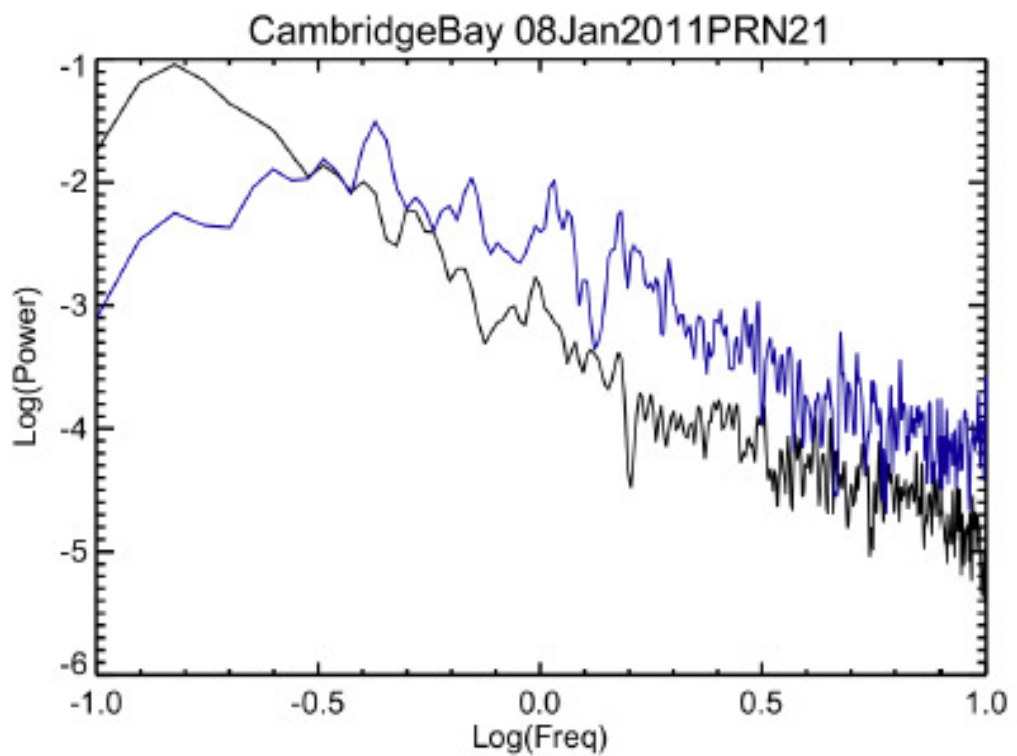


Figure 8.5: Corresponding phase (black) and amplitude (blue) scintillation spectra observed a scintillation event. Fresnel filtering is clearly observed in the amplitude spectra while there is no Fresnel filtering in the phase spectra [Mushini, 2013].

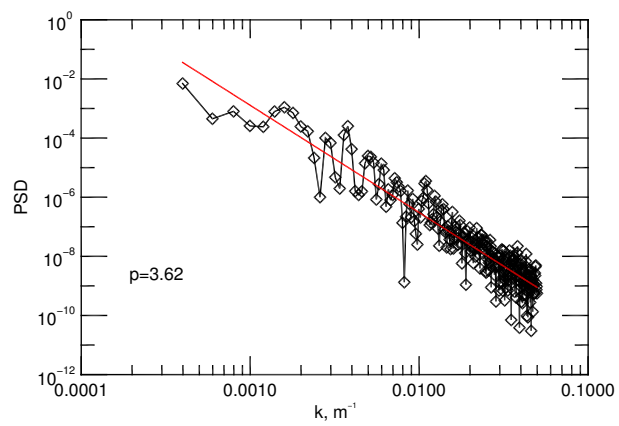
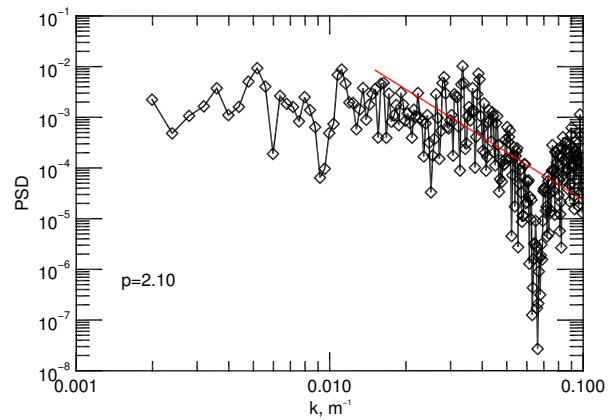


Figure 8.6: Illustration for the power spectra for the phase (top panel) and the power (bottom panel) components of the signal for $P_H = 4$.

8.3 Conclusion

Based on the hybrid spectral model proposed by Costa and Kelley, we constructed a simulator of the transionospheric channel for the case of high latitude scintillation. The simulator can take into account the complex geometry of the high latitude ionospheric irregularities [Costa and Kelley, 1977].

Preliminary results were presented. We have been able to reproduce the general features of the spectra observed during ionospheric scintillation events at high latitude, where a break down of the power law is observed for the power, while the phase component does not reveal such characteristic. The sensitivity of the spectral index of the phase and power components to the local spectral index p_H , characterizing the electron density fluctuations in the ionospheric slab, has been investigated. It has been found that the refractive contributions are more important for higher values of p_H , where scales larger than the Fresnel scale are predominant, and for lower values of p_H diffractive contributions are predominant. Also, it has been shown that for low values of the axial ratio, the diffraction contributions are predominant, while for higher values of AXR the refractive contributions are the most important. While this model is well suited for solving the trans-ionospheric wave propagation equation for the high latitude scintillation case, it is also capable of reproducing scintillations at lower latitudes, such as the equatorial region.

Chapter 9

Conclusion

Ionospheric scintillations are the product of the refractive and diffractive aspects of the ionospheric plasma. The GPS signal constitutes a good observable in terms of describing the dynamics and the morphology of the medium. In order to study the ionospheric scintillation and understand the mechanism at play, it is of primary importance to optimize the cut-off frequency adopted in singling out the scintillation components. For this purpose, the entropy maximization technique has been adopted.

In Chapter 5, a general wavelet-based entropy was proposed and computed for the phase and the power components. It has been found that the statistical behaviors of the phase and the power components, during scintillation, present a discrepancy with regard to one another. The Boltzmann-Gibbs entropy was constructed for the phase, given that the latter presented Gaussian statistics. On the other hand, the power component departed from Gaussian-

ity, and the corresponding Tsallis entropy was constructed. The optimum cut-off scale/frequency was adopted as the scale maximizing the entropy. Chapter 6, with regard to the short term intermittent aspect of the scintillation, presented a model for the power fluctuations based on the Castaing distribution and the evaluation of the corresponding higher order moments. It has been found that the intermittency is higher at smaller scales.

In Chapter 7, the statistical behaviour of the optimum scale was investigated, where a climatology study of the ionospheric scintillation was performed. A seasonal cycle was observed for the optimum scale. It has been shown that the probability of having the largest optimum scale is at its highest during summer. Also, it has been shown that the scintillation presented a higher chaoticity during summer.

The dimensionality of the ionospheric scintillation was also quantified by introducing a wavelet-based fractal dimension for the phase and the power components of the GPS signal during ionospheric scintillation. The dimensionality of the phase fluctuations presented a lower value during winter, whereas the power component presented a lower dimensionality during summer.

Finally, in Chapter 8, a simulator of the ionospheric scintillation was developed. The model takes into account the case of strong scintillation, where the amplitude fluctuations start to build up inside the ionospheric slab. The features of the power spectra of the observed scintillation events were reproduced: it has been found that the power fluctuations were characterized by

a power spectral density presenting a power law with a break down at the Fresnel scale. The phase, on the other hand, did not present this feature. Overall, as shown in this thesis, the statistical characteristics of the ionospheric scintillation are of primary interest. The maximum entropy principle permits us to identify the optimum detrending scale/frequency. Automating this procedure will permit us to perform an unbiased mitigation of the ionospheric scintillation effects.

The developed simulator could be used in order to solve the inverse problem, taking into account other measurements, such as collocated ionosonde measurements.

Bibliography

- Aarons, J. (1982). Global morphology of ionospheric scintillations. *Proceedings of the IEEE*, 70(4):360–378.
- Baker, K. and Wing, S. (1989). A new magnetic coordinate system for conjugate studies at high latitudes. *Journal of Geophysical Research: Space Physics*, 94(A7):9139–9143.
- Basu, S., Basu, S., MacKenzie, E., Coley, W., Sharber, J., and Hoegy, W. (1990). Plasma structuring by the gradient drift instability at high latitudes and comparison with velocity shear driven processes. *Journal of Geophysical Research: Space Physics*, 95(A6):7799–7818.
- Basu, S., MacKenzie, E., Basu, S., Fougere, P., Maynard, N., Coley, W., Hanson, W., Winningham, J., Sugiura, M., and Hoegy, W. (1988). Simultaneous density and electric field fluctuation spectra associated with velocity shears in the auroral oval. *Journal of Geophysical Research*, 93:115–136.
- Basu, S., MacKenzie, E., Costa, E., Fougere, P., Carlson, H., and Whitney, H. (1987). 250 MHz/GHz scintillation parameters in the equatorial, polar, and

- auroral environments. *IEEE journal on selected areas in communications*, 5(2):102–115.
- Batchelor, G. and Townsend, A. (1949). The nature of turbulent motion at large wave-numbers. 199(1057):238–255.
- Béniguel, Y. and Hamel, P. (2011). A global ionosphere scintillation propagation model for equatorial regions. *Journal of Space Weather and Space Climate*, 1(1):A04.
- Booker, H. G., Ratcliffe, J., and Shinn, D. (1950). Diffraction from an irregular screen with applications to ionospheric problems. *Philosophical Transactions of the Royal Society of London A: Mathematical, Physical and Engineering Sciences*, 242(856):579–607.
- Castaing, B., Gagne, Y., and Hopfinger, E. (1990). Velocity probability density functions of high reynolds number turbulence. *Physica D: Nonlinear Phenomena*, 46(2):177–200.
- Chatwin, P. and Sullivan, P. J. (1989). The intermittency factor of scalars in turbulence. *Physics of Fluids A: Fluid Dynamics*, 1(4):761–763.
- Costa, E. and Kelley, M. (1977). Ionospheric scintillation calculations based on in situ irregularity spectra. *Radio Science*, 12(5):797–809.
- Cronyn, W. M. (1970). The analysis of radio scattering and space-probe observations of small-scale structure in the interplanetary medium. *The Astrophysical Journal*, 161:755.

- Davies, K. (1990). *Ionospheric radio*. IET.
- de Toma, G., White, O. R., Chapman, G. A., Walton, S. R., Preminger, D. G., Cookson, A. M., and Harvey, K. L. (2001). Differences in the sun's radiative output in cycles 22 and 23. *The Astrophysical Journal Letters*, 549(1):L131.
- de Toma, G., White, O. R., Knapp, B. G., Rottman, G. J., and Woods, T. N. (1997). Mg ii core-to-wing index: Comparison of sbuv2 and solstice time series. *Journal of Geophysical Research: Space Physics*, 102(A2):2597–2610.
- Deshpande, K., Bust, G., Clauer, C., Rino, C., and Carrano, C. (2014). Satellite-beacon ionospheric-scintillation global model of the upper atmosphere (sigma) i: High-latitude sensitivity study of the model parameters. *Journal of Geophysical Research: Space Physics*, 119(5):4026–4043.
- Dyson, P., McClure, J., and Hanson, W. (1974). In situ measurements of the spectral characteristics of F region ionospheric irregularities. *Journal of Geophysical Research*, 79(10):1497–1502.
- Dyson, P. and Winningham, J. (1974). Top side ionospheric spread f and particle precipitation in the day side magnetospheric clefts. *Journal of Geophysical Research*, 79(34):5219–5230.
- Farge, M. (1992). Wavelet transforms and their applications to turbulence. *Annual review of fluid mechanics*, 24(1):395–458.

- Forte, B. and Radicella, S. M. (2002). Problems in data treatment for ionospheric scintillation measurements. *Radio Science*, 37(6).
- Forte, B. and Radicella, S. M. (2005). Comparison of ionospheric scintillation models with experimental data for satellite navigation applications. *Annals of Geophysics*.
- Fraser, A. M. and Swinney, H. L. (1986). Independent coordinates for strange attractors from mutual information. *Physical Review A*, 33(2):1134.
- Frisch, U. (1995). *Turbulence (Cambridge)*. Cambridge Univ. Press.
- Gola, M., Wernik, A., Franke, S., Liu, C., and Yeh, K. (1992). Behaviour of HILAT scintillation over Spitsbergen. *Journal of Atmospheric and Terrestrial Physics*, 54(9):1207–1213.
- Grassberger, P. and Procaccia, I. (1983). Characterization of strange attractors. *Physical review letters*, 50(5):346.
- Haldoupis, C., Kelley, M. C., Hussey, G. C., and Shalimov, S. (2003). Role of unstable sporadic-E layers in the generation of midlatitude spread F. *Journal of Geophysical Research: Space Physics*, 108(A12).
- Jones, I. (1960). Further observations of radio stellar scintillation. *Journal of Atmospheric and Terrestrial Physics*, 19(1):26–36.
- Kelley, M. C. (2009). *The Earth's Ionosphere: Plasma Physics & Electrodynamics*, volume 96. Academic press.

Kelley, M. C., Vickrey, J. F., Carlson, C., and Torbert, R. (1982). On the origin and spatial extent of high-latitude f region irregularities. *Journal of Geophysical Research: Space Physics*, 87(A6):4469–4475.

Kivelson, M. G. and Russell, C. T. (1995). *Introduction to space physics*. Cambridge university press.

Mushini, S. C. (2013). *Characteristics of Scintillating GPS Signal at High Latitudes During Solar Minima*. PhD thesis, University of New Brunswick, Department of Physics.

Prikryl, P., Jayachandran, P., Mushini, S., and Chadwick, R. (2011). Climatology of gps phase scintillation and hf radar backscatter for the high-latitude ionosphere under solar minimum conditions. 29(2):377–392.

Rino, C. (1976). Some new results on the statistics of radio wave scintillation, 2. scattering from a random ensemble of locally homogeneous patches. *Journal of Geophysical Research*, 81(13):2059–2064.

Rino, C. L. and Carrano, C. S. (2011). The application of numerical simulations in beacon scintillation analysis and modeling. *Radio Science*, 46(3).

Rufenach, C. (1971). A radio scintillation method of estimating the small-scale structure in the ionosphere. *Journal of Atmospheric and Terrestrial Physics*, 33(12):1941–1951.

Secan, J., Bussey, R., Fremouw, E., and Basu, S. (1995). An improved model of equatorial scintillation. *Radio Science*, 30(3):607–617.

Secan, J., Bussey, R., Fremouw, E., and Basu, S. (1997). High-latitude upgrade to the wideband ionospheric scintillation model. *Radio Science*, 32(4):1567–1574.

Seeber, G. (2003). *Satellite geodesy: foundations, methods, and applications*. Walter de Gruyter.

Shepherd, S. (2014). Altitude-adjusted corrected geomagnetic coordinates: Definition and functional approximations. *Journal of Geophysical Research: Space Physics*, 119(9):7501–7521.

Shkarofsky, I. (1968). Generalized turbulence space-correlation and wave-number spectrum-function pairs. *Canadian Journal of Physics*, 46(19):2133–2153.

Simon, M. K., Omura, J. K., Scholtz, R. A., and Levitt, B. K. (1994). *Spread spectrum communications handbook*, volume 2. Citeseer.

Spits, J. (2012). *Total Electron Content reconstruction using triple frequency GNSS signals*. PhD thesis, Université de Liège, Belgique.

Spogli, L., Alfonsi, L., De Franceschi, G., Romano, V., Aquino, M., and Dodson, A. (2009). Climatology of gps ionospheric scintillations over high and mid-latitude european regions.

Takens, F. (1981). Detecting strange attractors in turbulence. In *Dynamical systems and turbulence, Warwick 1980*, pages 366–381. Springer.

- Tsallis, C. (1988). Possible generalization of boltzmann-gibbs statistics. *Journal of statistical physics*, 52(1):479–487.
- Tsunoda, R. T. (1988). High-latitude F region irregularities: A review and synthesis. *Reviews of Geophysics*, 26(4):719–760.
- Urneki, R., Liu, C., and Yeh, K. (1977). Multifrequency studies of ionospheric scintillations. *Radio Science*, 12(2):311–317.
- Van Dierendonck, A. and Arbesser-Rastburg, B. (2004). Measuring ionospheric scintillation in the equatorial region over africa, including measurements from sbas geostationary satellite signals. In *Proceeding of ION GNSS 17th technical meeting of the satellite division, Long Beach, CA*, volume 316.
- Vickrey, J. F., Rino, C. L., and Potemra, T. A. (1980). Chatanika/triad observations of unstable ionization enhancements in the auroral F-region. *Geophysical Research Letters*, 7(10):789–792.
- Watson, C. (2011). Gps tec and riometer techniques for observing absorption events in the high latitude ionosphere. Master’s thesis.
- Wernik, A., Liu, C., Franke, S., and Gola, M. (1990). High-latitude irregularity spectra deduced from scintillation measurements. *Radio Science*, 25(5):883–895.
- Yeh, K. C. and Liu, C.-H. (1982). Radio wave scintillations in the ionosphere. *Proceedings of the IEEE*, 70(4):324–360.

Vita

Candidate's full name: Hichem Mezaoui

University attended:

University of Provence, Master of Science, 2009

Publications:

- Mezaoui, H., A. M. Hamza, and P. T. Jayachandran. "Dynamic analysis of the polar ionosphere using the GPS signal: Toward an optimization of the cutoff scale." *Radio Science* 52.2 (2017): 271-281.
- Mezaoui, H., A. M. Hamza, and P. T. Jayachandran. "Highlatitude intermittent ionospheric scintillations: Exploring the Castaing distribution." *Journal of Geophysical Research: Space Physics* 120.8 (2015): 6831-6836.
- Mezaoui, H., A. M. Hamza, and P. T. Jayachandran. "Investigating highlatitude ionospheric turbulence using global positioning system data." *Geophysical Research Letters* 41.19 (2014): 6570-6576.

Conference Paper:

Mezaoui, H., A. M. Hamza, and P. T. Jayachandran. "Characterization of the ionospheric scintillations at high latitude using GPS signal." General Assembly and Scientific Symposium (URSI GASS), XXXIth URSI. IEEE, 2014.

Conference Presentations:

- Dynamic analysis of the polar ionosphere using the Tsallis entropy.
Mezaoui, H., Hamza, A. M., Jayachandran, P. T. CAP congress, Ottawa, 13-17 June, 2016.
- Characterization of ionospheric turbulence at high latitude regions using CHAIN
Mezaoui, H., Hamza, A. M., Jayachandran, P. T. Division of Atmospheric and Space Physics Annual Meeting, Fredericton, Canada, February 19-21, 2014.
- Characterization of the Ionospheric Scintillations at High Latitude using GPS Signal Mezaoui, H., Hamza, A. M., Jayachandran, P. T. American Geophysical Union, Fall Meeting 2013, abstract SA21B-2027.